The effect of steep lateral bathymetries on the 3D-hydrodynamics in tidal estuaries

Cas van Ooijen

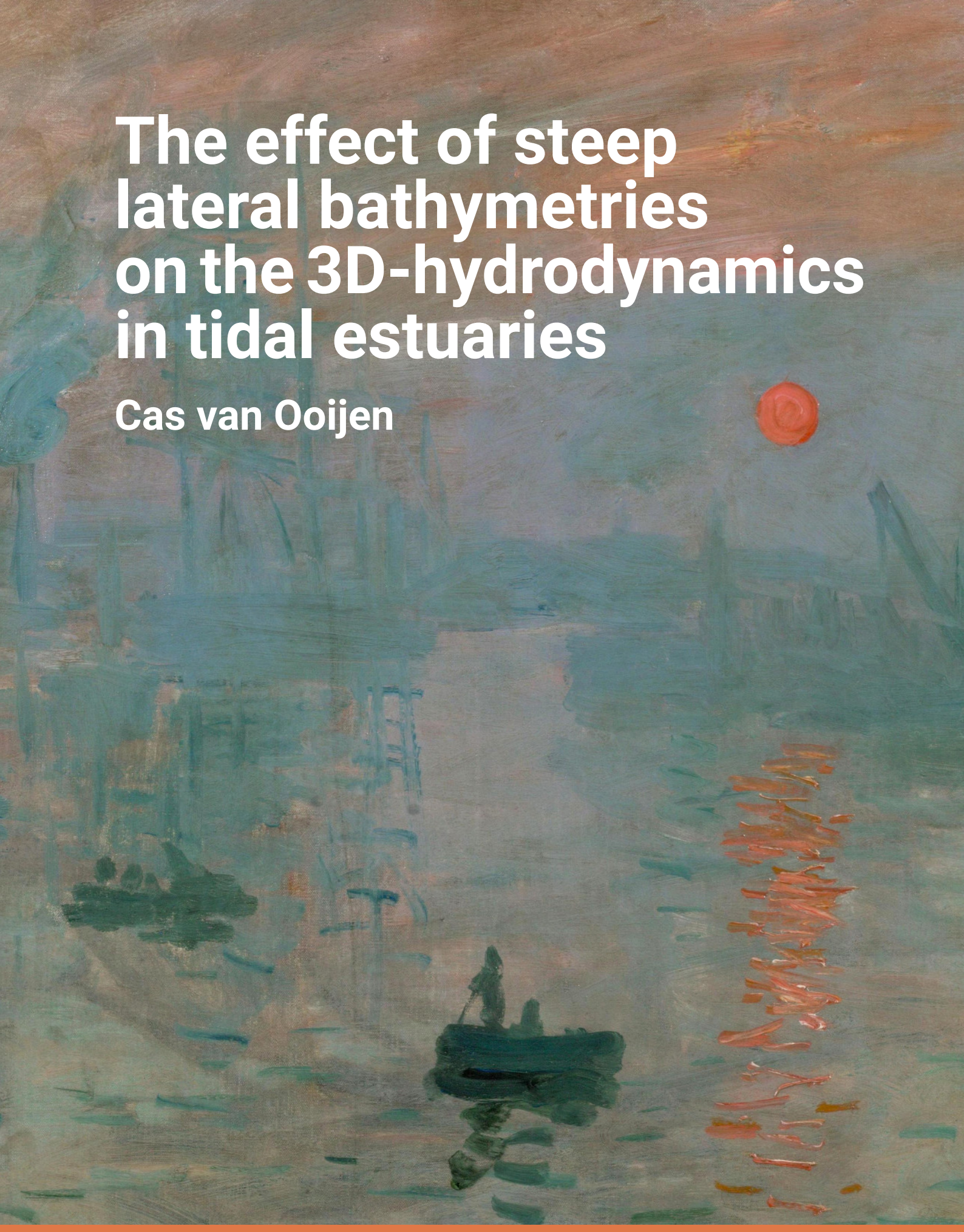

TU Delft

The effect of steep lateral bathymetries on the 3D-hydrodynamics in tidal estuaries

by

Cas van Ooijen

Student number:	5076781	
Project duration:	November 23, 2023 – July 9, 2024	
Thesis committee:	Prof. dr. Henk Schuttelaars	Responsible supervisor
	Dr. ir. Yoeri Dijkstra	Daily supervisor
	Ir. Marco Rozendaal	Daily co-supervisor
	Dr. Alexander Heinlein	Independent member

TU Delft

Summary

Lay summary

In estuaries, the part of a river where the flow is predominantly driven by the tide, the water motion is important to understand. For instance, by understanding the flow, one can better predict how pollutants are transported, or when flooding is likely to occur. However, much is still unknown about certain aspects of the water motion, such as how the hydrodynamics are influenced by the steepness of the river bed. In this thesis, the effect of steep lateral inclines on the river bed is systematically investigated. Because these steep inclines come with significant mathematical challenges, a new model for the water motion in estuaries is developed.

To study the effects of steepness, the model is applied to short estuaries with increasingly deep channels with increasingly steep inclines in the middle of the river, and shallower waters closer to the banks. The results indicate that during flood, i.e. the moment when flow into the estuary is strongest, water flows in through the deep channel and then from the channel towards the banks. During ebb, this pattern is reversed. For estuaries with steeper beds, currents are stronger, and the previously mentioned pattern is more pronounced.

Through a process known as *momentum advection*, so-called residual currents appear that are present regardless of the phase of the tidal cycle. Because these residual currents produce net transport by the movement of water, they are crucial in many transport processes involving sand, mud, salt, pollutants or other materials. The structure of the current is as follows: in the deeper channels, the residual current flows from the sea into the channel, and close to the banks, water flows out of the estuary. Steeper beds cause the residual flow to become stronger and (indirectly) because of the Coriolis effect, notably asymmetric.

Summary

In this thesis, the effect of steep lateral bathymetries on the three-dimensional hydrodynamics of estuaries, i.e. the part of a river where the water motion is primarily forced by the tide, is systematically investigated. Special focus is put on residual currents driven by (non-linear) momentum advection through the tidal motion. Because current three-dimensional idealised models are unable to give accurate results when advection becomes a dominant process, which can be the case for steep bathymetries, a new three-dimensional idealised model is developed.

The model is based on the three-dimensional Reynolds-averaged shallow water equations and solved using a truncation method, in which the equations and boundary conditions are projected onto a Fourier basis in time and an eigenfunction basis in the vertical dimension. The resulting system of non-linear differential equations is discretised using the spectral element method, and solved using the Newton-Raphson method.

To investigate the effects of steepnes systematically, the model is applied to short, rectangular estuaries with a Gaussian bathymetry whose steepness is controlled by a *steepness parameter*. First, the model results corresponding to a nearly flat bathymetry are compared to the results corresponding to a steep bathymetry. Subsequently, the most striking observations are quantified using parameters that capture these observations in a single scalar value.

The results indicate that bathymetry steepness has the following effects on the semidiurnal tidal water motion: firstly, as the steepness increases, along-channel tidal velocities increase in the deep parts of the estuary and decrease in the shallow parts. This effect is caused by the increased maximum depth and decreased minimum depth associated to higher values of the steepness parameter. Furthermore, steeper bathymetries lead to larger cross-channel (lateral) velocities. During flood, water flows in through the deep channel, and from the channel towards the shallower areas closer to the banks, and during ebb, the flow is reversed. In estuaries with less steep bathymetries, this lateral structure is less pronounced. Finally, significant phase differences between flow velocities in the channel and closer to the banks appear as the steepness parameter increases; velocities in the channel are increasingly delayed compared the velocities closer to the banks.

The steepness parameter also has notable influence on advectively-driven residual currents: in estuaries with steeper bathymetries, inflow through the deep channel is stronger and the lateral structure is more asymmetric. The forcing balances indicate that for estuaries with nearly flat bathymetries, residual currents are primarily driven by along-channel momentum advection. As the steepness increases, contributions from lateral and vertical advection increasingly take part in generating along-channel residual currents. While it is difficult to draw definitive conclusions about lateral residual flow, due to the large number of numerical artifacts left in the solutions, the results seem to indicate that the current is pointed from the channel towards the banks.

Contents

List of Symbols

Coordinates

x, y	horizontal Cartesian coordinates [m]
z	vertical Cartesian coordinate [m]
t	time [s]
φ	latitude [°]
ς	transformed vertical coordinate with range $[-1, 0]$ regardless of depth [-]
$\Lambda_1, \Lambda_2, \Lambda_3$	barycentric coordinates associated with a specific triangle [-]

Physical quantities

$u(x, y, z, t)$	along-channel flow velocity [ms^{-1}]
$v(x, y, z, t)$	cross-channel flow velocity [ms^{-1}]
$w(x, y, z, t)$	vertical flow velocity [ms^{-1}]
$\mathbf{u}(x, y, z)$	flow velocity vector, given by $\mathbf{u} = (u, v, w)$
$\rho(x, y, z, t)$	density [$\mathrm{kg\,m}^{-3}$]
$\tau^{x_i x_j}(x, y, z, t)$	elements of the stress tensor [Pa]
$p(x, y, z, t)$	pressure [Pa]
$\zeta(x, y, t)$	water surface elevation above mean water level [m]
$H(x, y)$	water depth/bathymetry [m]
$S(x, y)$	salinity [psu]
$A_{M_{2i}}(x, y)$	tidal forcing amplitude of component M_{2i} [m]
$\theta_{M_{2i}}(x, y)$	tidal forcing phase of component M_{2i} [s]
$q_{\mathrm{DI}}(x, y, t)$	depth-integrated normal flow at riverine boundary [$\mathrm{m}^2\mathrm{s}^{-1}$]

Other quantities

$\tilde{\omega}(x, y, \varsigma, t)$	alternative definition of vertical velocity [s^{-1}], given by $\tilde{\omega} = H^{-1}(w - \varsigma u H_x - \varsigma v H_y)$
$h_i(t)$	Fourier basis function for tidal constituent M_{2i}. Positive i denotes real part and negative i the imaginary part
$f_m(\varsigma)$	vertical orthogonal eigenfunction basis function corresponding to the m-th vertical component
$\alpha_{mi}(x, y)$	along-channel velocity coefficient for the product of vertical basis function $f_m(\varsigma)$ and Fourier basis function $h_i(t)$
$\beta_{mi}(x, y)$	cross-channel velocity coefficient for the product of vertical basis function $f_m(\varsigma)$ and Fourier basis function $h_i(t)$
$\boldsymbol{\alpha}_{mi}(x, y)$	vector of horizontal velocity coefficients, given by $\boldsymbol{\alpha}_{mi} = (\alpha_{mi}, \beta_{mi})$
$\gamma_i(x, y)$	water surface coefficient corresponding to Fourier basis function $h_i(t)$

Physical parameters

g	gravitational acceleration [ms^{-2}]
f	Coriolis frequency [$\mathrm{rad\,s}^{-1}$], given by $f = 2\Omega \sin\phi$
f_*	reciprocal Coriolis frequency [$\mathrm{rad\,s}^{-1}$], given by $f_* = 2\Omega \cos\phi$
Ω	angular velocity of Earth's rotation about its axis [$\mathrm{rad\,s}^{-1}$]
μ	dynamic viscosity [$\mathrm{kg\,m}^{-1}\mathrm{s}^{-1}$]

ν	kinematic viscosity [$m^2 s^{-1}$], given by $\nu = \mu/\rho$
α	coefficient of thermal expansion [K^{-1}]
β	coefficient of saline contraction [psu^{-1}]
A_h	horizontal eddy viscosity parametrising energy dissipation through horizontal turbulent eddies [$m^2 s^{-1}$]
$\mathscr{A}_h$	horizontal effective eddy viscosity [$m^2 s^{-1}$], given by $\mathscr{A}_h = A_h + \nu$
A_v	vertical eddy viscosity parametrising energy dissipation through vertical turbulent eddies [$m^2 s^{-1}$]
$\mathscr{A}_v$	vertical effective eddy viscosity [$m^2 s^{-1}$], given by $\mathscr{A}_v = A_v + \nu$
p_a	atmospheric pressure [Pa]
σ	frequency of the principal semidiurnal tide (M_2) [s^{-1}]
T	period of the principal semidiurnal tide [s]
Q	exchange rate [$m^3 s^{-1}$]
COM	center of mass of positive residual flow [m]

Numerical parameters

ε	weighting parameter for advective terms
M	total number of vertical basis functions taken into account
$i_{\max}$	total number of tidal constituents M_{2i} taken into account, excluding residual/subtidal flow M_0
$H^1_{i,k}$	coefficient defined by the inner product $(h_i, h_k)_2$, for $i, k = -i_{\max}, \dots, i_{\max}$
$H^2_{i,k}$	coefficient defined by the inner product $(h_i', h_k)_2$, for $i, k = -i_{\max}, \dots, i_{\max}$
$H^3_{i,j,k}$	coefficient defined by the inner product $(h_i h_j, h_k)_2$ for $i, j, k = -i_{\max}, \dots, i_{\max}$
H^4_k	coefficient defined by the inner product $(h_k, 1)_2$ for $k = -i_{\max}, \dots, i_{\max}$
$G^1_{m,\ell}$	coefficient defined by the inner product $(f_m, f_\ell)_2$ for $m, \ell = 1, \dots, M$
$G^2_{m,n,\ell}$	coefficient defined by the inner product $(f_m f_n, f_\ell)_2$ for $m, n, \ell = 1, \dots, M$
$G^3_{m,n,\ell}$	coefficient defined by the inner product $(\varsigma \mapsto f_m' \int_{-1}^{\varsigma} f_n \, \mathrm{d}\varsigma', f_k)_2$ for $m, n, \ell = 1, \dots, M$
G^4_ℓ	coefficient defined by the inner product $(\varsigma \mapsto \varsigma, f_\ell)_2$ for $\ell = 1, \dots, M$
p	order of the SEM basis
$\Delta x_{\max}$	maximum element size
K	threshold for the mesh refinement rule

Shape parameters

L	length of the estuary [m]
B	width of the estuary [m]
H_{offset}	parameter controlling the offset of the bathymetry [m]
H_{scale}	parameter controlling the scale of the bathymetry [m]
C	steepness parameter

1

Introduction

1.1. Estuaries

There are many different definitions of estuaries, which are used in different fields of study (Valle-Levinson, 2010). For instance, Cameron and Pritchard (1983) define an estuary as "a semi-enclosed coastal body of water which has a free connection with the open sea and within which sea water is measurably diluted with fresh water from land drainage". On the other hand, Fairbridge (1980) defines an estuary as the part of a river starting at the mouth and ending at the point where tides cease to influence the flow of water (i.e. because of friction). This is the definition used in this thesis. Examples of estuaries are shown in Figure 1.1.

(a) Scheldt, the Netherlands & Belgium (b) Hudson, USA

Figure 1.1: Satellite image of the Scheldt and Hudson estuaries. Obtained using Google Earth (Google, n.d.).

For many reasons, estuaries are important regions to study. They support some of the world's busiest ports, such as the ports of Antwerp, New York City and Shanghai, located in the Scheldt, Hudson and Yangtze estuaries, respectively. Furthermore, estuaries are some of the most productive habitats on the planet due to a large supply of nutrients from runoff (Cloern et al., 2014), serve as breeding grounds for many species of fish and crustaceans (Van Damme et al., 2005), and estuarine ecosystems are among the most valuable in the world (Costanza et al., 1997).

Both the economic and ecological functions of estuaries are significantly affected by the (tidally driven) water motion, or *hydrodynamics* in estuaries, both directly and indirectly. For instance, the environments around estuaries are at risk of flooding (Fairchild et al., 2021) and transport of sediment, salt and pollutants can have adverse effects for ecosystems and human populations alike (Kromkamp & Peene, 1995; Alam et al., 2017; Sunderland et al., 2019).

The hydrodynamics is in turn influenced by a plethora of factors, among which the shape of the river bed: the bathymetry (Li & Valle-Levinson, 1999). Many studies have investigated the periodic tidal motion in estuaries with general bathymetries (Li & Valle-Levinson, 1999; Winant, 2007; Ensing et al., 2015; Kumar et al., 2016), but a lot is still unknown about the sensitivity of the hydrodynamics to the steepness of the bathymetry. Furthermore, it is unclear what exact role momentum advection, the transport of momentum through the flow of water, plays in driving a stationary residual flow, especially in estuaries with steep bathymetries. This residual flow, which comes about due to the non-linear nature of advection, plays a crucial role in many transport processes, since the residual flow drives *net* transport. Work has been done researching residual flow, but many focus on density-driven flows (Burchard & Schuttelaars, 2012; Lerczak & Geyer, 2004). The studies that do focus on advection-driven residual flow often use two-dimensional models (Huijts et al., 2009; Li & O'Donnell, 2005), whose results can differ significantly from three-dimensional models that capture the full spatial structure of the flow (Rozendaal et al., 2024), or focus on longitudinally varying bathymetries (Ianniello, 1979). The aim of this thesis is to shed light on the role of lateral bathymetry steepness and its effect on advection in the three-dimensional hydrodynamics of estuaries.

1.2. Existing models for estuarine hydrodynamics

Mathematical models are excellent tools for researching the water motion in estuaries: mathematical models can be applied to hypothetical situations, which is useful for, among other things, studying the sensitivity of the water motion to parameters such as the steepness of bathymetry, for predicting the effects of changes to the shape of estuaries (e.g. deepening them to allow larger ships to pass through), and isolating the dominant physical processes that lead to specific patterns in the water flow. Mathematical models for estuarine hydrodynamics can be ordered based on their purpose (Murray, 2003), with *simulation models* at one extreme end, and *idealised models* at the other.

Simulation models like Delft3D (Lesser et al., 2004) and Telemac (Villaret et al., 2013) are designed to make accurate predictions that match observations quantitatively. They achieve this by resolving a large range of physical scales and including a wide variety of physical processes. This makes them applicable to many different situations. However, simulation models come with large computational costs, which makes studies that require large numbers of tests, such as parameter sensitivity studies, prohibitive. Furthermore, due to the complexitiy of such models, the results of simulation models are difficult to analyse systematically. Therefore, simulation models are less suitable to gain insight into the physical mechanisms involved in the hydrodynamics.

Idealised models, such as the model from Winant (2007) and iFlow (Dijkstra et al., 2017), on the other hand, are designed specifically for this purpose. By focusing on the dominant physical processes and making many simplifications, idealised models become fast enough for parameter sensitivity studies. Often, these types of models are solved semi-analytically. For instance, many idealised models make use of perturbation techniques based on scaling assumptions. These methods allow non-linear terms to be dealt with by viewing them as an infinite sum of linear ones (Holmes, 2013). Using perturbation methods also result in a clear cause-and-effect structure, which aids analysis of the results. However, because of the large number of simplifications and scaling assumptions, idealised models are often only able to reproduce observations qualitatively, and they are accurate in fewer situations than simulation models.

Both types of models are still unsuited to studying the (combined) effects of steep bathymetries and advection: simulation models are not suitable for systematic analysis in general and current idealised models are inaccurate if non-linear processes such as advection become dominant (leading-order), which might very well be the case in estuaries with steep bathymetries. Thus, a new type of idealised model that can handle leading-order non-linearities accurately is necessary to study these types of situations.

1.3. Research questions

The final goal of the thesis is to understand the sensitivity of the three-dimensional hydrodynamics to the steepness of the bathymetry. To achieve this, a model that can handle leading-order non-linearities accurately is developed. The final goal can be subdivided in two more specific research questions:

Q1: How does the steepness of the bathymetry affect the periodic tidal flow?

Q2: What residual flow patterns emerge due to momentum advection from the periodic tidal motion, and how are they affected by the bathymetric steepness?

The structure of the thesis is as follows. First, Chapter 2 describes the model equations and boundary condition. Subsequently, Chapter 3 discusses the methods used to solve the model equations, after which Chapter 4 presents the results of the experiments. In Chapter 5, the results are embedded into the literature and an outlook for future research is given, and finally, Chapter 6 summarises the conclusions and answers the research questions.

2

Model Formulation

This chapter describes the new mathematical model of estuarine hydrodynamics, including a definition of the domain (Section 2.1), the model equations (Section 2.2), and boundary conditions (Section 2.3).

2.1. Mathematical description of the domain

To describe the estuarine domain mathematically, let $D_{2\mathrm{D}} \subseteq \mathbb{R}^2$ be a connected set that delineates the (horizontal) shape of the estuary. In principle, the set $D_{2\mathrm{D}}$ can be geometrically complex. Furthermore, let $H(x, y)$ be the (positive) water depth, and let $\zeta(x, y, t)$ be the time-dependent water surface elevation above the mean water level, which is assumed to be at 0 m. Then the full domain is given by

$$D = \left\{(x, y, z, t) \in D_{2\mathrm{D}} \times \mathbb{R} \times [0, \infty) : -H(x, y) \leq z \leq \zeta(x, y, t) \text{ for all } (x, y, t) \in D_{2\mathrm{D}} \times [0, \infty)\right\}. \tag{2.1}$$

Here, the surface elevation ζ is an unknown, and is obtained by solving the model equations given in Section 2.2. Figure 2.1 gives a schematic overview of an example domain D.

Because the surface of the Earth is (approximately) spherical, spherical coordinates should be used. However, Cartesian coordinates x, y and z are used instead, since estuaries are small enough to warrant approximating the Earth's surface by a flat plane. Here, x and y are the horizontal coordinates, and z is the vertical coordinate pointing upwards. The orientation of the horizontal coordinates can be chosen freely.

The boundary Γ of the two-dimensional domain $D_{2\mathrm{D}}$ can be partitioned into three parts: a part Γ_s that connects to the sea, a part Γ_r that connects to the river, and a part Γ_c that consists of the closed boundary representing the banks of the river. Similar to (2.1), three-dimensional analogues can be defined:

$$\partial D_s = \left\{(x, y, z, t) \in \Gamma_s \times \mathbb{R} \times [0, \infty) : -H(x, y) \leq z \leq \zeta(x, y, t) \text{ for all } (x, y, t) \in \Gamma_s \times [0, \infty)\right\}, \tag{2.2a}$$

$$\partial D_r = \left\{(x, y, z, t) \in \Gamma_r \times \mathbb{R} \times [0, \infty) : -H(x, y) \leq z \leq \zeta(x, y, t) \text{ for all } (x, y, t) \in \Gamma_r \times [0, \infty)\right\}, \tag{2.2b}$$

$$\partial D_c = \left\{(x, y, z, t) \in \Gamma_c \times \mathbb{R} \times [0, \infty) : -H(x, y) \leq z \leq \zeta(x, y, t) \text{ for all } (x, y, t) \in \Gamma_c \times [0, \infty)\right\}. \tag{2.2c}$$

2.2. Model equations

In this thesis, the three-dimensional Reynolds-averaged shallow water equations are used. Turbulent eddies are parametrised as additional viscosity, and the associated *eddy viscosity* is assumed to be constant in time and space. Furthermore, the f-plane approximation is used and horizontal eddy viscosity terms are neglected. To focus on advection-driven residual flows, salinity gradients are neglected as well. Appendix A contains a derivation and explanation of these equations, starting from the Navier-Stokes equations which represent conservation of mass and momentum for fluids, and subsequently making various simplifications.

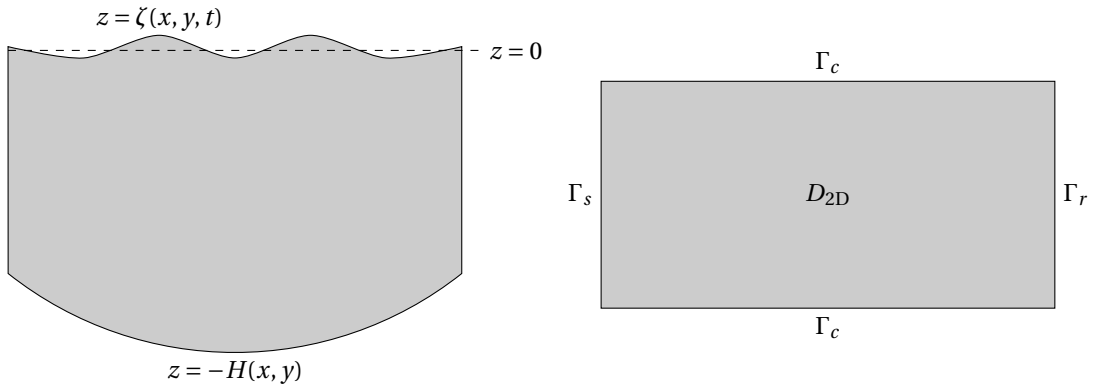

(a) Cross-section (b) Bird's eye view

Figure 2.1: Schematic overview of the domain D, seen from two different perspectives: a cross-section (a) and a bird's eye view (b).

The (as of yet unclosed) 3D-shallow water equations are given by

$$\nabla \cdot \mathbf{u} = 0, \tag{2.3a}$$

$$u_t + \varepsilon(uu_x + vu_y + wu_z) - fv = -g\zeta_x + \mathscr{A}_v u_{zz}, \tag{2.3b}$$

$$v_t + \varepsilon(uv_x + vv_y + wv_z) + fu = -g\zeta_y + \mathscr{A}_v v_{zz}. \tag{2.3c}$$

Here, $\mathbf{u} = (u, v, w)$ is the flow velocity vector, f is the Coriolis frequency, g is the gravitational acceleration, and $\mathscr{A}_v$ is the vertical eddy viscosity. Equation (2.3a) is the *continuity equation* and represents conservation of mass. Equations (2.3b-c) are the *momentum equations* and, unsurprisingly, represent conservation of momentum.

In the momentum equations (2.3b-c), non-linearities are present in the form of products of flow velocities. These terms are called the *advective terms*, and model the transport of momentum caused by the water motion, a process also known as *advection*. The advective terms are multiplied with the parameter ε, which has no physical meaning. This parameter is used to control the strength of momentum advection. This is necessary for convergence of the solution method (see Subsection 4.3.1).

The other terms in the equations are referred to (from left to right starting from the terms with f) as the *Coriolis terms*, accounting for the Earth's rotation, the *barotropic pressure gradient*, the depth-independent pressure gradient due to water surface variations, and finally, the *eddy viscosity term* dissipating energy through internal friction and turbulent eddies.

2.3. Boundary conditions

Firstly, velocities are required to vanish at the bed, i.e.

$$u = v = w = 0, \qquad \text{at } z = -H. \tag{2.4}$$

This is called the *no-slip condition* and models the fact that viscous fluids stick to solid surfaces (Day, 1990; Sochi, 2011).

Furthermore, it is assumed that a water particle on the water surface always remains part of the water surface. Mathematically, this means that for a particle on the surface with horizontal position (x_p, y_p) at any point in time t, the vertical position z_p is given by $z_p = \zeta(x_p, y_p, t)$. Taking the material derivative of this expression leads to a kinematic boundary condition in terms of the flow variables:

$$w = \zeta_t + u\zeta_x + v\zeta_y, \qquad \text{at } z = \zeta. \tag{2.5}$$

Because focus is put upon tidal flows and residual flows due to momentum advection, it is assumed that no wind is present, and thus, the flow experiences no shear stress at the water surface: $\tau^{\text{wind},x} = \tau^{\text{wind},y} = 0$. By using the assumption that turbulent water may be seen as a Newtonian fluid (see Section A.3 in Appendix A),

one can derive that

$$\mathscr{A}_v u_z = \mathscr{A}_v v_z = 0, \qquad \text{at } z = \zeta. \tag{2.6}$$

At the seaward boundary ∂D_s, the water motion will be forced by the semidiurnal tide (M_2), that is, the tide with a period of half a (lunar) day, and its overtides ($M_4, M_6, \ldots$), possibly including a residual/subtidal component (M_0). Mathematically, this can then be expressed as a Fourier series:

$$\zeta(x,y,t) = \sum_{i=0}^{\infty} A_{M_{2i}}(x,y)\cos\left(2\pi\sigma i\left(t-\theta_{M_{2i}}(x,y)\right)\right), \qquad (x,y)\in\Gamma_s. \tag{2.7}$$

Here, $A_{M_{2i}}$ is the tidal forcing amplitude of component M_{2i}, $\theta_{M_{2i}}$ is the phase. The parameter σ is the frequency of the M_2-tide, and is equal to $2.236\cdot10^{-5}$ s^{-1} (see Table 3.2 in Gerkema (2019)). Temporal changes in the amplitudes $A_{M_{2i}}$ due to e.g. the spring-neap cycle (Gerkema, 2019) are neglected.

At the closed boundaries, an impermeability condition will be imposed, that is, water is not allowed to flow through:

$$\mathbf{u}\cdot\mathbf{n} = 0, \qquad (x,y)\in\Gamma_c\cup\Gamma_r,\ z\in[-H,0] \tag{2.8}$$

where $\mathbf{n}$ is the outward-pointing normal vector. Since the closed boundaries ∂D_c are assumed to be perfectly straight vertical walls, the normal vector has no vertical component. River discharge is neglected, such that residual (stationary) flow is the result of non-linear interactions alone.

The model equations (2.3a-c) also contain time derivatives. To close the equations, initial conditions are theoretically also necessary. However, the solution methods described in Chapter 3 only solve the equilibrium flow, and disregard the transient solution. Therefore, it is not necessary to impose initial conditions.

To resolve the water surface elevation ζ, equations (2.3a-c) are not sufficient. In addition to (2.3a-c), the kinematic surface boundary condition (2.5) can be viewed as a model equation. However, the form of (2.4) makes it difficult to use as a model equation, since flow velocities would have to be evaluated at the dynamic water surface. Instead, it is possible to derive an equivalent expression in terms of depth-integrated quantities. Moreover, this equation is more suitable for interpretation of solutions, since the vertical velocity is absent.

To start, integrate the continuity equation (2.3a) over the water depth:

$$\begin{aligned}\int_{-H}^{\zeta}\nabla\cdot\mathbf{u}\,\mathrm{d}z &= \int_{-H}^{\zeta}u_x\,\mathrm{d}z+\int_{-H}^{\zeta}v_y\,\mathrm{d}z+[w]_{-H}^{\zeta}\\ \text{((2.4) and (2.5))} &= \int_{-H}^{\zeta}u_x\,\mathrm{d}z+\int_{-H}^{\zeta}v_y\,\mathrm{d}z+\zeta_t+u\zeta_x+v\zeta_y.\end{aligned}$$

Now, application of the Leibniz integration rule leads to the so-called *depth-integrated continuity equation*:

$$\zeta_t+\left(\int_{-H}^{\zeta}u\,\mathrm{d}z\right)_x+\left(\int_{-H}^{\zeta}v\,\mathrm{d}z\right)_y=0. \tag{2.9}$$

Physically, this means that whenever there is non-zero divergence (i.e. a sink or a source) in the depth-integrated water flow, the water level should rise or fall accordingly. This is an inevitable consequence of the incompressibility assumption.

In principle, the velocities should be integrated from z to the dynamic water surface ζ. However, to focus the analysis on advection, this non-linear contribution of ζ is neglected and the upper limits of integrals are equal to the mean sea level at $z=0$. Similarly, when flow velocities should be evaluated at $z=\zeta$, they are evaluated at $z=0$ instead. In many cases, this approximation is justified by a scaling analysis, see for example Dijkstra et al. (2017).

3

Solution methods

Now that the model equations (2.3a-c) and their boundary conditions have been defined, the solution method for the model will be presented. Before all the details are discussed, we first explain the idea of the method, which is based on Dijkstra et al. (2022).

We look for solutions that are in dynamic equilibrium, that is, solutions that are T-periodic, where $T = \sigma^{-1}$ is the period of the semidiurnal tide. Periodic behaviour on longer time scales such as the spring-neap cycle, and transient parts of the solution are neglected. Therefore, it is possible to write the solution as a Fourier series with the M_2-tidal frequency σ as fundamental frequency.

Furthermore, the solution can be written as an (infinite) linear combination of orthogonal basis functions in the vertical coordinate z. Because of orthogonality, the matrices that have to be solved at the end of the method are sparse. Also, the vertical dependence of the solution is always smooth, no matter the number of basis functions taken into account.

Once the equations have been projected onto these bases, the resulting system of two-dimensional PDEs is discretised using a spectral element method (SEM), which is a variant of the finite element method, and solved using the Newton-Raphson method. The spectral element method allows for geometrically complex domains, which makes our method suited to modelling realistic estuaries.

After a helpful coordinate transformation is introduced in Section 3.1, Section 3.2 details the projection of the model equations and boundary conditions onto the Fourier and vertical bases using a technique called Galerkin projection. After projection, the spectral element method and the Newton-Raphson method applied to non-linear PDEs are discussed briefly in Sections 3.3 and 3.4, respectively.

3.1. The vertical ς-coordinate transformation

The vertical range of the domain D is given by $z \in [-H(x,y), 0]$, for any $(x,y) \in D_{2\mathrm{D}}$. In order to define and perform operations on a vertical orthogonal basis, it will be beneficial to transform the z-coordinate in such a way that the domain D can be written as $D = D_{2\mathrm{D}} \times [-1,0] \times [0,\infty)$. To this end, ς-*coordinates*, first introduced by Phillips (1957) will be used[1].

Assume that the model was written in the coordinate system $(\hat{x}, \hat{y}, \hat{z}, \hat{t})$. The new coordinate system (x, y, ς, t) is defined as

$$x(\hat{x}, \hat{y}, \hat{z}, \hat{t}) = \hat{x}, \tag{3.1a}$$

$$y(\hat{x}, \hat{y}, \hat{z}, \hat{t}) = \hat{y}, \tag{3.1b}$$

$$\varsigma(\hat{x}, \hat{y}, \hat{z}, \hat{t}) = \frac{\hat{z}}{H(\hat{x}, \hat{y})} = \frac{\hat{z}}{H(x,y)}, \tag{3.1c}$$

$$t(\hat{x}, \hat{y}, \hat{z}, \hat{t}) = \hat{t}. \tag{3.1d}$$

[1] Usually, ς-coordinates are denoted by σ, but since this symbol is already used in this work, alternative notation is used.

Note that $\varsigma \in [-1,0]$, since $\varsigma(\hat{x},\hat{y},0,t) = 0$ and $\varsigma(\hat{x},\hat{y},-H(\hat{x},\hat{y}),\hat{t}) = -1$, so this coordinate system satisfies our requirements. Using the chain rule, partial derivatives in the old coordinates may be rewritten to coordinate system (3.1):

$$\frac{\partial}{\partial \hat{x}} = \frac{\partial}{\partial x}\frac{\partial x}{\partial \hat{x}} + \frac{\partial}{\partial y}\frac{\partial y}{\partial \hat{x}} + \frac{\partial}{\partial \varsigma}\frac{\partial \varsigma}{\partial \hat{x}} + \frac{\partial}{\partial t}\frac{\partial t}{\partial \hat{x}} = \frac{\partial}{\partial x} - \varsigma\frac{H_x}{H}\frac{\partial}{\partial \varsigma}, \tag{3.2a}$$

$$\frac{\partial}{\partial \hat{y}} = \frac{\partial}{\partial x}\frac{\partial x}{\partial \hat{y}} + \frac{\partial}{\partial y}\frac{\partial y}{\partial \hat{y}} + \frac{\partial}{\partial \varsigma}\frac{\partial \varsigma}{\partial \hat{y}} + \frac{\partial}{\partial t}\frac{\partial t}{\partial \hat{y}} = \frac{\partial}{\partial y} - \varsigma\frac{H_y}{H}\frac{\partial}{\partial \varsigma}, \tag{3.2b}$$

$$\frac{\partial}{\partial \hat{z}} = \frac{\partial}{\partial x}\frac{\partial x}{\partial \hat{z}} + \frac{\partial}{\partial y}\frac{\partial y}{\partial \hat{z}} + \frac{\partial}{\partial \varsigma}\frac{\partial \varsigma}{\partial \hat{z}} + \frac{\partial}{\partial t}\frac{\partial t}{\partial \hat{z}} = \frac{1}{H}\frac{\partial}{\partial \varsigma}, \tag{3.2c}$$

$$\frac{\partial}{\partial \hat{t}} = \frac{\partial}{\partial x}\frac{\partial x}{\partial \hat{t}} + \frac{\partial}{\partial y}\frac{\partial y}{\partial \hat{t}} + \frac{\partial}{\partial \varsigma}\frac{\partial \varsigma}{\partial \hat{t}} + \frac{\partial}{\partial t}\frac{\partial t}{\partial \hat{t}} = \frac{\partial}{\partial t}. \tag{3.2d}$$

Before substituting (3.2a-d) into the model, Burchard and Petersen (1997) suggest using an alternative definition of the vertical velocity, given by

$$\tilde{\omega} = \frac{1}{H}\left(w - \varsigma u H_x - \varsigma v H_y\right). \tag{3.3}$$

The velocity $\tilde{\omega}$ has two main benefits over w. Firstly, the kinematic boundary condition at the river bed (2.4) turns into the simple condition $\tilde{\omega} = 0$. Moreover, the use of (3.3) causes convenient cancellations after substitution of (3.2) into the model equations. Following Burchard and Petersen (1997), the model equations in ς-coordinates are given by

$$(Hu)_x + (Hv)_y + H\tilde{\omega}_\varsigma = 0, \tag{3.4a}$$

$$Hu_t + (Hu^2)_x + (Huv)_y + H(u\tilde{\omega})_\varsigma - fHv = -gH\zeta_x + \frac{\mathscr{A}_v}{H}u_{\varsigma\varsigma}, \tag{3.4b}$$

$$Hv_t + (Huv)_x + (Hv^2)_y + H(v\tilde{\omega})_\varsigma + fHu = -gH\zeta_y + \frac{\mathscr{A}_v}{H}v_{\varsigma\varsigma}, \tag{3.4c}$$

$$\zeta_t + \left(H\int_{-1}^{0} u \,\mathrm{d}\varsigma\right)_x + \left(H\int_{-1}^{0} v \,\mathrm{d}\varsigma\right)_y = 0. \tag{3.4d}$$

Equations (3.4a-d) are subject to the following transformed boundary conditions:

$$\tilde{\omega} = 0, \qquad \varsigma = -1, \tag{3.5a}$$

$$\frac{\mathscr{A}_v}{H}u_\varsigma = \frac{\mathscr{A}_v}{H}v_\varsigma = 0, \qquad \varsigma = 0, \tag{3.5b}$$

$$u = v = 0, \qquad \varsigma = -1, \tag{3.5c}$$

$$\zeta = \sum_{i=0}^{i_{\max}} A_{M_{2i}} \cos\left(2\pi\sigma i\left(t - \theta_{M_{2i}}\right)\right), \qquad (x,y) \in \Gamma_s, \tag{3.5d}$$

$$\mathbf{u}\cdot\mathbf{n} = 0, \qquad (x,y) \in \Gamma_c \cup \Gamma_r,\ \varsigma \in [-1,0]. \tag{3.5e}$$

Note that the tidal forcing boundary condition (3.5d) is truncated at $i_{\max} \in \mathbb{N}$ rather than prescribing infinitely many harmonic modes.

3.2. Galerkin projection

The unknowns u, v and ζ are written as truncated series expansions in terms of the temporal basis functions $h_i(t)$, $i = -i_{\max},\ldots,i_{\max}$ and vertical basis functions $f_m(\varsigma)$, $m = 1,\ldots,M$:

$$u(x,y,\varsigma,t) = \sum_{m=1}^{M}\sum_{i=-i_{\max}}^{i_{\max}} \alpha_{mi}(x,y) f_m(\varsigma) h_i(t), \tag{3.6a}$$

$$v(x,y,\varsigma,t) = \sum_{m=1}^{M}\sum_{i=-i_{\max}}^{i_{\max}} \beta_{mi}(x,y) f_m(\varsigma) h_i(t), \tag{3.6b}$$

$$\zeta(x,y,t) = \sum_{i=-i_{\max}}^{i_{\max}} \gamma_i(x,y) h_i(t). \tag{3.6c}$$

where α_{mi}, β_{mi} and γ_i are the spatially varying coefficients associated to each combination of temporal and vertical basis functions, and M and $i_{\max}$ are the number of vertical and temporal basis functions taken into account, respectively. If α_{mi}, β_{mi} and γ_i are known exactly, the basis expansions (3.6) converge to the exact solution in the limit as $M, i_{\max} \to \infty$. The vertical basis functions f_m, $m \in \mathbb{N}$ and Fourier basis functions h_i, $i \in \mathbb{Z}$ are defined in Subsection 3.2.1. Note that the vertical velocity $\tilde{\omega}$ is absent from (3.6a-c), since an analytical expression for $\tilde{\omega}$ in terms of the coefficients α_{mi} and β_{mi} follows from the continuity equation (2.3a). This expression is derived in detail in Subsection 3.2.2. Subsection 3.2.3 describes the projection of the model equations and boundary conditions onto the bases. This is achieved using a technique called *Galerkin projection*, which is explained below. Finally, the weak formulations of the resulting equations that are necessary for the spectral element method are derived in Subsection 3.2.4.

By representing the unknowns as finite linear combinations of basis functions, they are approximated in a finite-dimensional subspace of the full infinite-dimensional solution space. For general solutions, this finite representation cannot be exact. Instead, the coefficients of each basis function must be chosen so that the finite-dimensional representation matches the full solution as closely as possible, in some sense.

The *method of weighted residuals* (Karniadakis & Sherwin, 1999, pg. 18) is one method to achieve this. Let V be a Hilbert space with inner product $(\cdot,\cdot)_V$ and norm $\|\cdot\|_V = \sqrt{(\cdot,\cdot)_V}$,and let $V_n := \text{Span}\{\psi_j\}_{j=1}^n$ with $V_n \subseteq V$ be a finite-dimensional subspace. The vector $u \in V$ is approximated by a finite linear combination u_n:

$$u_n := \sum_{j=1}^{n} a_j \psi_j, \tag{3.7}$$

and let $R = u - u_n$ denote the residual. In the method of weighted residuals, the coefficients a_j, $j = 1, \ldots, n$ are chosen to satisfy

$$(v_j, R)_V = 0, \qquad j = 1, \ldots, n, \tag{3.8}$$

where $v_j \in V$ are weight functions. For instance, if V is a function space and v_j are given by Dirac deltas $\delta(x - x_j)$, then the method of weighted residuals becomes a *collocation method*, using which the finite representation is exact at $x = x_j$. The *Galerkin projection* corresponds to the choice $v_j = \psi_j$, $j = 1, \ldots, n$. If $\{\psi_j\}_{j=1}^n$ is an orthogonal basis, then (3.8) reduces to

$$a_j = \frac{(u, \psi_j)_V}{(\psi_j, \psi_j)_V}, \qquad j = 1, \ldots, n, \tag{3.9}$$

and the Galerkin projection is the *orthogonal projection* of V onto V_n, that minimises $\|R\|_V$ (van Neerven, 2022). Galerkin projection can also be applied to equations, where the projection is obtained by multiplying both sides by one of the basis functions and subsequently taking the inner product, which for function spaces is usually defined by integration. In this thesis, the standard L^2-inner products are used, since the basis functions defined in Subsection 3.2.1 are orthogonal with respect to this inner product.

3.2.1. Defining the expansion bases

Since the solutions are T-periodic, they may be written as a Fourier series. Accordingly, the basis functions $h_i(t)$ are of Fourier-type. They are given by:

$$h_i(t) = \begin{cases} \cos(2\pi\sigma i t), & i > 0, \\ \frac{1}{2}\sqrt{2}, & i = 0, \\ \sin(2\pi\sigma i t), & i < 0, \end{cases} \tag{3.10}$$

The function $h_0(t)$ is constant and represents the residual flow, which does not vary with the tide. It is chosen to be equal to $\sqrt{2}/2$ such that the $L^2((0,T)$-norm of every h_i, $i \in \mathbb{Z}$ is equal to $(2\sigma)^{-1}$, for the sake of notational brevity.

Since the flow velocities u and v are subject to boundary conditions on the vertical boundaries $\varsigma = -1$, $\varsigma = 0$, the vertical basis functions are chosen such that they satisfy these conditions. This way, the final solutions satisfy the vertical boundary condition regardless of the coefficients α_{mi} and β_{mi}. To satisfy the no-stress boundary condition (3.5b) at the top of the water column, it must hold that $f_m'(0) = 0$ for all $m = 1, \ldots, M$. The no-slip condition at the bed implies that $f_m(-1) = 0$ for all $m = 1, \ldots, M$.

Now, the functions are defined for all $\varsigma \in [-1,0]$. A desirable property for an expansion basis is orthogonality, since projection of the model on an orthogonal basis leaves the resulting equations as decoupled as possible. Therefore, the f_m, $m = 1,\dots,M$ are chosen to obey the eigenvalue problem

$$f'' = -\lambda f. \tag{3.11}$$

Equation (3.11) combined with the boundary conditions $f(-1) = f'(0) = 0$ is a *regular Sturm-Liouville eigenvalue problem*, which is known to have infinitely many *eigenvalue-eigenfunction pairs* (λ_m, f_m), $m \in \mathbb{N}$ such that the eigenfunctions f_m are pairwise orthogonal with respect to some weighted inner product on $L^2((-1,0))$ (Haberman, 2013). In this case, the orthogonality is with respect to the standard $L^2((-1,0))$-inner product. Additionally, second derivatives of the vertical basis functions appear in the model equations. However, because the eigenvalue problem (3.11) is used to define f_m, $-\lambda f$ can be substituted any time they appear. This leads to simplifications in the projected model equations.

The solutions of the eigenvalue problem (3.11) are given by

$$f_m(\varsigma) = \cos\left(\left(m+\frac{1}{2}\right)\pi\varsigma\right), \qquad \lambda_m = \left(m+\frac{1}{2}\right)^2\pi^2, \tag{3.12}$$

for $m \in \mathbb{N}$. The solution procedure is outlined in Appendix B. Figure 3.1 shows the first four basis functions $f_m(\varsigma)$.

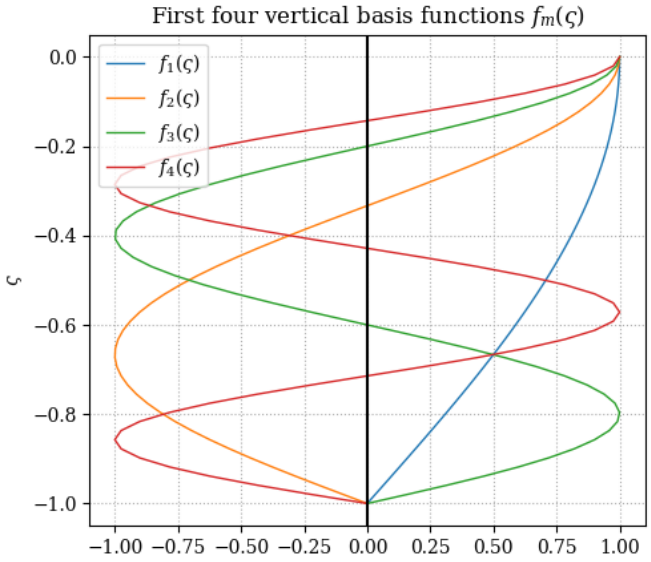

Figure 3.1: The first four solutions to eigenvalue problem (3.11) plotted against ς.

3.2.2. An analytical expression for vertical flow velocity

Using the continuity equation (3.4a), an analytical formula can be derived for $\tilde{\omega}$ in terms of the velocity coefficients α_{mi} and β_{mi}. The notation $\boldsymbol{\alpha}_{mi} = (\alpha_{mi}, \beta_{mi})$ is introduced for brevity.

Substitution of the truncated basis expansions (3.6) into the continuity equation (3.4a) results in

$$\tilde{\omega}_\varsigma = -\frac{1}{H}\sum_{m=1}^{M}\sum_{i=-i_{\max}}^{i_{\max}} \nabla\cdot(H\boldsymbol{\alpha}_{mi}) f_m(\varsigma) h_i(t), \tag{3.13}$$

which can be integrated to obtain

$$\tilde{\omega} = \tilde{C}(x,y,t) - \frac{1}{H}\sum_{m=1}^{M}\sum_{i=-i_{\max}}^{i_{\max}} \nabla\cdot(H\boldsymbol{\alpha}_{mi}) h_i(t) \int_{-1}^{\varsigma} f_m(\varsigma')\,\mathrm{d}\varsigma', \tag{3.14}$$

where $\tilde{C}$ is an integration constant that is later chosen to satisfy the kinematic boundary condition at the bed (3.5a). By the fundamental theorem of calculus, the integral in (3.14) is equal to

$$\int_{-1}^{\varsigma} f_m(\varsigma')\,\mathrm{d}\varsigma' = \frac{2}{(2m+1)\pi}\left[\sin\left(\left(m+\frac{1}{2}\right)\pi\varsigma\right)+(-1)^m\right]. \tag{3.15}$$

Furthermore, (3.14) shows that $\tilde{\omega}(x,y,-1,t)=\tilde{C}(x,y,t)$. To satisfy boundary condition (3.5a), $\tilde{C}$ must be identically equal to zero. In conclusion,

$$\tilde{\omega} = -\frac{1}{H}\sum_{m=1}^{M}\sum_{i=-i_{\max}}^{i_{\max}} \frac{2}{(2m+1)\pi}\nabla\cdot(H\boldsymbol{\alpha}_{mi})h_i(t)\left[\sin\left(\left(m+\frac{1}{2}\right)\pi\varsigma\right)+(-1)^m\right]. \tag{3.16}$$

Using relation (3.3), the actual vertical velocity w can be recovered as well.

3.2.3. Projecting the equations and boundary conditions

In the rest of this chapter, a notational convention inspired by *Einstein summation notation* is used, which allows summations to be notated more efficiently. The summation operator is omitted in favour of specifying the summation indices beforehand. In the following, m and n will be summation indices ranging from 1 to M, and i and j summation indices ranging from $-i_{\max}$ to $i_{\max}$. As an example, the along-channel flow velocity (3.6a) is written in this notation convention as

$$u = \alpha_{mi} f_m h_i.$$

First, the linear depth-integrated continuity equation will be projected. To this end, substitute (3.6a-c) into (3.4d) to obtain

$$\gamma_i \frac{\mathrm{d}h_i}{\mathrm{d}t} + \nabla\cdot(H\boldsymbol{\alpha}_{mi})h_i\int_{-1}^{0} f_m\,\mathrm{d}\varsigma = 0. \tag{3.17}$$

Since (3.17) is already depth-independent, only projection onto the Fourier modes is necessary. To this end, multiply by h_k, $k=-i_{\max},\ldots,i_{\max}$ and integrate over the period $[0,T]$. This yields

$$H^2_{i,k}\gamma_i + H^2_{i,k}\nabla\cdot(H\boldsymbol{\alpha}_{mi})\int_{-1}^{0} f_m\,\mathrm{d}\varsigma = 0, \qquad k=-i_{\max},\ldots,i_{\max}, \tag{3.18}$$

where the integration coefficients $H^1_{i,k}$ and $H^2_{i,k}$ are defined by

$$H^1_{i,k} = \int_0^T h_i h_k\,\mathrm{d}t = (2\sigma)^{-1}\delta_{i,k}, \tag{3.19a}$$

$$H^2_{i,k} = \int_0^T \frac{\mathrm{d}h_i}{\mathrm{d}t} h_k\,\mathrm{d}t = \pi i\delta_{i,-k} = -\pi k\delta_{i,-k}. \tag{3.19b}$$

In (3.19), $\delta_{i,k}$ denotes the Kronecker delta. Rewriting (3.18) using (3.19) then results in $2i_{\max}+1$ two-dimensional PDEs given by

$$-\pi k\gamma_{-k} + \frac{2\cdot(-1)^m}{(2m+1)\pi}(2\sigma)^{-1}\nabla\cdot(H\boldsymbol{\alpha}_{m,k}) = 0, \qquad k=-i_{\max},\ldots,i_{\max}. \tag{3.20}$$

Now, substitution of (3.6) and the expression (3.16) for $\tilde{\omega}$ into the momentum equation for u (3.4b) leads to the double sum

$$\begin{aligned} H\alpha_{mi}\frac{\mathrm{d}h_i}{\mathrm{d}t}f_m + \left[(H\alpha_{mi}\alpha_{nj})_x + (H\alpha_{mi}\beta_{nj})_y\right]h_i h_j f_m f_n - \\ \alpha_{mi}\nabla\cdot(H\boldsymbol{\alpha}_{nj})h_i h_j\left[f_m f_n + \frac{\mathrm{d}f_m}{\mathrm{d}\varsigma}\int_{-1}^{\varsigma} f_n\,\mathrm{d}\varsigma'\right] - \frac{\mathscr{A}_v}{H}\alpha_{mi}h_i\frac{\mathrm{d}^2 f_m}{\mathrm{d}\varsigma^2} \\ -fH\beta_{mi}h_i f_m = -g(\gamma_i)_x h_i. \end{aligned} \tag{3.21}$$

First, (3.21) will be projected onto the Fourier basis functions. The resulting equations are then projected onto the vertical basis[2]. In the derivation of (3.22), the second derivatives of the vertical basis functions are

[2] By Fubini's theorem, projecting the equations onto the vertical basis first would lead to the same results.

interchanged with $-\lambda_m f_m$. All this results in

$$\begin{aligned} HG^1_{m,\ell}H^2_{i,k}\alpha_{mi} + G^2_{m,n,\ell}H^3_{i,j,k}\left[(H\alpha_{mi}\alpha_{nj})_x + (H\alpha_{mi}\beta_{nj})_y\right] - \\ H^3_{i,j,k}(G^2_{m,n,\ell} + G^3_{m,n,\ell})\alpha_{mi}\nabla\cdot(H\boldsymbol{\alpha}_{nj}) + \frac{\lambda_m \mathscr{A}_v}{H}G^1_{m,\ell}H^1_{i,k}\alpha_{mi} - \\ fH^1_{i,k}G^1_{i,k}\beta_{mi} = -gH^1_{i,k}(\gamma_i)_x\int_{-1}^{0} f_m \,\mathrm{d}\varsigma, \end{aligned} \tag{3.22}$$

for $k = -i_{\max},\ldots,i_{\max}$ and $\ell = 1,\ldots,M$. In the same way as (3.22), the momentum equation for v (3.4c) can be written as

$$\begin{aligned} HG^1_{m,\ell}H^2_{i,k}\beta_{mi} + G^2_{m,n,\ell}H^3_{i,j,k}\left[(H\beta_{mi}\alpha_{nj})_x + (H\beta_{mi}\beta_{nj})_y\right] - \\ H^3_{i,j,k}(G^2_{m,n,\ell} + G^3_{m,n,\ell})\beta_{mi}\nabla\cdot(H\boldsymbol{\alpha}_{nj}) + \frac{\lambda_m \mathscr{A}_v}{H}G^1_{m,\ell}H^1_{i,k}\beta_{mi} + \\ fH^1_{i,k}G^1_{i,k}\alpha_{mi} = -gH^1_{i,k}(\gamma_i)_y\int_{-1}^{0} f_m \,\mathrm{d}\varsigma, \end{aligned} \tag{3.23}$$

for $k = -i_{\max},\ldots,i_{\max}$ and $\ell = 1,\ldots,M$.

The new integration coefficients are defined by

$$G^1_{m,\ell} = \int_{-1}^{0} f_m f_\ell \,\mathrm{d}\varsigma = \frac{1}{2}\delta_{m,\ell}, \tag{3.24a}$$

$$\begin{aligned} G^2_{m,n,\ell} = \int_{-1}^{0} f_m f_n f_\ell \,\mathrm{d}\varsigma = \frac{1}{4}\Bigg[&\frac{(-1)^{m+n+\ell+1}}{(m+n+\ell+\frac{3}{2})\pi} + \frac{(-1)^{m+n-\ell}}{(m+n-\ell+\frac{1}{2})\pi} \\ &+ \frac{(-1)^{m-n+\ell}}{(m-n+\ell+\frac{1}{2})\pi} + \frac{(-1)^{m-n-\ell+1}}{(m-n-\ell-\frac{1}{2})\pi}\Bigg], \end{aligned} \tag{3.24b}$$

$$\begin{aligned} G^3_{m,n,\ell} = \int_{-1}^{0}\frac{\mathrm{d}f_m}{\mathrm{d}\varsigma}\int_{-1}^{\varsigma} f_n \,\mathrm{d}\varsigma' f_\ell \,\mathrm{d}\varsigma = \frac{2m+1}{8n+4}\Bigg[&\frac{(-1)^{m-n+\ell+1}}{(m-n+\ell+\frac{1}{2})\pi} + \frac{(-1)^{m+n+\ell+1}}{(m+n+\ell+\frac{3}{2})\pi} + \\ &\frac{(-1)^{m-n-\ell}}{(m-n-\ell-\frac{1}{2})\pi} + \frac{(-1)^{m+n-\ell}}{(m+n-\ell+\frac{1}{2})\pi}\Bigg] + \frac{2m+1}{4n+2}\Bigg[\frac{(-1)^{m+n+\ell}-1}{(m+\ell+1)\pi} + \\ &(1-\delta_{m,\ell})\frac{(-1)^{m+n-\ell+1}-1}{(m-\ell)\pi}\Bigg], \end{aligned} \tag{3.24c}$$

$$H^3_{i,j,k} = \int_0^{\sigma^{-1}} h_i h_j h_k \,\mathrm{d}t = \begin{cases} (4\sigma)^{-1}\mathbb{1}_{\{i=j+k \text{ or } j=i+k \text{ or } k=i+j\}}, & i,j,k \geq 0, \\ (4\sigma)^{-1}\left(\mathbb{1}_{\{k=-i+j \text{ or } j=-i+k\}} - \mathbb{1}_{\{i=-j-k\}}\right), & i \geq 0, j,k < 0, \\ 0, & \text{otherwise.} \end{cases} \tag{3.24d}$$

The shallow water equations have now been reformulated in terms of the coefficients α_{mi}, β_{mi} and γ_i. Furthermore, the boundary conditions at the vertical boundaries $\varsigma = -1$ and $\varsigma = 0$ are captured by the basis functions $f_m(\varsigma)$. The lateral boundary conditions (3.5e-g) still have to be expressed in terms of the new unknowns.

Firstly, by standard trigonometric identities, the tidal forcing boundary condition may be rewritten as:

$$\zeta = \sum_{i=0}^{i_{\max}} A_{M_{2i}} h_i(\theta_{M_{2i}})h_i(t) + A_{M_{2i}} h_{-i}(\theta_{M_{2i}})h_{-i}(t), \qquad (x,y) \in \Gamma_s. \tag{3.25}$$

Then, if

$$A_i := A_{M_{2|i|}} h_i(\theta_{M_{2|i|}}),$$

Galerkin projection results in

$$H^1_{i,k}\gamma_i = H^1_{i,k}A_i, \tag{3.26}$$

which implies $\gamma_k = A_k$ for $k = -i_{\max},\ldots,i_{\max}$ and $(x,y) \in \Gamma_s$.

For the normal flow conditions (3.5f-g), the same methods as for the model equations are used. Because the three-dimensional normal vector $\mathbf{n}$ has no vertical component since the riverine boundary is a straight vertical wall, the normal flow conditions immediately translate to conditions for $\boldsymbol{\alpha}_{mi} \cdot \mathbf{n}$. After Galerkin projection onto the Fourier and eigenfunction modes, the following boundary conditions are obtained

$$\boldsymbol{\alpha}_{\ell k} \cdot \mathbf{n} = 0, \qquad (x, y) \in \Gamma_c \cup \Gamma_r, \tag{3.27a}$$

for $k = -i_{\max}, \ldots, i_{\max}$ and $\ell = 1, \ldots, M$.

3.2.4. Weak formulations

To solve the projected system of two-dimensional PDEs, a spectral element method based on the more general Galerkin method is used (Section 3.3). The Galerkin method works with so-called weak formulations of the equations, which are equivalent to the classical formulation for sufficiently smooth solutions (van Neerven, 2022). Weak formulations are derived by multiplying the equations by a *test function* ϕ in a certain function space (usually a variation of the Sobolev space $H^1(D_{2\mathrm{D}})$), integrating over the domain, and finally applying integration by parts, which involves the divergence theorem for dimensions higher than one (van Kan et al., 2005). One further advantage of weak formulations is that *natural boundary conditions* such as (3.27a-b) can be substituted directly into the weak formulation, eliminating the need to handle them separately. *Essential boundary conditions* such as the Dirichlet condition (3.26) have to be treated separately, and thus, the test functions ϕ are assumed to vanish on boundaries that are governed by essential boundary conditions.

First, we derive the weak form of the projected depth-integrated continuity equation (3.20). Since the water surface is subject to an essential boundary condition, the test functions ϕ are assumed to be members of the space $H^1(D_{2\mathrm{D}}; \Gamma_s)$, consisting of H^1-functions that vanish[3] at the seaward boundary Γ_s. After applying the process described before, we obtain

$$-\pi k \int_{D_{2\mathrm{D}}} \gamma_{-k} \phi_k^1 \, \mathrm{d}A = -\frac{1}{2\sigma} \frac{(-1)^m}{(m+\frac{1}{2})\pi} \left[\int_{\Gamma_r} \phi_k^1 H \boldsymbol{\alpha}_{mk} \cdot \mathbf{n} \, \mathrm{d}s - \int_{D_{2\mathrm{D}}} H \left(\alpha_{mk} \frac{\partial \phi_k^1}{\partial x} + \beta_{mk} \frac{\partial \phi_k^1}{\partial y} \right) \mathrm{d}A \right], \tag{3.28}$$

for all $k = -i_{\max}, \ldots, i_{\max}$ and all $\phi_k^1 \in H^1(D_{2\mathrm{D}}; \Gamma_s)$. Here, the notation $\mathrm{d}A$ denotes integration over two-dimensional surfaces, and $\mathrm{d}s$ denotes integration over one-dimensional curves. Since $\boldsymbol{\alpha}_{mk}$ is known on the riverine boundary, the line integral acts as a forcing term in the equation. The superscript of the test function indicates that it belongs to the equations derived from the depth-integrated continuity equation. Similarly, the superscripts 2 and 3 indicate that the test functions belong to the equations derived from the along-channel and cross-channel momentum equations respectively.

Because the momentum equations (3.22) and (3.23) are non-linear, their weak forms are non-linear as well. The test functions of these weak formulations live in the space $H^1(D_{2\mathrm{D}})$, since the horizontal velocities are not subject to any essential boundary conditions. The along-channel momentum equation is given by

$$\begin{aligned}
-\frac{\pi k}{2} \int_{D_{2\mathrm{D}}} \alpha_{\ell,-k} \phi_{\ell k}^2 \, \mathrm{d}A + G_{1,mn\ell} H_{3,ijk} \left(\oint_{\partial D_{2\mathrm{D}}} H \alpha_{mi} \phi_{\ell k}^2 \boldsymbol{\alpha}_{nj} \cdot \mathbf{n} \, \mathrm{d}s - \int_{D_{2\mathrm{D}}} H \alpha_{mi} \boldsymbol{\alpha}_{nj} \cdot \nabla \phi_{\ell k}^2 \, \mathrm{d}A \right) \\
- H_{3,ijk} (G_{1,mn\ell} + G_{2,mn\ell}) \left(\oint_{\partial D_{2\mathrm{D}}} H \alpha_{mi} \phi_{\ell k}^2 \boldsymbol{\alpha}_{nj} \cdot \mathbf{n} \, \mathrm{d}s - \int_{D_{2\mathrm{D}}} H \phi_{\ell k}^2 \nabla \alpha_{mi} \cdot \boldsymbol{\alpha}_{nj} \, \mathrm{d}A - \right. \\
\left. \int_{D_{2\mathrm{D}}} H \alpha_{mi} \boldsymbol{\alpha}_{nj} \cdot \nabla \phi_{\ell k}^2 \, \mathrm{d}A \right) + \frac{\pi^2 \mathscr{A}_v}{4\sigma} \left(\ell + \frac{1}{2} \right)^2 \int_{D_{2\mathrm{D}}} \frac{1}{H} \alpha_{\ell k} \phi_{\ell k}^2 \, \mathrm{d}A - \\
\frac{f}{4\sigma} \int_{D_{2\mathrm{D}}} H \beta_{\ell k} \phi_{\ell k}^2 \, \mathrm{d}A = -\frac{g(-1)^\ell}{2(\ell+\frac{1}{2})\pi\sigma} \int_{D_{2\mathrm{D}}} \frac{\partial \gamma_k}{\partial x} \phi_{\ell k}^2 \, \mathrm{d}A,
\end{aligned} \tag{3.29}$$

for all $k = -i_{\max}, \ldots, i_{\max}$, $\ell = 1, \ldots, M$ and all $\phi_{\ell k}^2 \in H^1(D_{2\mathrm{D}})$. The cross-channel momentum equation has

[3] in the same sense as the definition of the space $H_0^1(\Omega)$ on page 361 of van Neerven (2022).

weak form

$$
\begin{aligned}
-\frac{\pi k}{2}\int_{D_{2\mathrm{D}}}\beta_{\ell,-k}\phi^3_{\ell k}\,\mathrm{d}A + G_{1,mn\ell}H_{3,ijk}\left(\oint_{\partial D_{2\mathrm{D}}}H\beta_{mi}\phi^3_{\ell k}\boldsymbol{\alpha}_{nj}\cdot\mathbf{n}\,\mathrm{d}s - \int_{D_{2\mathrm{D}}}H\beta_{mi}\boldsymbol{\alpha}_{nj}\cdot\nabla\phi^3_{\ell k}\,\mathrm{d}A\right)\\
-H_{3,ijk}(G_{1,mn\ell}+G_{2,mn\ell})\left(\oint_{\partial D_{2\mathrm{D}}}H\beta_{mi}\phi^3_{\ell k}\boldsymbol{\alpha}_{nj}\cdot\mathbf{n}\,\mathrm{d}s - \int_{D_{2\mathrm{D}}}H\phi^3_{\ell k}\nabla\beta_{mi}\cdot\boldsymbol{\alpha}_{nj}\,\mathrm{d}A -\right.\\
\left.\int_{D_{2\mathrm{D}}}H\beta_{mi}\boldsymbol{\alpha}_{nj}\cdot\nabla\phi^3_{\ell k}\,\mathrm{d}A\right) + \frac{\pi^2\mathscr{A}_v}{4\sigma}\left(\ell+\frac{1}{2}\right)^2\int_{D_{2\mathrm{D}}}\frac{1}{H}\beta_{\ell k}\phi^3_{\ell k}\,\mathrm{d}A +\\
\frac{f}{4\sigma}\int_{D_{2\mathrm{D}}}H\alpha_{\ell k}\phi^3_{\ell k}\,\mathrm{d}A = -\frac{g(-1)^\ell}{2(\ell+\frac{1}{2})\pi\sigma}\int_{D_{2\mathrm{D}}}\frac{\partial\gamma_k}{\partial y}\phi^3_{\ell k}\,\mathrm{d}A,
\end{aligned}
\tag{3.30}
$$

for all $k=-i_{\max},\ldots,i_{\max}$, $\ell=1,\ldots,M$ and all $\phi^3_{\ell k}\in H^1(D_{2\mathrm{D}})$.

In (3.29), (3.30), the closed contour integrals act as linear terms for the riverine and closed boundaries, since the normal flow can be substituted. However, no normal flow is prescribed on the seaward boundary, implying that the integral over Γ_s is an additional non-linear term.

3.3. The spectral element method

The spectral element method (SEM) is a method to discretise weak forms of partial differential equations based on the finite element method (FEM), which is in turn based on the method of weighted residuals and Galerkin projection (see Subsection 3.2.3). FEM is a method to generate (continuous) basis functions that are supported on small sets, based on a triangulated mesh of the domain, leading to sparse systems of equations. In SEM, (potentially high order) *orthogonal* polynomials are used to construct the basis. Subsection 3.3.1 describes how this SEM expansion basis is constructed, and after, Subsection 3.3.2 describes how weak forms are solved. Karniadakis and Sherwin (1999) provide additional details about this method; the information in this section is based on their book.

3.3.1. SEM expansion bases

When using SEM (and FEM), the domain of interest Ω must be partitioned into a finite number of *elements*. In one dimension, these elements are intervals, and in two dimensions, elements are usually given by triangles. By using triangles as elements, SEM is able to handle very general domains. An expansion basis can then be constructed on each element separately, after which all element bases (or *local bases*) are combined in such a way that the basis functions of the full basis (or *global basis*) are continuous. The process of constructing the global basis from the local ones is called *assembly*. In this subsection, the construction of a local basis on a one-dimensional element is described first, after which two-dimensional local bases can be considered.

Usually, a local basis is constructed on a standard element and subsequently transformed to general elements by means of a coordinate transformation. For one-dimensional domains, the standard element is the interval $[-1,1]$. In many versions of FEM, the only two basis functions considered on this interval are the linear functions

$$
\xi\mapsto\frac{1-\xi}{2}, \qquad\qquad \xi\mapsto\frac{1+\xi}{2}.
$$

However, SEM makes use of higher order polynomials as well. Often, these higher order polynomials are chosen from a family of orthogonal polynomials, such as *Legendre polynomials* $P_p(\xi)$ or *Jacobi polynomials* $P_p^{\alpha,\beta}(\xi)$, which are the solutions of the Sturm-Liouville problem

$$
\frac{\mathrm{d}}{\mathrm{d}\xi}\left[(1-\xi)^{1+\alpha}(1+\xi)^{1+\beta}\frac{\mathrm{d}}{\mathrm{d}\xi}P_p^{\alpha,\beta}(\xi)\right] = \lambda_p(1-\xi)^\alpha(1+\xi)^\beta P_p^{\alpha,\beta}(\xi),
\tag{3.31}
$$

with $\lambda_p=-p(\alpha+\beta+p+1)$ and where p denotes the order of the polynomials. The orthogonality (w.r.t. a weighted inner product) of these functions benefits the sparsity of the eventual linear system to solve.

A commonly used one-dimensional SEM expansion basis of order P is given by

$$\phi_p(\xi) = \begin{cases} \dfrac{1-\xi}{2}, & p = 1, \\ \left(\dfrac{1-\xi}{2}\right)\left(\dfrac{1+\xi}{2}\right) P_{p-1}^{1,1}(\xi), & p = 2,\ldots,P-1, \\ \dfrac{1+\xi}{2}, & p = P. \end{cases} \tag{3.32}$$

Other types of bases, for example based on Lagrangian interpolation, are used as well.

Once the local basis is mapped to every element, a continuous global basis can be constructed. The only local basis functions that are non-zero at the element boundaries are the linear ones ($p = 1$, $p = P$). Thus, to satisfy global continuity, the two linear basis functions that are nonzero at element boundaries must be joined together. This creates piecewise linear function that bear resemblence to tents. The higher-order functions can be incorporated into the continuous global basis by restriction to their respective elements. An example of a second-order SEM basis is given in Figure 3.2. The construction of two-dimensional SEM

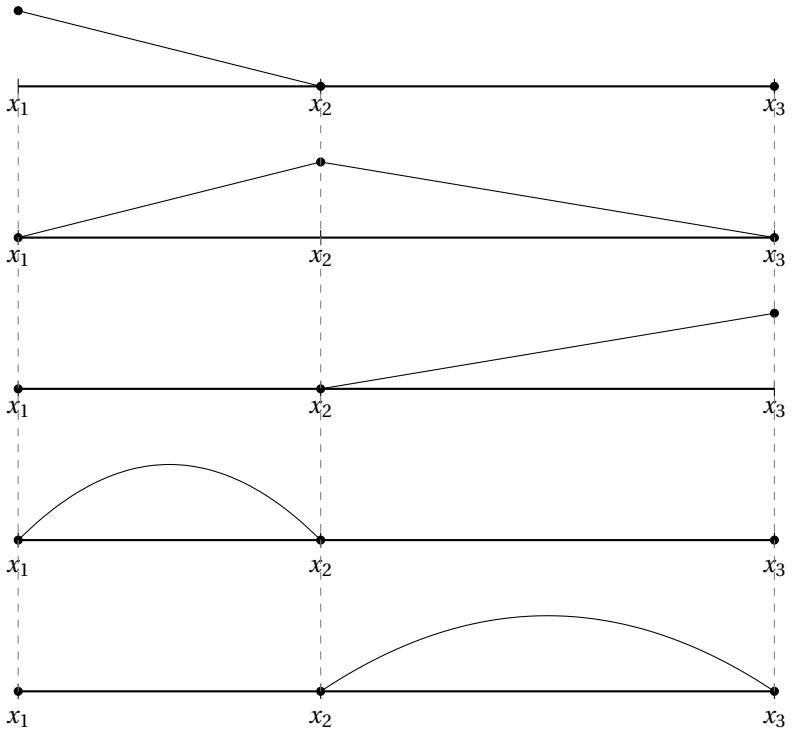

Figure 3.2: The basis functions of a second-order SEM expansion basis on $\Omega = [x_1, x_3]$ with elements $[x_1, x_2]$ and $[x_2, x_3]$.

expansion bases follows along similar lines as the construction of the one-dimensional bases. Firstly, since the two-dimensional standard element is a triangle, *barycentric coordinates* $(\Lambda_1, \Lambda_2, \Lambda_3)$ are used[4], which for a standard triangle with vertices $(-1,-1)$, $(1,-1)$ and $(-1,1)$ are given by

$$\Lambda_1 = \frac{1-\xi_1}{2} - \frac{1+\xi_2}{2}, \tag{3.33a}$$

$$\Lambda_2 = \frac{1+\xi_1}{2}, \tag{3.33b}$$

$$\Lambda_3 = \frac{1+\xi_2}{2}. \tag{3.33c}$$

Here, ξ_1 and ξ_2 are Cartesian coordinates. Barycentric coordinates are defined such that $(1,0,0)$ corresponds with the vertex $(-1,-1)$, $(0,1,0)$ with the vertex $(1,-1)$ and $(0,0,1)$ with $(-1,1)$.

[4]Since three coordinates are used to describe two-dimensional space, an extra condition is necessary to guarantee that every point is described uniquely. Usually, the condition $\Lambda_1 + \Lambda_2 + \Lambda_3 = 1$ is used.

An example of a P-th order SEM expansion basis on the standard triangle, called the *Dubiner basis* is given by

$$\phi_i^V = \Lambda_i, \qquad i = 1,\dots,3, \tag{3.34a}$$

$$\phi_{i,j,p}^E = \Lambda_i \Lambda_j P_p^S(\Lambda_i - \Lambda_j, \Lambda_i + \Lambda_j), \qquad i,j = 1,\dots,3,\ i \neq j,\ p = 0,\dots,P-2, \tag{3.34b}$$

$$\phi_{p,q}^B = \Lambda_1\Lambda_2\Lambda_3 P_p^S(\Lambda_1 - \Lambda_2, \Lambda_1 + \Lambda_2) P_q^{0,2p+1}(2\Lambda_3 - 1), \qquad p+q \leq P-3. \tag{3.34c}$$

Here $P_p^S : (x,y) \mapsto P_p(x/y)y^p$ is the *scaled Legendre polynomial*. The basis functions are subdivided into *vertex modes* which are nonzero on triangle vertices, *edge modes* which are nonzero on edges but zero on vertices, and *bubble modes* which are zero on the entire triangle boundary. This subdivision is necessary for the global assembly process: to enforce continuity, the vertex modes at any vertex in the mesh must be combined, and likewise for the edge modes at any edge in the mesh. Similarly to the one-dimensional case, the bubble modes can be restricted to their elements without creating discontinuities. The Dubiner basis (3.34) is the basis used by the Python package `ngsolve` (Schöberl, 2014), which is used for our SEM implementation. An illustration of some of these basis functions on a triangular mesh of a rectangular domain is given in Figure 3.3.

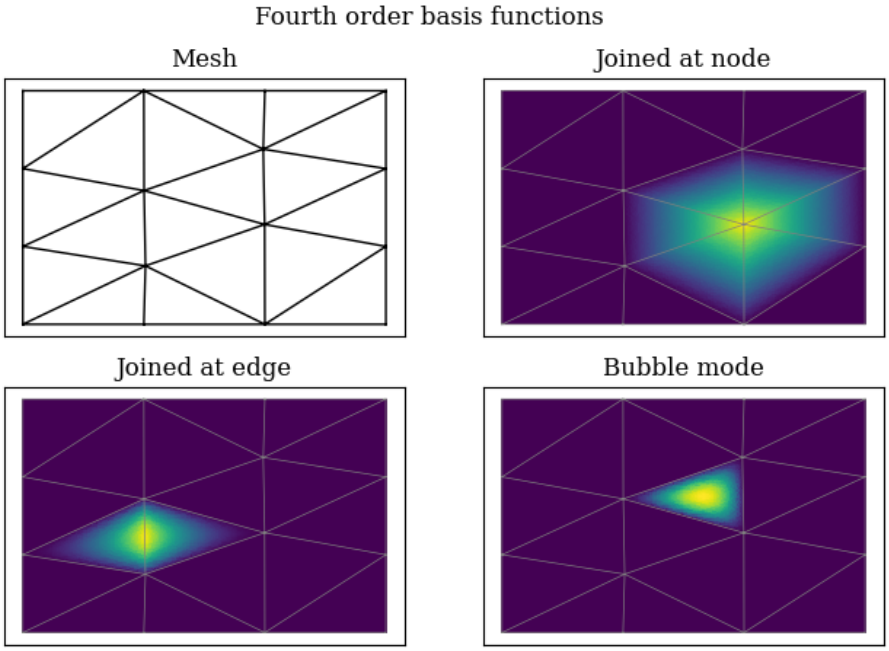

Figure 3.3: Three basis functions of a fourth order Dubiner basis on a mesh of the unit square. *Top right*: vertex modes joined at a vertex. *Bottom left*: edge modes joined at an edge. *Bottom right*: bubble mode restricted to its element.

3.3.2. Solving weak forms of PDEs: the Galerkin method

To find an approximate solution to (the weak forms of) the differential equations, the solution is written as a linear combination of the SEM basis functions with unknown coefficients. Furthermore, since the solution is approximated on a finite-dimensional space spanned by the expansion basis, it is reasonable to assume that the test functions live in this space as well (van Kan et al., 2005). Because the weak forms hold for *every* test function in the test space which is now finite-dimensional, it is natural to enforce that the weak forms hold for every basis function as test function, since each possible test function in the finite-dimensional solution space is a linear combination of the basis functions.

For example, to solve the linear weak form

$$\int_\Omega L(u)\phi \,\mathrm{d}A = \int_\Omega f\phi \,\mathrm{d}A,$$

for some linear operator L, one would write $u = \sum_{i=1}^{N} a_i \phi_i$ and choose test functions ϕ_j, $j = 1, \ldots, N$. This results in the linear system of algebraic equations

$$\sum_{i=1}^{N} a_i \int_\Omega L(\phi_i)\phi_j \, \mathrm{d}A = \int_\Omega f\phi_j \, \mathrm{d}A, \qquad j = 1, \ldots, N, \tag{3.35}$$

from which the unknown $(a_i)_{i=1}^N$ may be obtained using any linear solver of choice. This method of obtaining approximate solutions to weak formulations is called the *Galerkin method*. In principle, this is the same as the Galerkin projection described in Section 3.2. By definition of the SEM expansion basis, many pairs of basis functions are disjointly supported or (nearly) orthogonal, which makes (3.35) a relatively sparse system of equations.

For simplicity, a direct linear solver based on Gaussian elimination is used. The package `ngsolve` contains two built-in (unsymmetric) sparse direct solvers: UMFPACK (Davis & Duff, 1997) and PARDISO (Schenk & Gärtner, 2004). It was found that applied to the model of this thesis, PARDISO is generally fast and leads to solutions with relatively large residuals, whereas UMFPACK is generally slower but gives more accurate solutions. In this thesis, both of them are applied, depending on which property is necessary for the computation of interest.

3.4. Newton's method for non-linear partial differential equations

Applying the spectral element method to the weak formulations (3.29) and (3.30) will lead to a large system of non-linear algebraic equations. The *Newton-Raphson* method, or *Newton's method* can provide solutions to these equations. Given an initial guess $\mathbf{u}^0$ for the solution of a non-linear equation $F(\mathbf{u}) = \mathbf{0}$ with $F : \mathbb{R}^d \to \mathbb{R}^d$, a solution can be obtained via the iterative process

$$J(\mathbf{u}^k)(\mathbf{u}^{k+1} - \mathbf{u}^k) = -F(\mathbf{u}^k). \tag{3.36}$$

Here, J is the Jacobian matrix of the non-linear function F. If $J(\mathbf{u})$ is non-singular at the actual solution $\mathbf{u}$ and the initial guess $\mathbf{u}^0$ is 'close enough' to $\mathbf{u}$, then the Newton method converges quadratically. What 'close enough' means differs per situation.

Because it is hard to gain access to the non-linear algebraic equations in the Python package `ngsolve` that is used for the spectral element code, The Newton method is approached from a slightly different angle, though Subsection 3.4.1 will show that the resulting methods are equivalent after discretisation.

First, the *Fréchet derivative* of a non-linear operator acting between normed vector spaces must be introduced. If $\mathscr{T} : V \to W$ is a non-linear operator, then $\mathscr{T}$ is said to be *Fréchet differentiable* if for every $u \in V$, there is a bounded linear operator $D\mathscr{T}(u)$ such that

$$\lim_{\|h\|_V \to 0} \frac{\|\mathscr{T}(u+h) - \mathscr{T}(u) - D\mathscr{T}(u)h\|_W}{\|h\|_V} = 0. \tag{3.37}$$

Here, $\|h\|_V \to 0$ indicates that the $h \in V$ may approach 0 from *any* direction. In this case, $D\mathscr{T}(u)$ is called the *Fréchet derivative* of $\mathscr{T}$ at u. A related concept is the *Gateaux derivative* of $\mathscr{T}$ in the direction of a given vector $v \in U$. $\mathscr{T}$ is *Gâteaux differentiable* at $u \in U$ in the direction of $v \in V$ if the limit

$$D\mathscr{T}(u; v) = \lim_{\varepsilon \to 0} \frac{\mathscr{T}(u + \varepsilon v) - \mathscr{T}(u)}{\varepsilon} = \frac{\mathrm{d}}{\mathrm{d}\varepsilon} \mathscr{T}(u + \varepsilon v)\bigg|_{\varepsilon = 0} \tag{3.38}$$

exists in W. If $\mathscr{T}$ is Fréchet differentiable, then it is also Gâteaux differentiable in every direction and its Fréchet derivative at $u \in V$ is given by $D\mathscr{T}(u) : v \mapsto D\mathscr{T}(u; v)$ (Kesavan, 2004).

Using these functional derivatives, a Newton method for non-linear equations on general Banach spaces can be defined in an analogous way to (3.36). To solve the non-linear equation $\mathscr{T}(u) = 0$, with $\mathscr{T} : V \to W$ a non-linear operator, the iterative process

$$D\mathscr{T}(u^k)(u^{k+1} - u^k) = -\mathscr{T}(u^k) \tag{3.39}$$

can be used to find a solution, provided the initial guess u^0 is close enough to the solution. Here, the meaning of 'close enough' depends on the equations considered.

To apply the general Banach space analogue of the Newton method (3.39), the weak forms of the momentum equations (3.29) and (3.30) must be linearised. Since each momentum equation is a vector-valued operator, the Fréchet derivatives will be as well. As an illustration, one of the non-linear terms in (3.29), namely $\mathcal{T}_{ijmnk\ell}(\boldsymbol{\alpha}) := \int_{D_{2\mathrm{D}}} H\alpha_{mi}\boldsymbol{\alpha}_{nj}\cdot\nabla\phi^2_{\ell,k}\,\mathrm{d}A$ is linearised. Assuming that all $\boldsymbol{\alpha}_{mi}$ are almost everywhere continuously differentiable, the Leibniz integration rule implies that the Gâteaux derivative of $\mathcal{T}_{ijmnk\ell}$ at $\boldsymbol{\alpha}^0$ in the direction of $\tilde{\boldsymbol{\alpha}}$ is given by

$$\begin{aligned} D\mathcal{T}_{ijmnk\ell}(\boldsymbol{\alpha}^0;\tilde{\boldsymbol{\alpha}}) &= \frac{\mathrm{d}}{\mathrm{d}\varepsilon}\left(\int_{D_{2\mathrm{D}}} H(\alpha^0_{mi}+\varepsilon\tilde{\alpha}_{mi})(\boldsymbol{\alpha}^0_{nj}+\varepsilon\tilde{\boldsymbol{\alpha}}_{nj})\cdot\nabla\phi^2_{\ell,k}\,\mathrm{d}A\right)\Big|_{\varepsilon=0} \\ &= \int_{D_{2\mathrm{D}}} H\,\frac{\mathrm{d}}{\mathrm{d}\varepsilon}\left(\alpha^0_{mi}\boldsymbol{\alpha}^0_{nj}+\varepsilon\tilde{\alpha}_{mi}\boldsymbol{\alpha}^0_{nj}+\varepsilon\alpha^0_{mi}\tilde{\boldsymbol{\alpha}}_{nj}+\varepsilon^2\tilde{\alpha}_{mi}\tilde{\boldsymbol{\alpha}}_{nj}\right)\Big|_{\varepsilon=0}\cdot\nabla\phi^2_{\ell,k}\,\mathrm{d}A \\ &= \int_{D_{2\mathrm{D}}} H(\alpha^0_{mi}\tilde{\boldsymbol{\alpha}}_{nj}+\tilde{\alpha}_{mi}\boldsymbol{\alpha}^0_{nj})\cdot\nabla\phi^2_{\ell,k}\,\mathrm{d}A. \end{aligned} \tag{3.40}$$

The other two types of non-linear terms can be linearised in exactly the same manner. They are given by

$$\int_{D_{2\mathrm{D}}} H\phi^2_{\ell,k}\nabla\alpha_{mi}\cdot\boldsymbol{\alpha}_{nj}\,\mathrm{d}A \xrightarrow{D} \int_{D_{2\mathrm{D}}} H\phi^2_{\ell,k}\nabla\tilde{\alpha}_{mi}\cdot\boldsymbol{\alpha}^0_{nj}\,\mathrm{d}A+\int_{D_{2\mathrm{D}}} H\phi^2_{\ell,k}\nabla\alpha^0_{mi}\cdot\tilde{\boldsymbol{\alpha}}_{nj}\,\mathrm{d}A, \tag{3.41a}$$

$$\int_{\Gamma_s} H\phi^2_{\ell,k}\alpha_{mi}\boldsymbol{\alpha}_{nj}\cdot\mathbf{n}\,\mathrm{d}s \xrightarrow{D} \int_{\Gamma_s} H\phi^2_{\ell,k}\tilde{\alpha}_{mi}\boldsymbol{\alpha}^0_{nj}\cdot\mathbf{n}\,\mathrm{d}s+\int_{\Gamma_s} H\phi^2_{\ell,k}\alpha^0_{mi}\tilde{\boldsymbol{\alpha}}_{nj}\cdot\mathbf{n}\,\mathrm{d}s. \tag{3.41b}$$

Here $\xrightarrow{D}$ denotes taking the Gâteaux derivative at $\boldsymbol{\alpha}^0$ in the direction of $\tilde{\boldsymbol{\alpha}}$.

3.4.1. Order of linearisation

In this final subsection, it is proved that the final linear systems of algebraic equations that result from the Newton methods (3.36) and (3.39) are equal as long as the initial guess u^0 in (3.39) can be represented exactly by the SEM basis. For notational brevity, the result is proved for weak forms that can be written like

$$\int_\Omega F(u,u_x,u_y,x,y)\phi(x.y)\,\mathrm{d}A=0,$$

i.e. 'systems' of only a single PDE. However, the proof extends to systems of PDEs as well.

Proposition 3.1. *Let $\Omega\subseteq\mathbb{R}^2$ be a bounded and open set, let $F:\mathbb{R}^5\to\mathbb{R}$ be continuously differentiable and let the SEM basis $(\phi_i)_{i=1}^N$ for $N\in\mathbb{N}$ be bounded and continuously differentiable almost everywhere in Ω. For a given test function ϕ, define the operator $\mathcal{T}_\phi : C^1(\overline{\Omega})\to C^1(\overline{\Omega})$ by*

$$\mathcal{T}_\phi(u)=\int_\Omega F(u,u_x,u_y,x,y)\phi(x,y)\,\mathrm{d}A.$$

If the initial guess u^0 in (3.39) can be represented exactly by $(\phi_i)_{i=1}^N$, then the two Newton methods (3.39) and (3.36) for the weak form $\forall\phi: T_\phi(u)=0$ lead to exactly the same system of algebraic equations for any given iteration.

Proof. First, note that $C^1(\overline{\Omega})$ is a normed vector space (even a Banach space) in the norm $\|\cdot\|_{C^1(\overline{\Omega})}$ given by

$$\|f\|_{C^1(\overline{\Omega})} := \max\{\|f\|_\infty,\|f_x\|_\infty,\|f_y\|_\infty\},$$

(van Neerven, 2022, pg. 77). Thus, taking Gâteaux and Fréchet derivatives of T is justified. Now, for $v\in C^1(\overline{\Omega})$, by linearity of differentiation, one has that

$$\begin{aligned} D\mathcal{T}_\phi(u;v) &= \frac{\mathrm{d}}{\mathrm{d}\varepsilon}\left(\int_\Omega F(u+\varepsilon v,u_x+\varepsilon v_x,u_y+\varepsilon v_y,x,y)\phi\,\mathrm{d}A\right)\Big|_{\varepsilon=0} \\ \text{(Leibniz rule)} &= \int_\Omega \frac{\mathrm{d}}{\mathrm{d}\varepsilon}F(u+\varepsilon v,u_x+\varepsilon v_x,u_y+\varepsilon v_y,x,y)\Big|_{\varepsilon=0}\phi\,\mathrm{d}A \\ \text{(Chain rule)} &= \int_\Omega\left(v\frac{\partial F}{\partial\xi_1}(u,u_x,u_y,x,y)+v_x\frac{\partial F}{\partial\xi_2}(u,u_x,u_y,x,y)+v_y\frac{\partial F}{\partial\xi_3}(u,u_x,u_y,x,y)\right)\phi\,\mathrm{d}A. \end{aligned}$$

Here $\frac{\partial F}{\partial \xi_k}$ denotes the partial derivative of F with respect to its k-th variable. Using the Leibniz rule is justified by the fact that F, u, v and ϕ are bounded and continuously differentiable almost everywhere.

The continuous Newton method (3.39) for the weak form $\forall \phi : T_\phi(u) = 0$ can now be discretised using the Galerkin method to obtain the linear system

$$\sum_{i=1}^{N} b_i^k \left(\int_\Omega \frac{\partial F}{\partial \xi_1}(u^k, u_x^k, u_y^k, x, y)\phi_i\phi_j \,\mathrm{d}A + \int_\Omega \frac{\partial F}{\partial \xi_2}(u^k, u_x^k, u_y^k, x, y)\frac{\partial \phi_i}{\partial x}\phi_j \,\mathrm{d}A \right.$$
$$\left. + \frac{\partial F}{\partial \xi_3}(u^k, u_x^k, u_y^k, x, y)\frac{\partial \phi_i}{\partial y}\phi_j \,\mathrm{d}A \right) = -\int_\Omega F(u^k, u_x^k, u_y^k, x, y)\phi_j \,\mathrm{d}A,$$

for $j = 1, \ldots, N$. The coefficients b_i^k can then be used to construct $u^{k+1} - u^k$, by means of $u^{k+1} - u^k = \sum_{i=1}^N b_i^k \phi_i$. Note that if u^0 can be written as $\sum_{i=1}^N a_i^0 \phi_i$, then all subsequent u^k can be written as $\sum_{i=1}^N a_i^k \phi_i$.

Now, the algebraic version of the Newton method (3.36) is applied. To this end, the weak form $\forall \phi : \mathcal{T}_\phi(u) = 0$ is discretised using the Galerkin method, which results in a non-linear system of algebraic equations:

$$\int_\Omega F\left(\sum_{i=1}^N a_i\phi_i, \sum_{i=1}^N a_i \frac{\partial \phi_i}{\partial x}, \sum_{i=1}^N a_i \frac{\partial \phi_i}{\partial y}, x, y \right)\phi_j \,\mathrm{d}A = 0, \qquad j = 1, \ldots, N,$$
$$\Leftrightarrow T_{\text{disc}}(a_1, \ldots, a_N) = 0.$$

To apply (3.36), the Jacobian of T_{disc} must be computed:

$$\begin{aligned}
\frac{\partial}{\partial a_i}\left(T_{\text{disc}}(a_1, \ldots, a_N)\right)_j &= \frac{\partial}{\partial a_i}\left(\int_\Omega F\left(\sum_{i=1}^N a_i\phi_i, \sum_{i=1}^N a_i \frac{\partial \phi_i}{\partial x}, \sum_{i=1}^N a_i \frac{\partial \phi_i}{\partial y}, x, y \right)\phi_j \,\mathrm{d}A \right) \\
\text{(Leibniz rule)} &= \int_\Omega \frac{\partial F}{\partial a_i}\left(\sum_{i=1}^N a_i\phi_i, \sum_{i=1}^N a_i \frac{\partial \phi_i}{\partial x}, \sum_{i=1}^N a_i \frac{\partial \phi_i}{\partial y}, x, y \right)\phi_j \,\mathrm{d}A \\
\text{(Chain rule)} &= \int_\Omega \frac{\partial F}{\partial \xi_1}\left(\sum_{i=1}^N a_i\phi_i, \sum_{i=1}^N a_i \frac{\partial \phi_i}{\partial x}, \sum_{i=1}^N a_i \frac{\partial \phi_i}{\partial y}, x, y \right)\phi_i\phi_j \,\mathrm{d}A \\
&\quad + \int_\Omega \frac{\partial F}{\partial \xi_2}\left(\sum_{i=1}^N a_i\phi_i, \sum_{i=1}^N a_i \frac{\partial \phi_i}{\partial x}, \sum_{i=1}^N a_i \frac{\partial \phi_i}{\partial y}, x, y \right)\frac{\partial \phi_i}{\partial x}\phi_j \,\mathrm{d}A \\
&\quad + \int_\Omega \frac{\partial F}{\partial \xi_3}\left(\sum_{i=1}^N a_i\phi_i, \sum_{i=1}^N a_i \frac{\partial \phi_i}{\partial x}, \sum_{i=1}^N a_i \frac{\partial \phi_i}{\partial y}, x, y \right)\frac{\partial \phi_i}{\partial y}\phi_j \,\mathrm{d}A.
\end{aligned}$$

Then the linear system that must be solved in iteration k is given by

$$\begin{aligned}
&\sum_{i=1}^N b_i^k \left[\int_\Omega \frac{\partial F}{\partial \xi_1}\left(\sum_{i=1}^N a_i^k\phi_i, \sum_{i=1}^N a_i^k \frac{\partial \phi_i}{\partial x}, \sum_{i=1}^N a_i^k \frac{\partial \phi_i}{\partial y}, x, y \right)\phi_i\phi_j \,\mathrm{d}A \right. \\
&\quad + \int_\Omega \frac{\partial F}{\partial \xi_2}\left(\sum_{i=1}^N a_i^k\phi_i, \sum_{i=1}^N a_i^k \frac{\partial \phi_i}{\partial x}, \sum_{i=1}^N a_i^k \frac{\partial \phi_i}{\partial y}, x, y \right)\frac{\partial \phi_i}{\partial x}\phi_j \,\mathrm{d}A \\
&\quad \left. + \int_\Omega \frac{\partial F}{\partial \xi_3}\left(\sum_{i=1}^N a_i^k\phi_i, \sum_{i=1}^N a_i^k \frac{\partial \phi_i}{\partial x}, \sum_{i=1}^N a_i^k \frac{\partial \phi_i}{\partial y}, x, y \right)\frac{\partial \phi_i}{\partial y}\phi_j \,\mathrm{d}A \right] \\
&\quad = -\int_\Omega F\left(\sum_{i=1}^N a_i^k\phi_i, \sum_{i=1}^N a_i^k \frac{\partial \phi_i}{\partial x}, \sum_{i=1}^N a_i^k \frac{\partial \phi_i}{\partial y}, x, y \right)\phi_j \,\mathrm{d}A,
\end{aligned}$$

for $j = 1, \ldots, N$, and where b_i^k are defined in the same way as before. If every u^k can be represented exactly using the basis functions, then the linear systems resulting from (3.39) and (3.36) are exactly equal. As noted before, this is the case when the initial guess satisfies this requirement. □

4

Results

In this chapter, the results are presented. In Section 4.1, I present the default choice of domain and bathymetry, and values of physical and numerical parameters. Section 4.2 discusses the semidiurnal tidal motion (M_2) without advection. Subsequently, Section 4.3 describes the structure of the residual flow induced by advection. In each section, the solutions for a relatively flat bathymetry and a steeper one are compared, and the effects of steepness of the bathymetry are quantified by means of scalar values that characterise aspects of the solutions.

4.1. Parameter values

For simplicity, the two-dimensional domain $D_{2\mathrm{D}}$ is chosen to be rectangular, with width B and length L: $D_{2\mathrm{D}} = [0, L] \times [-B/2, B/2]$. The length L is chosen just small enough to be able to use sufficiently fine meshes and/or high SEM basis orders to obtain numerically converged results on ordinary computers.

The model is forced at the seaward boundary ($x = 0$) by a uniform semidiurnal (M_2) tidal water level $\zeta(x, y, t) = A_{M_2} \cos(2\pi\sigma t)$ with zero phase.

Table 4.1 contains default values of all physical and numerical parameters. In this table, p is the order of the SEM basis and Δx is the mesh size. For triangular meshes, Δx is the length scale of the largest elements in the mesh. If multiscale geometries are used, elements can differ in size by quite a lot, but for rectangular domains, the parameter Δx is a good indication for the size of *all* elements.

4.1.1. Bathymetries with variable steepness

The bathymetry has a Gaussian shape independent of the along-channel coordinate x, and is given by

$$H(x, y) = H_{\mathrm{offset}} + H_{\mathrm{scale}} \mathrm{e}^{-C\eta^2}. \tag{4.1}$$

Here, H_{offset} and H_{scale} control the offset and scale of the Gaussian profile, and C, the *steepness parameter*, controls the steepness of the profile. The coordinate η is given by $\eta = 2y/B$, such that it runs from -1 to 1.

To study the effect of bathymetric steepness, the steepness parameter C is varies. The other parameters H_{offset} and H_{scale} are chosen in such a way, that the cross-sectional area remains constant if C is varied. Ensing et al. (2015) tune H_{offset} and H_{scale} such that the water depth at the closed boundaries remains constant. However, this restriction excludes flat beds, since the cross-sectional area of an estuary with a flat bed cannot be equal to the cross-sectional area of an estuary with depth strictly larger than the depth at the closed boundaries. Instead, the offset parameter H_{offset} is used to preserve cross-sectional area under varying C. The parameter H_{scale} is kept constant. Using some integral identities and elementary algebra, it is found that H_{offset} should be equal to

$$H_{\mathrm{offset}} = \frac{H_{\mathrm{scale}}}{2} \left(\sqrt{\frac{\pi}{6}} \operatorname{erf}\left(\sqrt{6}\right) - \sqrt{\frac{\pi}{C}} \operatorname{erf}\left(\sqrt{C}\right) \right) + 2, \tag{4.2}$$

Physical parameters	
g	$9.81\ \mathrm{ms}^{-2}$
f	$10^{-4}\ \mathrm{rad\,s}^{-1}$
$\mathscr{A}_v$	$0.01\ \mathrm{m}^2\mathrm{s}^{-1}$
σ	$2.236 \cdot 10^{-5}\ \mathrm{s}^{-1}$
ρ_0	$1020\ \mathrm{kg\,m}^{-3}$
A_{M_2}	1 m
Shape parameters	
L	10 km
B	3 km
H_{offset}	2 m
H_{scale}	10 m
C	6
Numerical parameters	
M	7
$i_{\max}$	2
p	4
Δx	1 km
K (explained in Subsection 4.1.2)	1.2

Table 4.1: Default values of numerical and physical parameters

where erf denotes the error function. The range of bathymetries available by varying C is illustrated in Figure 4.1.

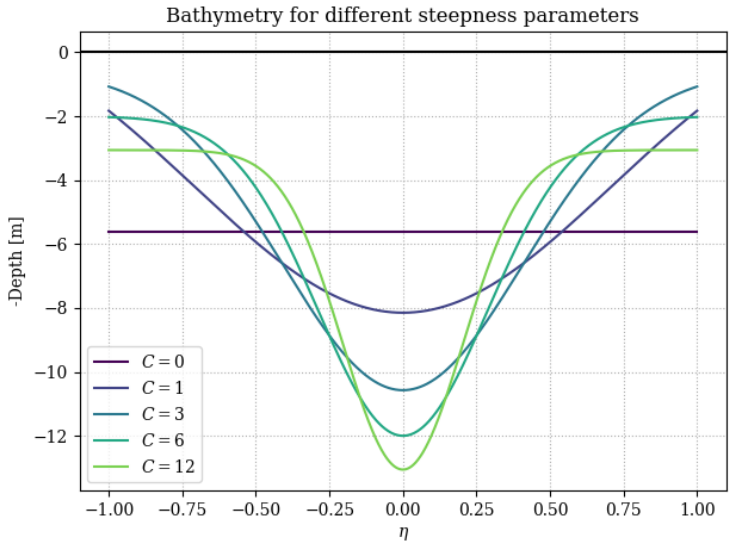

Figure 4.1: Bathymetries given by (4.1) for different steepness parameters ($C = 0, 1, 3, 6$ and 12).

4.1.2. Local mesh refinement

Steep and narrow channels corresponding to large steepness parameters introduce small length scales in the domain, which leads to small length scales in the solution. To capture this behaviour accurately, either high order basis functions or small mesh sizes are necessary. However, these small mesh sizes or high-order basis functions are really only required over those locations where the small-scale behaviour is located. *Local mesh refinement* allows us to decrease the mesh size exactly in those places where it is required, increasing the efficiency of the solution method. Local p-refinement, which increases the order of the local SEM basis

where more accuracy is required, is also a possibility, but this is more difficult to implement in `ngsolve`.

First, a computational mesh is generated using the standard algorithm of `ngsolve`. Then, we loop over every triangular element in the mesh and mark them based on some refinement rule. Finally, the marked elements are refined, which involves bisecting the element along one of its medians. To ensure that the new element vertices do not border the edges of neighbouring elements, the mesh refinement modifies the neighbouring elements as well. This step is necessary to preserve the classification of vertex, edge and bubble modes in the SEM basis.

Elements are marked based on the rule:

$$\int_e \|\nabla H\| \, \mathrm{d}A \geq \frac{K}{|E|} \sum_{e \in E} \int_e \|\nabla H\| \, \mathrm{d}A, \tag{4.3}$$

where $\|\cdot\|$ is the Euclidean norm in $\mathbb{R}^2$, E is the set of all elements, $K > 1$ is a parameter controlling how sensitive the rule is. In words, (4.3) marks elements if the bathymetry gradient in that element exceeds the average bathymetry by a factor of K: if an element is located over sufficiently steep bathymetry, it will be marked. Figure 4.2 illustrates mesh refinement using rule (4.3) applied to the default bathymetry ($C = 6$).

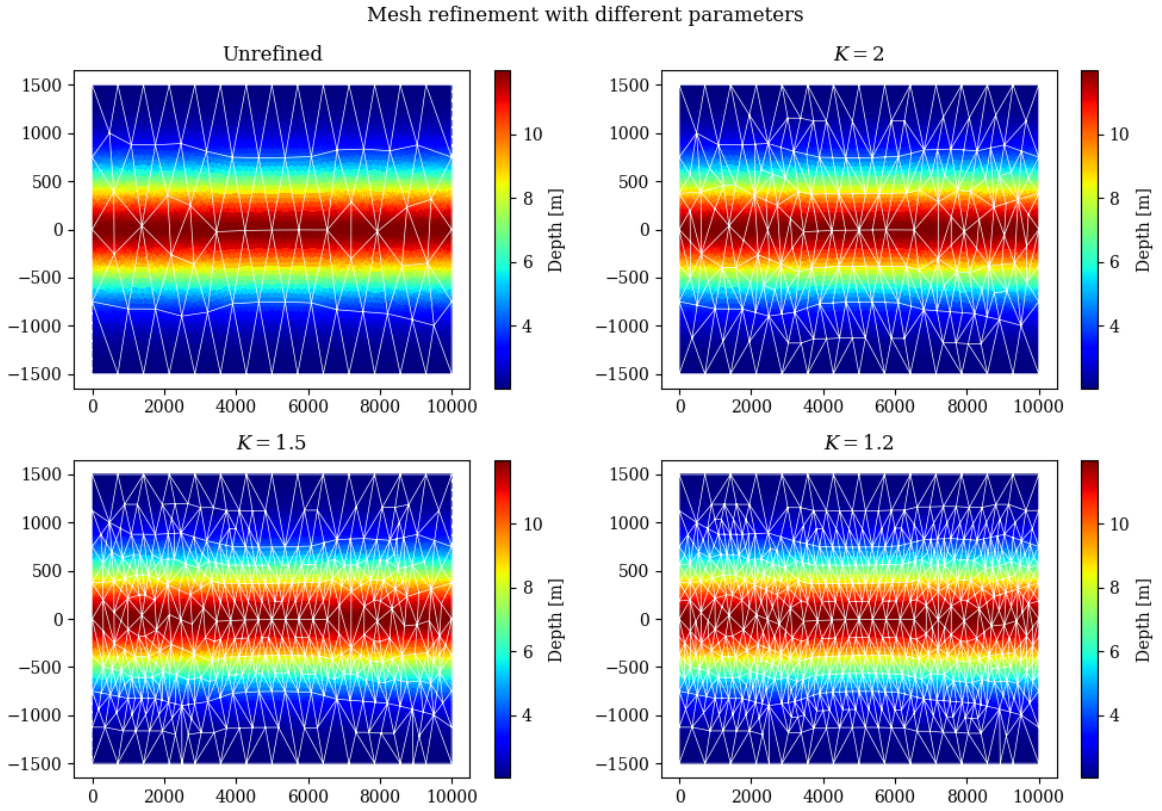

Figure 4.2: Refinement of a mesh generated with $\Delta x = 700$ m based on rule (4.3), applied to the default bathymetry ($C = 6$). The white wireframes denote the edges of the meshes, and the colour indicates the local water depth.

By default, K is set to 1.2 and the mesh is subjected to two iterations of local mesh refinement. These values were based on trial and error; using two iterations with $K = 1.2$ leaded to numerically converged results that were able to be computed on an ordinary computer.

4.2. Semidiurnal tidal flow

First, the principal semidiurnal tidal flow (M_2) and its dependence on the bathymetric steepness parameter C is investigated. For this purpose, the non-linear advective terms are neglected ($\varepsilon = 0$). This has two main reasons. Firstly, understanding the linear tidal motion is beneficial for understanding the full tidal motion.

Indeed, Ianniello (1979) has shown that under certain scaling assumptions, the linear M_2-flow constitutes the dominant part of the hydrodynamics. Secondly, the Newton method failed to converge if advective effects were included. As of yet, it is unclear why the method diverges in this case. Subsection 4.3.1 elaborates on this.

The effect of steep bathymetries on the linear M_2-flow is investigated both qualitatively (Subsection 4.2.1) and quantitatively (Subsection 4.2.2). The solutions for a gently sloping bathymetry ($C = 0.1$)[1] are first compared to those of a steeper bathymetry ($C = 6$). To describe the effects of steepness quantitatively, we capture the hydrodynamics using a small set of scalars and plot those scalars against the steepness parameter.

For the following analysis, it is useful to describe the time-dependent solutions as complex waves, like:

$$u(x,y,z,t) = U_{\text{real}}(x,y,z)h_1(t) + iU_{\text{imag}}(x,y,z)h_{-1}(t) = |U(x,y,z)|\exp(i\varphi(x,y,z)),$$

for the M_2-along-channel velocity. With this formulation, the tidal flow can be described using amplitudes and phases relative to the phase of the tidal water level forcing at $x = 0$. Importantly, positive phases are perceived as *delays* with respect to the tidal forcing, and negative phases indicate that the solution is ahead of the forcing.

4.2.1. Comparison of two solutions

Water surface amplitude

In Figures 4.3-4.5, the amplitude of the M_2 water surface elevation corresponding to $C = 0.1$ and $C = 6$ and their difference is shown. By linearity, other tidal constituents than M_2 are identically equal to zero.

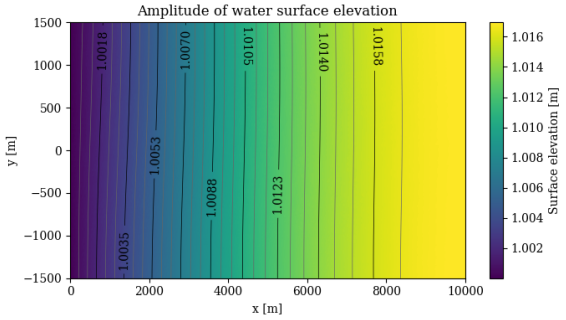

Figure 4.3: Top view of the amplitude of the M_2-water surface elevation corresponding to $C = 0.1$. Lighter (darker) colours indicate larger (smaller) amplitudes.

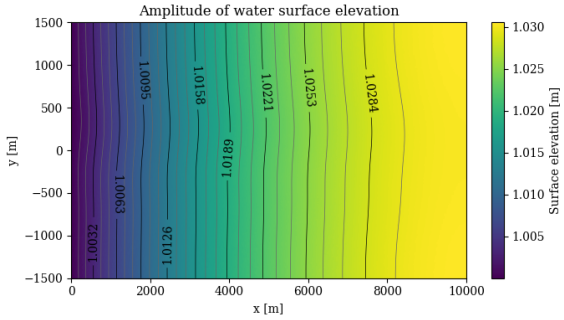

Figure 4.4: Top view of the amplitude of the M_2-water surface elevation corresponding to $C = 6$. Lighter (darker) colours indicate larger (smaller) amplitudes.

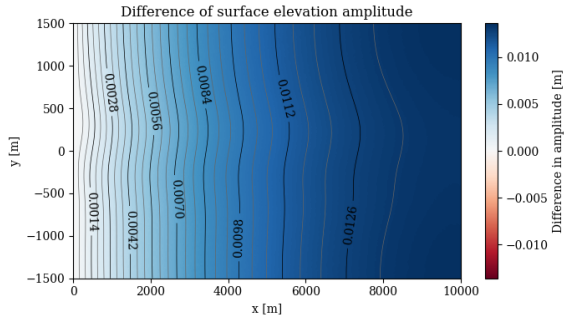

Figure 4.5: Top view of difference between M_2-water surface elevation amplitudes corresponding to $C = 0.1$ and $C = 6$. Blue indicates that the amplitude corresponding to $C = 6$ is larger than the one corresponding to $C = 0.1$, and red indicates the opposite. Darker (lighter) colours signify larger (smaller) differences

[1] In the case $C = 0$ (flat bed), Coriolis effects are dominant. It is better to use $C = 0.1$, because the effects of steepness become more noticable this way.

The plots indicate that the water surface elevation is not overly affected by the steepness of the bathymetry, since both cases are very similar (as shown in Figure 4.5), though the steeper bathymetry seems to lead to larger amplitudes. In both cases, variations in the amplitude of the surface elevation never exceed three centimeters. The phase varies even less (shown later in Figures 4.14 and 4.15). Thus, the water surface elevation behaves like a spatially uniform surface moving up and down in phase with the tidal forcing, regardless of the steepness.

These observations are consistent with the literature. Linear wave theory indicates that tidal waves have wavelengths of approximately $\sigma^{-1}\sqrt{gH}$ (Bosboom & Stive, 2023, Appendix A). Estuaries are typically around 10-20 metres deep (Nitsche et al., 2007; Van Damme et al., 2005). It follows that the tidal wave is hundreds of kilometers long. Therefore, the surface will vary but little in the short range of 10 km. Furthermore, Winant (2007) showed that the lateral surface variation ζ_y is of order $\mathcal{O}(B/L)$. Since the length L is larger than the width B, the small lateral variations shown in Figures 4.3 and 4.4 are consistent with his results.

Along-channel velocity amplitude

In Figures 4.6 and 4.7, maps of the amplitude of the along-channel velocity u are shown. From these figures, it becomes clear that varying the steepness parameter significantly affects the flow velocities.

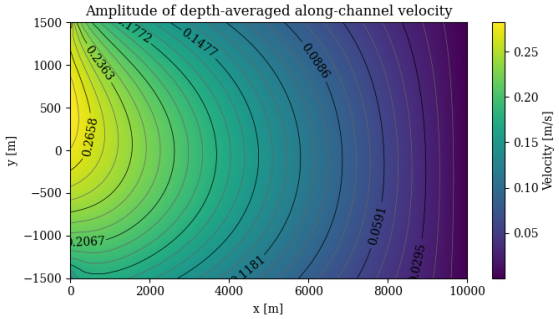

Figure 4.6: Top view of amplitude of depth-averaged M_2-along channel velocity corresponding to $C = 0.1$. Lighter (darker) colours indicate larger (smaller) amplitudes.

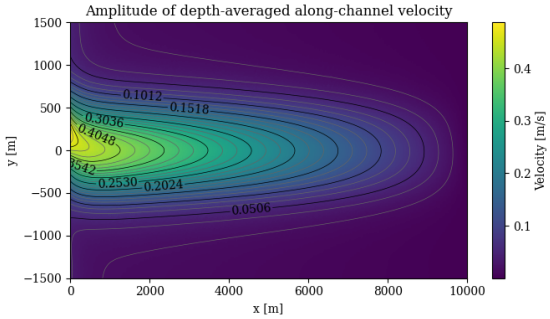

Figure 4.7: Top view of amplitude of depth-averaged M_2-along channel velocity corresponding to $C = 6$. Lighter (darker) colours indicate larger (smaller) amplitudes.

Firstly, the figures show that in both cases, the contour lines of the velocity curve upwards close to the seaward boundary. This is the effect of an unphysical boundary layer, and should be ignored in the analysis. Indeed, Winant (2007) demonstrated that in the presence of Coriolis forces and a non-flat bathymetry, it is impossible for the water surface elevation to be spatially uniform, as prescribed in (3.5d). Because the surface elevation and flow velocities are coupled, the flow velocities are unphysical close to the boundary as well. The cross-channel velocity is also affected by this boundary layer.

Secondly, the flow velocity in the deeper channel is larger than the velocity closer to the banks of the river. This effect is much more pronounced when a steeper bathymetry is used. Intuitively speaking, the water experiences less friction from the bed in the deeper channel than closer to the shallower sides. A more precise explanation is as follows: in ς-coordinates, the parameter controlling the bed friction is given by $\mathscr{A}_v H^{-2}$. In deeper waters, this parameter will be much smaller than in shallow water. As a result, the boundary layer (in ς-coordinates) at the bed, caused by the no-slip condition (3.5c-d) will be smaller, and accordingly, velocities above the bed are able to grow more quickly due to the reduced influence of bed friction. Figures 4.8 and 4.9 illustrate this boundary layer by showing the along-channel velocity amplitudes in the cross-section $\{L/2\} \times [-B/2, B/2]$, i.e. halfway along the estuary.

Tidal currents

Above, only the amplitudes of the solution were discussed. Now, the velocity vector, i.e. the current, and its variation over the tidal cycle is described and explained. To this end, the amplitudes of the cross-channel velocities in the central cross-section are shown in Figures 4.10 and 4.11, and Figures 4.12 and 4.13 show the depth-integrated velocities, i.e. the transport of water in the x- and y-direction at slack tide before ebb (minimum flow velocity before flow out of the estuary), ebb (maximum flow out of the estuary), slack tide before flood (minimum flow velocity before flow into the estuary) and flood (maximum flow into the estuary), respectively. The depth-*integrated* velocities are shown instead of depth-*averaged* velocities because the

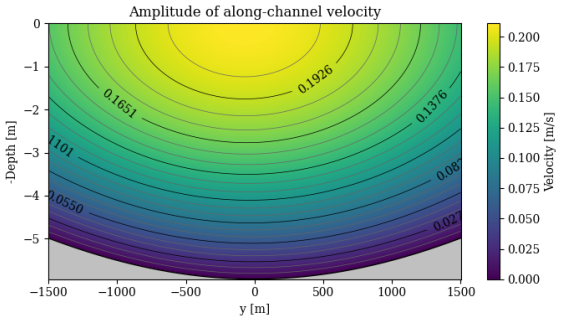

Figure 4.8: Amplitude of M_2-along-channel velocity in the cross-section $\{L/2\} \times [-B/2, B/2]$ corresponding to $C = 0.1$. Lighter (darker) colours indicate larger (smaller) velocities.

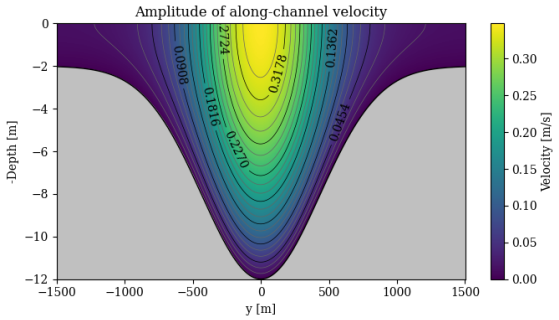

Figure 4.9: Amplitude of M_2-along-channel velocity in the cross-section $\{L/2\} \times [-B/2, B/2]$ corresponding to $C = 6$. Lighter (darker) colours indicate larger (smaller) velocities.

depth-integrated velocities are directly linked to the water surface through the depth-integrated continuity equation. This makes interpretation of the structure of the depth-integrated currents straightforward.

In case $C = 0.1$, the tidal currents are approximately laterally uniform, though they are slightly stronger in the deeper channel, as expected. In Figure 4.12, the arrows indicate that the cross-channel velocity is nowhere of the same order of magnitude as the along-channel velocities; all arrows are horizontal. This observation is supported by Figures 4.10 and 4.11. These figures also show that the cross-channel velocity is two orders of magnitude smaller than the along-channel velocity.

The flow in the steep estuary ($C = 6$) differs a lot from the nearly flat estuary ($C = 0.1$). During ebb, most of the water flows out of the estuary through the deep channel, and water on the shallow banks flows towards the channel. During flood, the exact opposite is visible: water flows in through the channel and from the channel towards the banks. As Figures 4.10 and 4.11 indicate, the lateral velocities are much larger in this case as well, and are able to balance the along-channel velocities close to the banks. The asymmetry of the lateral velocity structure shown in Figures 4.10 and 4.11 is caused by Coriolis forces.

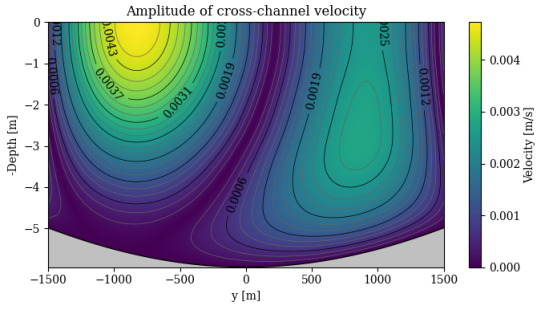

Figure 4.10: Amplitude of M_2-cross-channel velocity in the cross-section $\{L/2\} \times [-B/2, B/2]$ corresponding to $C = 0.1$. Lighter (darker) colours indicate larger (smaller) velocities.

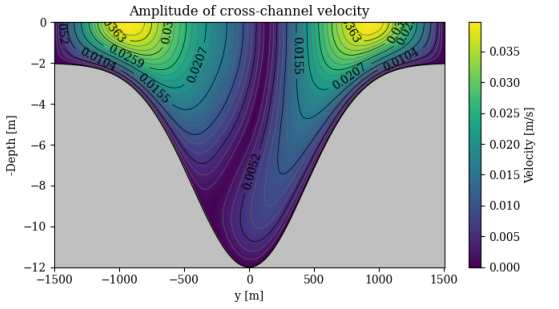

Figure 4.11: Amplitude of M_2-cross-channel velocity in the cross-section $\{L/2\} \times [-B/2, B/2]$ corresponding to $C = 6$. Lighter (darker) colours indicate larger (smaller) velocities.

These observations can be explained using the previous observations and the depth-integrated continuity equation (3.4d). The depth-integrated continuity equation and the divergence theorem imply that for any $\tilde{D} \subseteq D_{2D}$ that has a piecewise-smooth boundary,

$$\int_{\tilde{D}} \zeta_t \, \mathrm{d}A = -\oint_{\partial\tilde{D}} \left(H \int_{-1}^{0} \mathbf{u} \, \mathrm{d}\varsigma \right) \cdot \mathbf{n} \, \mathrm{d}s =: -\oint_{\partial\tilde{D}} \mathbf{U} \cdot \mathbf{n} \, \mathrm{d}s. \tag{4.4}$$

$\mathbf{U}$ is the vector of depth-integrated velocities, and $\mathbf{n}$ is the outward-pointing normal vector. In words, identity (4.4) states that the total increase of surface elevation in $\tilde{D}$ must be equal to the total amount of water flowing into $\tilde{D}$.

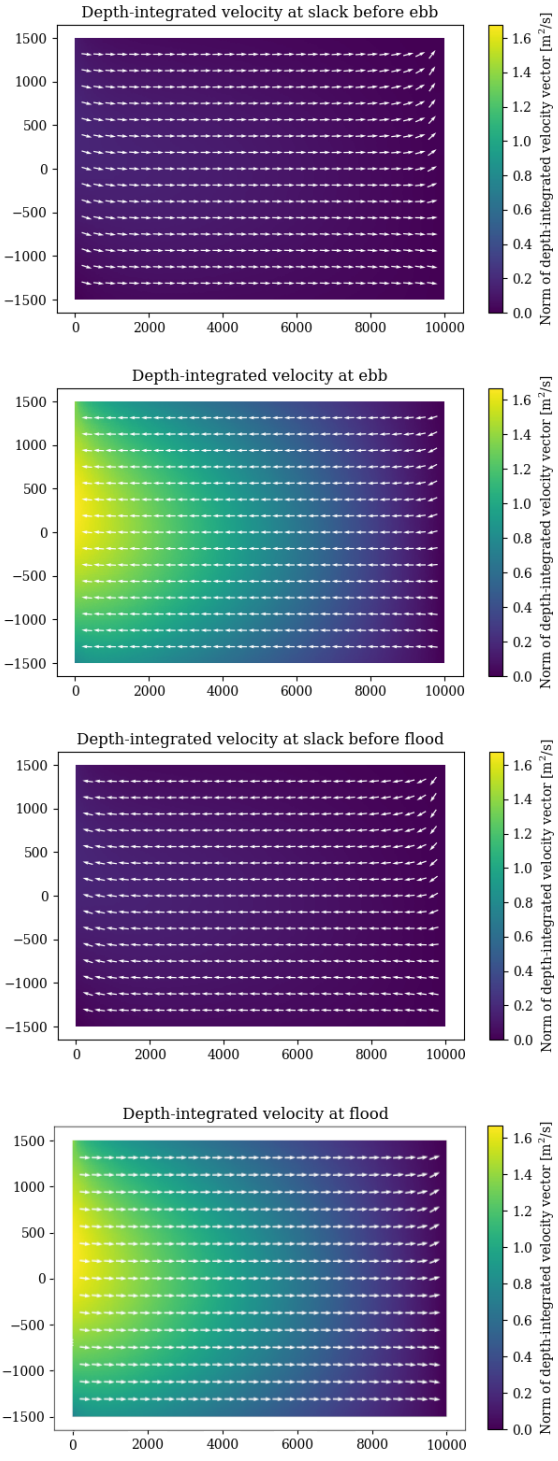

Figure 4.12: Transport of water (depth-integrated velocity) at four moments in the tidal cycle ($t = 0$, $t = 0.25\sigma^{-1}$, $t = 0.5\sigma^{-1}$ and $t = 0.75\sigma^{-1}$) corresponding to $C = 0.1$. The colour denotes the norm of the transport where lighter (darker) colours denote stronger (weaker) currents, and the arrows denote the direction.

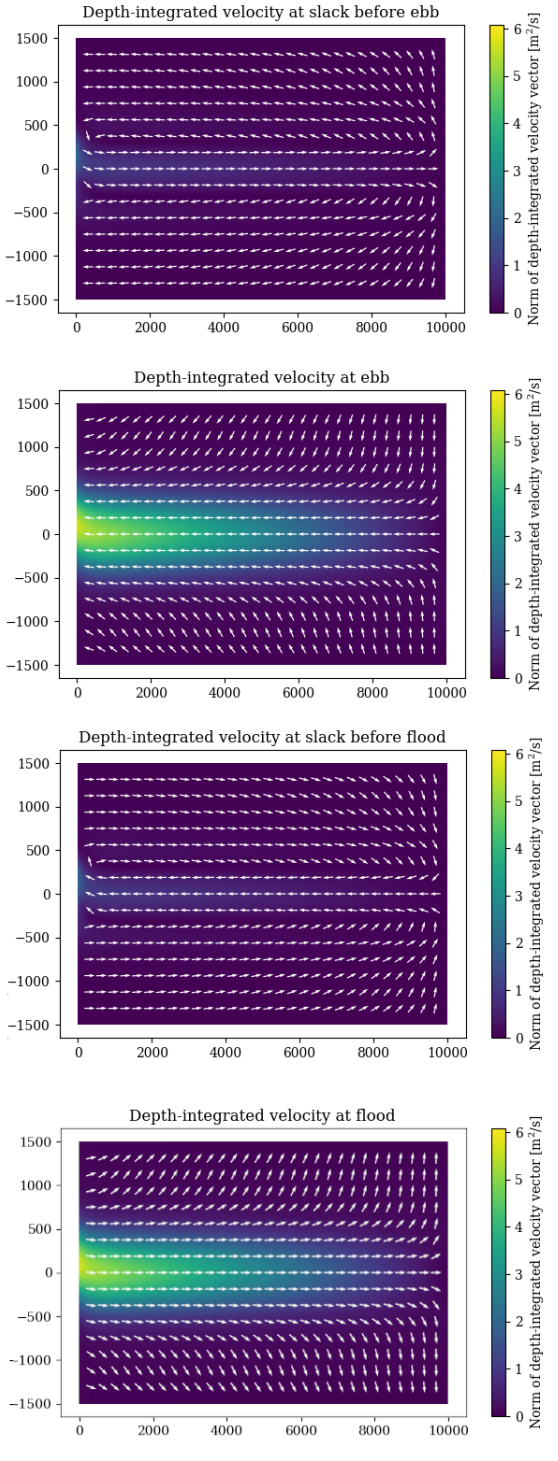

Figure 4.13: Transport of water (depth-integrated velocity) at four moments in the tidal cycle ($t = 0$, $t = 0.25\sigma^{-1}$, $t = 0.5\sigma^{-1}$ and $t = 0.75\sigma^{-1}$) corresponding to $C = 6$. The colour denotes the norm of the transport where lighter (darker) colours denote stronger (weaker) currents, and the arrows denote the direction.

First, the case $C = 6$ is analysed. During flood, water is transported into the estuary via the channel, because the along-channel velocity is large in deeper areas. Accordingly, the total amount of water flowing into any $\tilde{D}$ located in the channel is also large. However, the water surface elevation and its time derivative are ap-

proximately uniform in space. Therefore, for any $\tilde{D}$ located in shallow waters, the total flow into $\tilde{D}$ must be approximately equal to the the total flow into a $\tilde{D}$ of the same area in the deep channel. Since along-channel velocities are small in shallow waters, the lateral transport of water must be relatively large in these areas, i.e. water flows from the channel towards the banks. The same arguments can be used to explain the current during ebb and the currents in the case $C = 0.1$. In the latter case, the difference in along-channel velocity between channel and banks is much smaller, which implies that the lateral velocities will be much smaller as well.

Phase difference in the channel

In short estuaries, the water surface is typically approximately a standing wave (Friedrichs, 2010), in which the velocities are ahead of the surface by $\pi/2$ radians. This phase difference arises because water must flow into the estuary before the water surface can rise. However, the slack water currents in the steep estuary indicate that the water transport above the channel is delayed compared to the transport over shallower waters. Figures 4.14 and 4.15, in which the phases of the surface and the along-channel velocity and their differences are shown, support this observation. To be able to discern variation in the phase, the colour ranges in both these Figures differ. Furthermore, the figures indicate that in the nearly flat estuary, the phase difference between surface and velocity is indeed close to $\pi/2$, but that in the steep estuary, the phase difference between surface and velocity differs significantly from $\pi/2$.

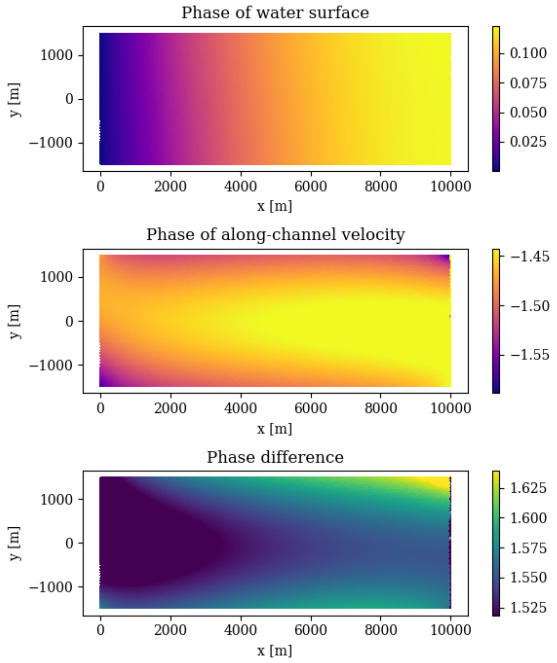

Figure 4.14: Phases [rad] of water surface elevation (top), depth-averaged along-channel velocity (middle) and their difference (bottom) in the case $C = 0.1$. Lighter (darker) colours are associated with larger (smaller) phases.

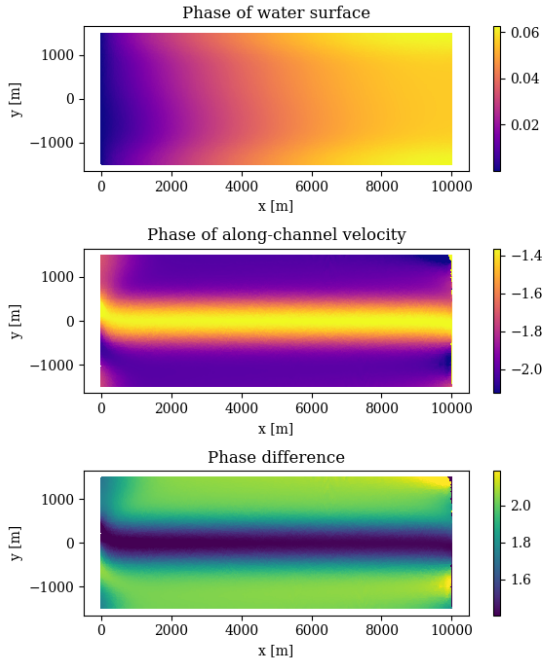

Figure 4.15: Phases [rad] of water surface elevation (top), depth-averaged along-channel velocity (middle) and their difference (bottom) in the case $C = 6$. Lighter (darker) colours are associated with larger (smaller) phases.

4.2.2. Quantifying the effects of steepness

Summarising Subsection 4.2.1, the most striking differences between the hydrodynamics in the steep and nearly flat estuaries are the growing difference between along-channel flow in the channel and close to the banks, the increasing cross-channel flow induced by this difference, and the smaller phase difference between surface and velocity above the channel. To quantify these effects of the bathymetric steepness, the following indicative scalar values are plotted as a function of the steepness parameter C:

- The maximum and mean along-channel velocity amplitude (depth-dependent) computed in the central cross-section $\{L/2\} \times [-B/2, B/2]$ to prevent interference of the seaward boundary layer,

- the maximum cross-channel velocity amplitude (depth-dependent) computed in the central cross-section,

- the phase differences between surface elevation and depth-averaged along-channel velocity at the point $(L/2, 0)$ in the middle of the channel and at the point $(L/2, -B/2+100)$, located close to one of the banks of the estuary. The point $(L/2, -B/2+100)$ is used instead of a point on the bank to reduce the influence of numerical errors, which get relatively large close to the bank for large values of C, since velocities are very small there.

The steepness parameter ranges from $C = 0$ (flat bed) to $C = 12$.

In Figures 4.16 and 4.17, the dependence of the mean and maximum along-channel velocity, and maximum cross-channel velocity on the steepness parameter C is shown, respectively. As expected from Subsection 4.2.1, the maximum along-channel and cross-channel velocities increase as the bathymetric steepness increases. The maximum along-channel velocity grows faster between $C = 0$ and $C = 1$ than in the rest of the range of C. Furthermore, the maximum cross-channel velocity seems to stop growing close to $C = 12$. Finally, the mean along-channel velocity in the central cross-section decreases as the steepness increases, but after $C \approx 3$, it remains constant.

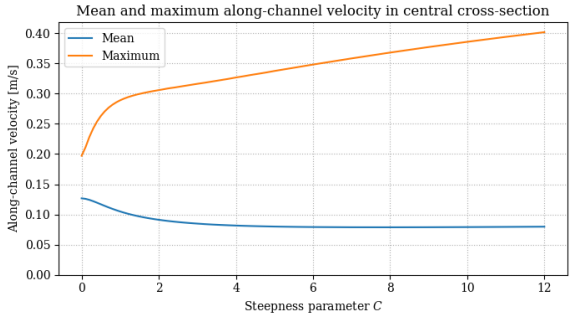

Figure 4.16: Mean and maximum along-channel velocity amplitude in the central cross-section as a function of the steepness parameter C.

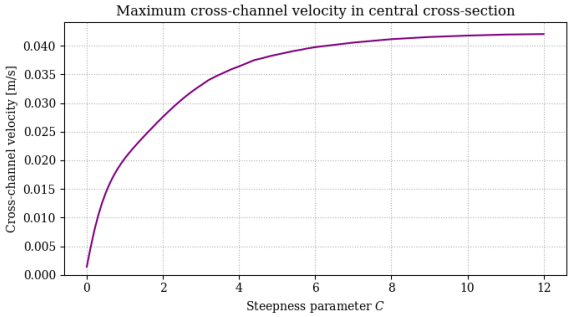

Figure 4.17: Maximum cross-channel velocity amplitude in the central cross-section as a function of the steepness parameter C.

To study the dependence of the mean along-channel velocity on the steepness parameter C, one could take inspiration from Rozendaal et al. (2024) and parametrise the bed friction term in a one-dimensional (1DH) model (see for example Friedrichs (2010)) exactly using analytical vertical and lateral structures. In this work, the authors give an exact parametrisation of three-dimensional bed friction in a two-dimensional model. To achieve similar results in the model of this thesis, the analytical vertical and lateral structures of Winant (2007) can be used; this model is very similar to the model of this thesis. Using the dependence of this cross-sectionally averaged friction parameter on the steepness parameter C, one could explain the dependence of the cross-sectionally averaged velocity on C as shown in Figure 4.16, assuming that a large friction parameter corresponds to a small cross-sectionally averaged velocity. However, because of time constraints, this analysis is not carried out in this thesis.

The dependence of the phase difference on C is shown in Figure 4.18. As expected from Subsection 4.2.1, the phase difference above the channel decreases as C increases, and the phase difference close to the banks increases as C increases. There is a conspicuous peak at $C = 4.4$ that breaks the trend, but this is likely the result of numerical error and not reflective of physical behaviour; nothing about the bathymetry corresponding to $C = 4.4$ is qualitatively different than the bathymetries corresponding to neighbouring values of C.

Figure 4.18 indicates that the phase difference between the surface elevation and the along-channel velocity is strictly smaller than $\pi/2$. Indeed, Li and O'Donnell (2005) explain that due to bed friction, the phase difference between surface elevation and flow is smaller than $\pi/2$. The tide may be decomposed into an incident and reflected wave. Because of bed friction, the reflected wave is slightly weaker than the incident wave, which causes the tide to be closer to a *progressive wave*, i.e. with a phase difference of 0. Because the estuary considered in this thesis is short, the reflected wave is only slightly weaker than the incident wave. Therefore, the phase difference is only slightly smaller than $\pi/2$.

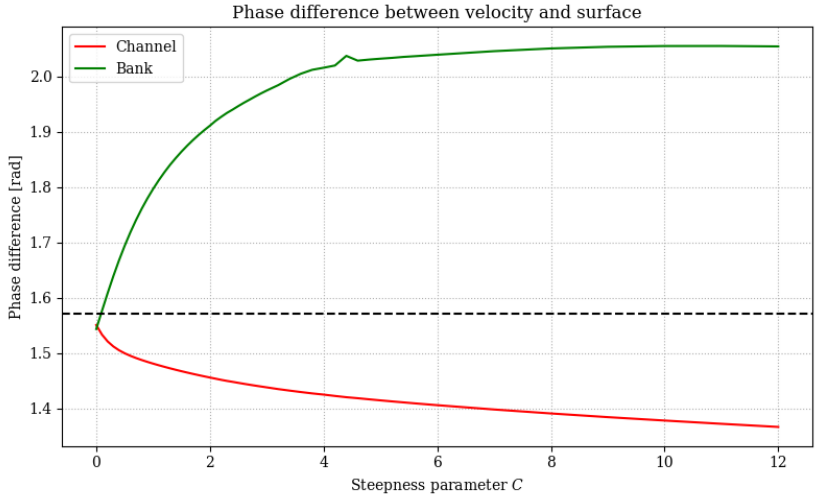

Figure 4.18: Phase difference between water surface and depth-averaged along-channel velocity in the middle of the channel and close to the banks, plotted against the steepness parameter C. The dashed line indicates $\pi/2$.

However, Figure 4.18 shows phase differences that are much larger than $\pi/2$ for non-flat bathymetries. Thus, additional analysis is needed to explain the results in this figure. As before, this additional analysis is not performed in this thesis due to time constraints.

4.3. Advection-induced residual flow

Now, the residual (subtidal) flow patterns that emerge from advection are studied. Since river discharge and density gradients were neglected, advection is the only mechanism that produces residual flow. As mentioned before, convergence of the Newton method proved to be a significant challenge; to be able to generate interpretable results, the equations had to be modified slightly. In Subsection 4.3.1, this modification is described and it will be argued that the results are most likely still valid despite the modification. Afterwards, the same approach as Section 4.2 is taken: two solutions associated to different steepness parameters are compared qualitatively in Subsection 4.3.2 and the effect of steepness is quantified using scalar values in Subsection 4.3.3

4.3.1. Divergence of the Newton method

It can be shown that the Newton method converges in one iteration if it is applied to linear problems. Therefore, there is a connection between how fast the Newton method converges and how strong the non-linearities in the equations are. Inspired by this, one may aid convergence by suppressing non-linear terms. To this end, the equations are modified in two ways.

Firstly, advective terms are *only* included in the equations for the residual flow. That means that the semidiurnal tidal motion does not change compared to Section 4.2, and overtides ($M_4, M_6, \ldots$) and their non-linear interactions with M_2-flow and residual flow are neglected. Thus, the residual flow is only affected by momentum advection from the semidiurnal tide and the residual flow itself. Later, the results show that the influence of momentum advection through the residual flow on the residual flow itself is negligible. Therefore, it is likely that advection from residual flow does not significantly affect semidiurnal flow as well.

Secondly, the parameter ε is chosen to be equal to 0.1 instead of 1. The momentum equations for the residual flow (2.3b-c) then transform to

$$\varepsilon(\overline{uu}_x + \overline{vu}_y + \overline{wu}_z) - f\overline{v} = -g\overline{\zeta}_x + \mathscr{A}_v\overline{u}_{zz}, \tag{4.5a}$$

$$\varepsilon(\overline{uv}_x + \overline{vv}_y + \overline{wv}_z) + f\overline{u} = -g\overline{\zeta}_y + \mathscr{A}_v\overline{v}_{zz}. \tag{4.5b}$$

Here, the bar denotes taking the average over the tidal period. Note that the time derivative vanishes because residual flow is considered. The momentum equations in ς-coordinates and the projected equations transform accordingly.

It is difficult to predict how the residual flow structure is affected by using $\varepsilon = 0.1$ instead of $\varepsilon = 1$. Ideally, this only affects the scale of the residual flow, and not its spatial structure. However, this is not guaranteed. Even in this case, analysis of the solutions will be valuable, as this would later allow us to conclude that the spatial structure of residual flow is significantly affected by the strength of advection, once solutions with $\varepsilon = 1$ have been computed.

Even with these modifications convergence is not certain, but when the initial guess was chosen to be the solution of the linear problem, convergence was achieved for nearly all values of C considered; the only value for which the Newton method did not converge was $C = 12$, where the norm of the residual did not tend to zero, but remained approximately constant. However, the norm of the residual was small enough to be confident that the solution is approximately correct. Moreover, the results for $C = 12$ (shown later in Subsection 4.3.3) do not break trends.

As for why convergence is such a challenge, I have two hypotheses. Firstly, the reason could be the seaward boundary layer. The results indicate that in this boundary layer, residual currents are an order of magnitude stronger than outside this layer, which suggests that the advective terms are very influential here. Possibly, this occurs because of unphysical large gradients in the tidal motion. Secondly, there are noticable numerical artifacts present in the solutions, especially in v, w and their gradients. It is possible that these artifacts strengthen the advective terms, which makes convergence more difficult. More analysis is necessary before definitive conclusions can be drawn. Methods to avoid the above issues are discussed in Section 5.2.

4.3.2. Comparison of two solutions

Like Subsection 4.2.1, the residual flow patterns associated with a gently sloping bathymetry ($C = 0.1$) are compared to the patterns associated with a steep bathymetry ($C = 6$).

Along-channel velocity

In Figure 4.19 the residual along-channel velocities corresponding to both bathymetries are shown, from a top perspective and in the central cross-section ($x = L/2$).

Looking at Figure 4.19, it becomes clear that the seaward boundary layer discussed before strongly affects the advective residual flow. In the nearly flat estuary ($C = 0.1$), the contourlines are curved, and in the steep estuary ($C = 6$), the currents even switch sign in the boundary layer. Like before, these flow patterns are expected to be unrealistic and hence, exclude the seaward boundary layer from the analysis.

Comparing the left panels of Figure 4.19 to the right panels, one can observe that the residual flow is stronger in the case $C = 6$ and the maximum positive flow is noticeably more off-center. These observations can be interpreted by looking at which terms in the residual momentum equations are dominant. To this end, Figures 4.20 and 4.21 show the cross-sectional views of each forcing term, computed using the solution corresponding to $C = 0.1$ and $C = 6$, respectively. The term 'forcing' is defined loosely as every term in the along-channel residual momentum balance (4.5a) except $\mathscr{A}_v \overline{u}_{zz}$.

The contribution of advection from tidal motion is calculated as follows: the semidiurnal flow can be written in terms of the harmonic basis functions as $u_1(x,y,z)\cos(2\pi\sigma t) - u_{-1}(x,y,z)\sin(2\pi\sigma t)$. Thus, the product uu_x is given by

$$\frac{1}{2}\left(u_1\frac{\partial u_1}{\partial x} + u_{-1}\frac{\partial u_{-1}}{\partial x}\right) + \frac{1}{2}\left(u_1\frac{\partial u_1}{\partial x} + u_{-1}\frac{\partial u_{-1}}{\partial x}\right)\cos(4\pi\sigma t) - \frac{1}{2}\left(u_1\frac{\partial u_{-1}}{\partial x} + u_{-1}\frac{\partial u_1}{\partial x}\right)\sin(4\pi\sigma t), \tag{4.6}$$

and hence, the contribution of uu_x to the residual momentum equations is given by $\frac{1}{2}(u_1(u_1)_x + u_{-1}(u_{-1})_x)$. Similar formulas can be derived for the contribution of the other advective terms to the residual momentum equations.

In the case $C = 0.1$, Figure 4.20 shows that the along-channel residual flow is governed by a balance between momentum advection through along-channel tidal motion and the surface gradient. The surface gradient is determined as a reaction to other forcing mechanisms in such a way that the cross-sectionally averaged residual along-channel velocity vanishes. This is required by the depth-integrated continuity equation. Indeed,

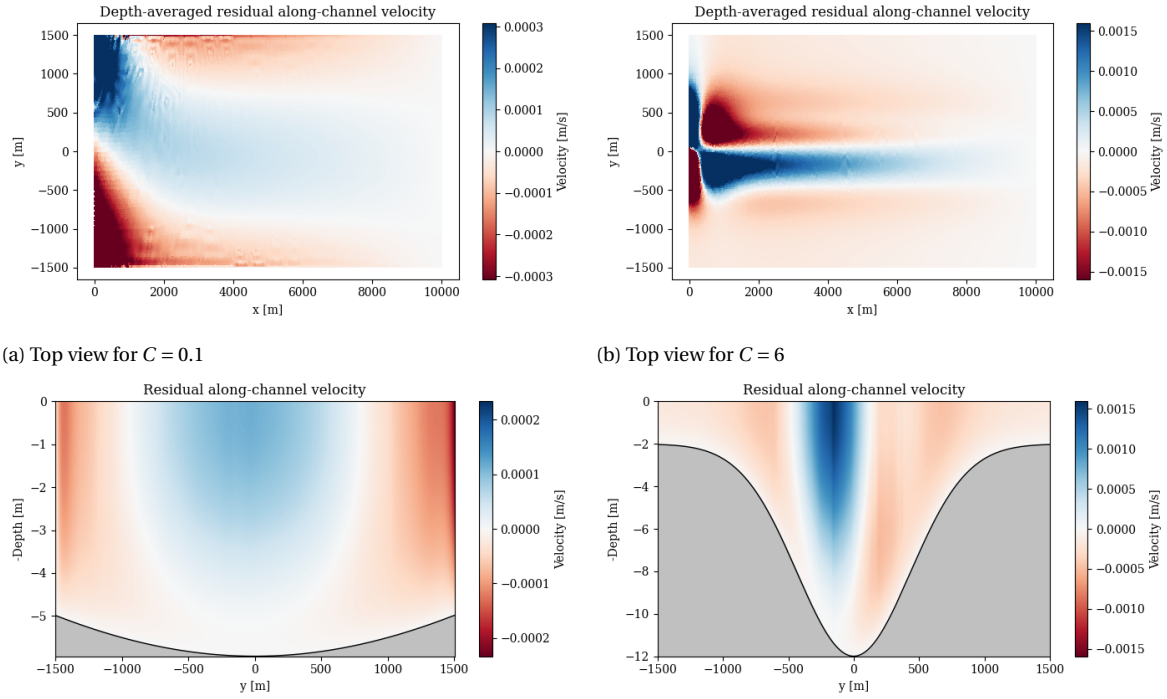

(a) Top view for $C = 0.1$

(b) Top view for $C = 6$

(c) Cross-sectional view for $C = 0.1$

(d) Cross-sectional view for $C = 6$

Figure 4.19: Residual along-channel flow for two different bathymetries ($C = 0.1$ (left) and $C = 6$ (right)), showed from two different perspectives: a top view (top) and a cross-sectional view (bottom). Positive (negative) velocities are signified by blue (red) and indicate flow into (out of) the channel. The range of the colour is restricted to the maximum absolute velocity in the central cross-section; in the seaward boundary layer, velocities are much larger than suggested here.

since the time derivative of residual quantities vanishes, it holds that

$$\left(\int_{-H}^{0} u \, \mathrm{d}z\right)_x + \left(\int_{-H}^{0} v \, \mathrm{d}z\right)_y = 0.$$

Integrating this equation over the width of the estuary and using that there is no lateral transport through the closed boundaries, one finds that the cross-sectionally averaged residual along-channel velocity is constant. Because the river discharge was neglected, the cross-sectionally averaged residual along-channel velocity is equal to 0 as well.

In the case $C = 6$, Figure 4.21 shows that the residual flow also is governed by a balance between advection and surface gradients. However, in this case, advection of momentum through lateral and vertical tidal motion is significant as well. In fact, close to the borders of the deep channel, lateral advection is stronger than along-channel advection. Lateral advection is able to become part of the dominant balance because of two reasons: lateral tidal velocities are larger in the presence of steep bathymetries and the difference between along-channel tidal velocities in the channel and velocities above the banks is larger, leading to a large lateral gradient u_y. Because of the Coriolis effect, the structure of the lateral velocity is asymmetric and hence, the lateral advection (and vertical advection through (3.16)) is asymmetric as well. Because these processes are part of the dominant balance, the total forcing is asymmetric, which causes the asymmetry in the residual along-channel flow.

Furthermore, along-channel tidal velocities are larger in the case $C = 6$ than in the case $C = 0.1$. Because river discharge was neglected, the along-channel velocity must decay to zero. It follows that the larger along-channel velocities in the steep estuary decay faster than velocities in the nearly flat estuary. Therefore, both u and u_x are larger and hence, advection through along-channel flow is stronger. Combined with the stronger lateral and vertical advection, the total forcing in the residual equation is larger, which is likely the reason for the stronger residual along-channel flow in the steep estuary.

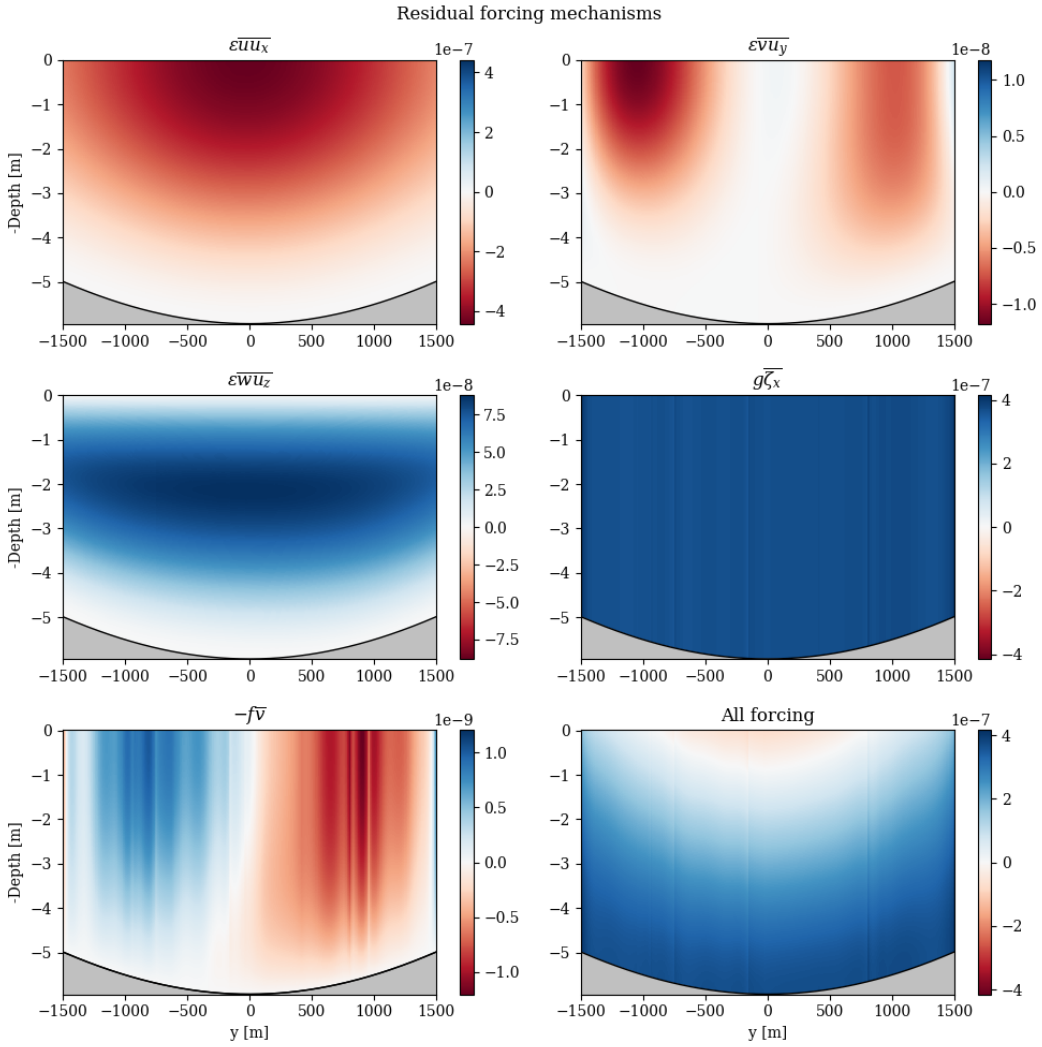

Figure 4.20: Forcing balance in residual along-channel momentum equation in the case $C = 0.1$. The bar denotes averaging a quantity over the tidal period.

Cross-channel velocity

In Figure 4.22, the residual cross-channel velocities are shown. It is clear that Figure 4.22 is riddled with numerical artifacts. In fact, Figure 4.22d seems to indicate that the cross-sectionally averaged residual cross-channel velocity does not vanish. This would imply a net lateral transport, which is physically impossible. Because of these artifacts, a sensitivity analysis for residual lateral velocities is not carried out; any indicative scalar value would be significantly affected by the artifacts.

However, there are still useful conclusions to be drawn from Figure 4.22: in both cases, momentum advection of tidal motion causes residual flow towards the banks of the estuary. Furthermore, lateral velocities are stronger if the bathymetry is steeper.

4.3.3. Quantifying the effects of steepness

In this subsection, the observations about the increased strength and asymmetry of the residual along-channel flow are quantified using two indicative scalar values:

- The *exchange rate* Q over the central cross-section as a measure of the strength of the residual flow, which is defined as the total amount of residual inflow (Li & O'Donnell, 2005). Because river discharge was neglected, the exchange rate could equivalently be defined as minus the total amount of residual

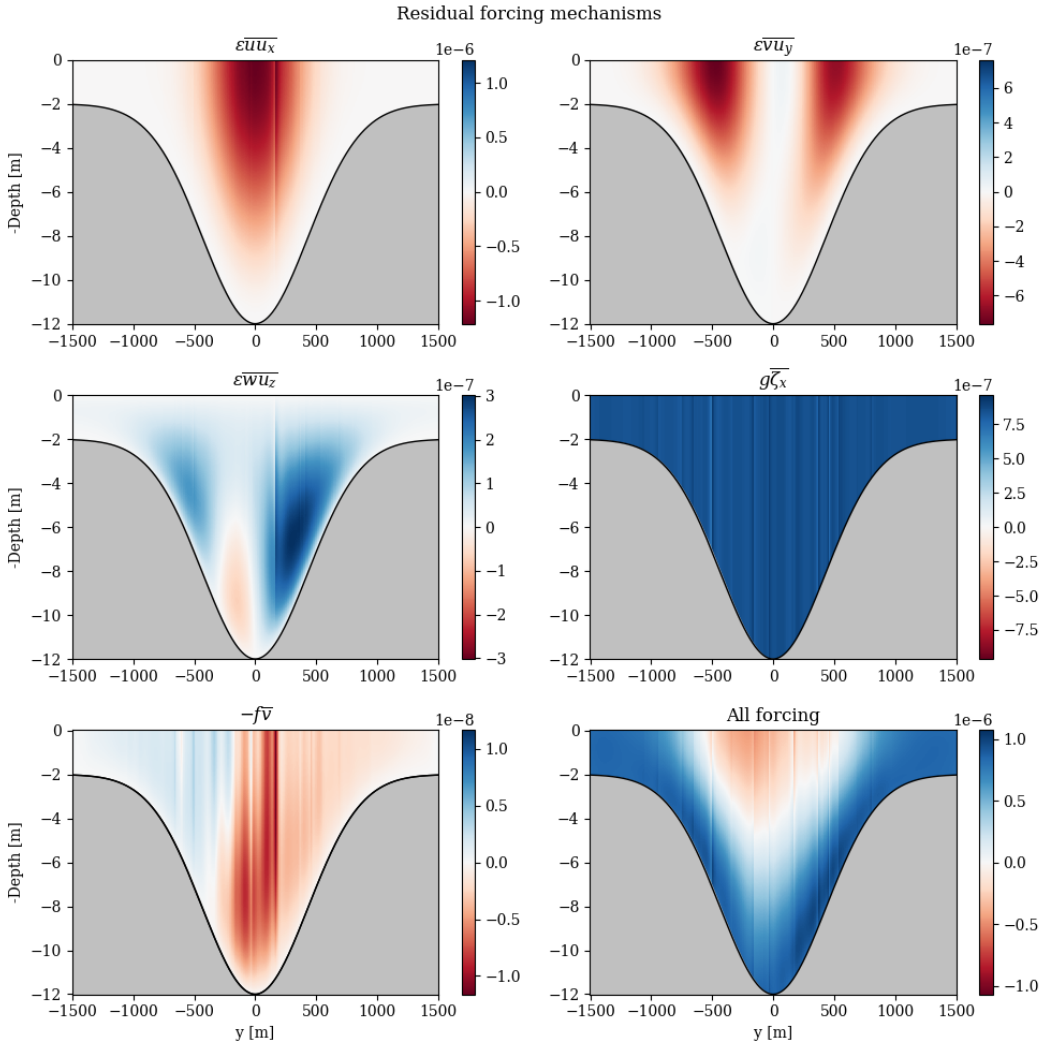

Figure 4.21: Forcing balance in residual along-channel momentum equation in the case $C = 6$.

outflow. The exchange rate is computed by setting the outflow to zero and integrating over the cross-section.

- The center of mass (COM) of the residual depth-integrated inflow as a measure of the lateral asymmetry of the residual flow. If the inflow is divided by the exchange rate such that it integrates to 1 and constitutes a probability density, the center of mass is equal to the expected value of this probability distribution. More precisely, the center of mass is computed using the following formula:

$$\text{COM} = \frac{1}{Q}\int_{-B/2}^{B/2} y \int_{-H}^{0} \max\{\overline{u}, 0\}\, \mathrm{d}z\, \mathrm{d}y, \tag{4.7}$$

  where $\overline{u}$ denotes the residual along-channel velocity.

These integral quantities are used instead of (the location of) the maximum because integral quantities are much less sensitive to numerical errors in the solution than maxima. In Figures 4.23 and 4.24, the dependence of Q and COM on the steepness parameter is shown.

Figure 4.23 indicates that the exchange rate grows approximately linearly with the steepness parameter and it shows no signs of slowing down at $C = 12$. This figure shows that the dependence of the exchange rate on C bears a remarkable resemblance to the dependence of the maximum tidal velocity amplitude on C. For low values of C, it was shown that the forcing balance for residual flow is dominated by along-channel advection.

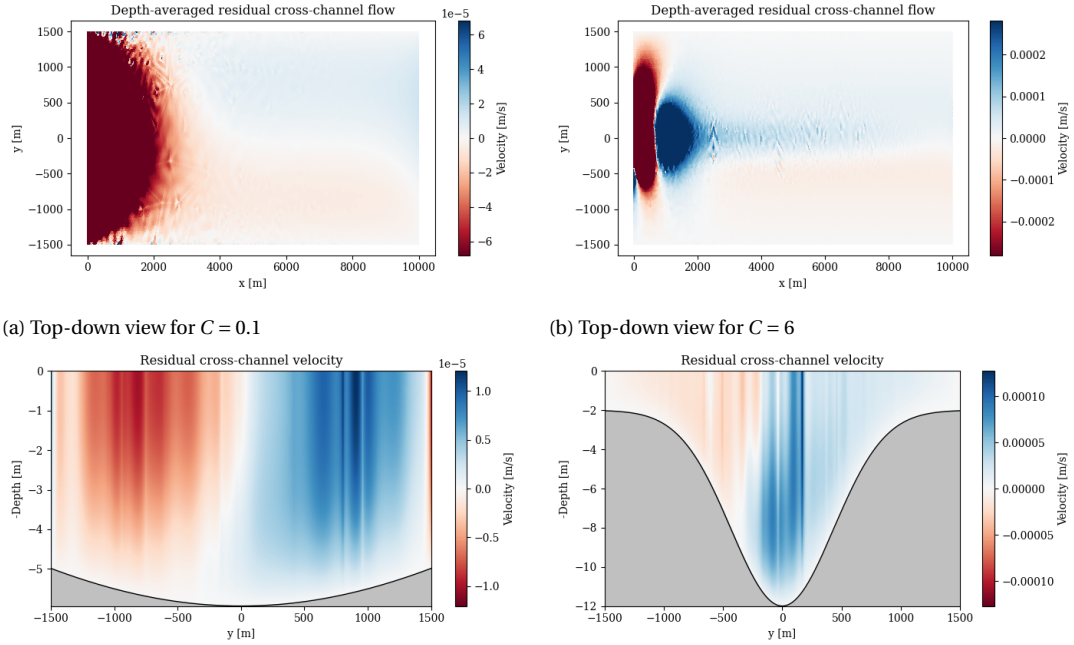

(a) Top-down view for $C = 0.1$

(b) Top-down view for $C = 6$

(c) Cross-sectional view for $C = 0.1$

(d) Cross-sectional view for $C = 6$

Figure 4.22: Residual cross-channel flow for two different bathymetries, showed from two different perspectives. Positive velocities (blue) indicate flow towards positive values of y. The range of the colour is restricted to the maximum absolute velocity in the central cross section.

Therefore, it seems likely that for those values of C, the increase of exchange rate as the steepness parameter increases is linked to the increase of semidiurnal tidal velocities.

Figure 4.24 shows that the center of mass first moves towards to lower bank of the river, reaching its maximum distance from $y = 0$ at $C = 6$, before moving back to $y = 0$ again. Figures 4.10 and 4.11 show that the locations of the maximum lateral tidal velocities do not move inward as the steepness increases to $C = 6$. However, comparing Figure 4.11 to Figure 4.25, which shows the amplitudes of cross-channel tidal velocities for $C = 10$, indicates that after $C = 6$, the maxima follow the borders of the deep channel and move inward. Lateral tidal velocities are also stronger in estuaries with steeper bathymetries.

Using these observations, a possible explanation of Figure 4.24 is as follows. For small values of C, lateral advection is unable to balance the symmetric along-channel advection even where it is weaker, leading to a relatively symmetric residual flow pattern. However, as the steepness of the bathymetry increases, the asymmetric lateral advection becomes stronger, leading to more asymmetric forcing, which in turn leads to more asymmetric residual flow. This pattern continues until the maxima of the lateral tidal velocities (and the maxima of u_y) have started to move to the center of the channel, causing them to encroach on the territory of the along-channel advection, which is still stronger. At this point, the influence of lateral advection diminishes and accordingly, the residual flow pattern becomes more symmetric. Because the asymmetry in the spatial structure of semidiurnal lateral velocities arises due to Coriolis forces, the asymmetry in the structure of the residual along-channel velocity is indirectly caused by the Coriolis effect, even though the contribution of the Coriolis terms in the along-channel residual momentum balance (4.5a) is negligible, as shown in the bottom-left panels of Figures 4.20 and 4.21

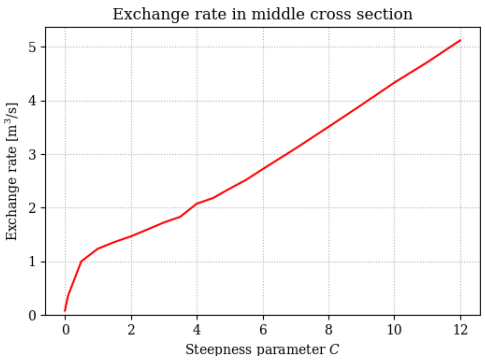

Figure 4.23: Exchange rate as a function of the steepness parameter C.

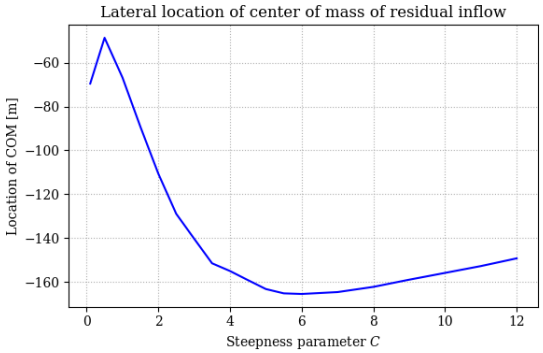

Figure 4.24: Lateral location of center of mass of residual inflow as a function of the steepness parameter C.

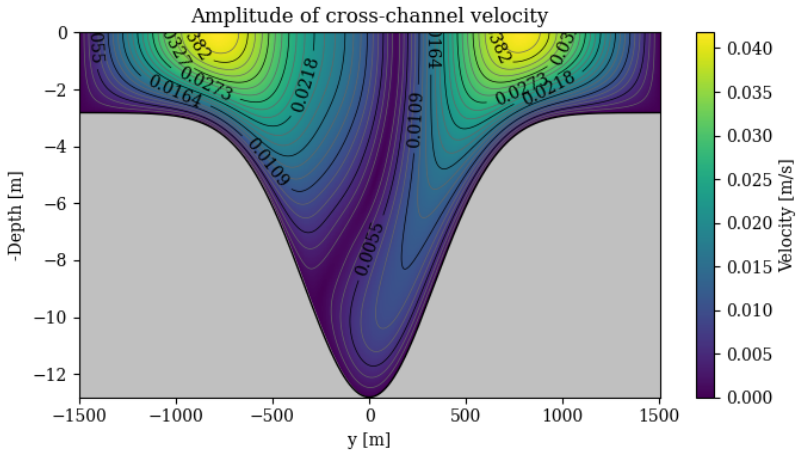

Figure 4.25: Amplitude of M_2-cross-channel velocity in the central cross-section $\{L/2\} \times [-B/2, B/2]$ for steepness parameter $C = 10$. Lighter (darker) colours indicate larger (smaller) velocities.

5

Discussion

In this section, differences and similarities between the results of this thesis and previously known results are discussed (Section 5.1). After, a brief overview is given of which aspects of the model and solution method should be improved to be able to answer the research questions in a more satisfying way (Section 5.2).

5.1. Embedding in the literature

This section is subdivided in two subsections. In Subsection 5.1.1, the results of Section 4.2 about the semidiurnal tidal motion are compared to previous studies. Likewise, in Subsection 5.1.2, the results of Section 4.3 about residual flow are compared to the literature.

5.1.1. Semidiurnal tidal motion

There are many studies that investigate linear tidal motion using idealised models. Li and Valle-Levinson (1999) use a depth-averaged (2DH) model to describe tidal motion in rectangular estuaries with arbitrary lateral bathymetries. They study the along- and cross-channel tidal currents for various complex bathymetries, among which bathymetries that match bathymetries considered in this thesis very closely (see Figure 1a in their paper). They find along-channel and cross-channel velocity patterns that look very similar to the patterns found in Figures 4.8, 4.7, 4.10 and 4.11. The lateral velocities found in this work are of the same order of magnitude as my results, but their along-channel velocities are much larger than the velocities found in Section 4.2. However, the domain of Li and Valle-Levinson (1999) is much longer than the domain considered in this thesis. In the last ten kilometres of their domain, the order of magnitude of the along-channel velocity *does* match the results of this work.

The work of Winant (2007), which was discussed before, uses a fully three-dimensional model to study the effects of Coriolis forces on the three-dimensional tidal hydrodynamics. Comparing his results to mine, one can see that for the matching value of the friction parameter δ (for $C = 6$, $\delta \approx 1$), the along-channel velocity results of Winant (2007) are similar to my results; both the order of magnitude and the spatial structure match. Furthermore, his results show that the phase difference between water surface and velocity depends on location, and that velocities in the deep channel are more delayed (or equivalently, less ahead) than velocities close to the banks.

Comparing Figure 5.1, which shows the semidiurnal lateral velocity amplitude of Winant's model, to Figure 5.2, which shows the lateral velocity amplitude resulting from the model of this work applied to a domain that only differs in the length (50 km in the results depicted by Figure 5.1 and 10 km in the results depicted by Figure 5.2), one can see that the spatial structure of the lateral velocities is similar. However, the location of the smaller of the two local maxima is completely different: in Figure 5.1, the smaller local maximum is located deep in the channel, and in Figure 5.2, the smaller local maximum is located at the water surface. Furthermore, the lateral velocity amplitudes are much larger in Figure 5.1 than in Figure 5.2. Because Winant's model is so similar to ours, and the width and bathymetry match, the length is likely the source of the discrepancy.

This would indicate that varying the length of the estuary has significant effects on both the size and the lateral structure of semidiurnal cross-channel velocities.

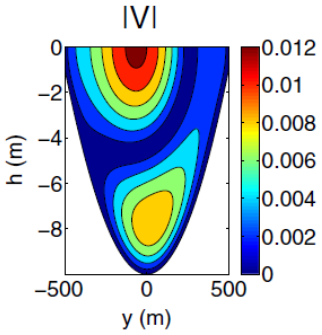

Figure 5.1: Semidiurnal lateral velocity amplitudes [m/s] for a rectangular estuary with a length of 50 km, width of 1 km and a parabolic lateral bathymetry $H(\eta) = 2 + 8(1-\eta^2)$ obtained with Winant's model. Source: Figure 11 in Kumar et al. (2016), who also compared their model to Winant's model.

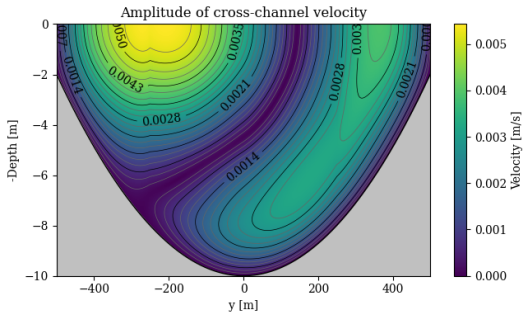

Figure 5.2: Semidiurnal lateral velocity amplitudes [m/s] for a rectangular estuary with a length of 10 km, width of 1 km and a parabolic lateral bathymetry $H(\eta) = 2 + 8(1-\eta^2)$ obtained with the model of this thesis.

Ensing et al. (2015) used a three-dimensional perturbative model to study lateral tidal motion in response to bathymetry steepness, among other factors. While their lateral velocity structure is different than the one presented by Figures 4.10 and 4.11, they do find that increasing bathymetry steepness strengthens lateral tidal velocity. The structural differences are likely due to the differences in model set-up and domain. For instance, Ensing et al. (2015) include width-convergence effects and a tidally varying salinity, which can be a major driver of lateral tidal motion (Lerczak & Geyer, 2004).

5.1.2. Advection-induced residual flow

As for the advection-driven residual flow, Li and O'Donnell (2005) used a depth-averaged perturbative model to study the effects of channel length on the residual flow. They found that the channel length (relative to the quarter tidal wave length) has a profound effect on the structure of the residual flow: for short channels, water flows into the estuary through the deep channel and out closer to the banks. For long channels, this is exactly the other way around. Since this thesis considered short channels, the findings in Section 4.3 match their results. The depth-averaged residual velocity vectors found using their model, applied to a long estuary with a Gaussian lateral bathymetry, are shown in Figure 5.3. In the last ten kilometres of the domain of Figure 5.3, the residual flow matches the results found in this thesis: the flow points into the estuary in the deep channel and from the channel towards the banks. Since the authors state that their results for a *short* channel resemble the results for a long channel close to the riverine boundary, the results in this thesis match the results of Li and O'Donnell (2005) in short channels.

Finally, Huijts et al. (2009) study the lateral distribution of residual flow in response to various factors using a cross-sectional model that assumes uniform along-channel conditions. Because they use a perturbation method to solve their equations, they are able to decompose the solution into contributions from each forcing mechanism, among which momentum advection from semidiurnal tidal flow. Furthermore, they give formulas to compute residual velocity scales for each forcing mechanism. Comparing their Figure 9 to Figure 4.19, it can be seen that the residual flow found in this thesis differs greatly from the results of Huijts et al. (2009). Both the velocity scales and the lateral structure of the residual along-channel velocity are completely different. In Table 5.1, the residual along-channel velocity scales observed in Figure 4.19 divided by ε are compared to the expected velocity scales using the formulas in Huijts et al. (2009), which shows that the formulas of Huijts et al. (2009) significantly underestimate the strength of the residual current. Furthermore, the authors find that residual current flows into the estuary in one half of the cross-section, and out of the estuary in the other half (see their Figure 9h), whereas the results of this thesis indicate inflow through the channel and outflow at the shallower sides.

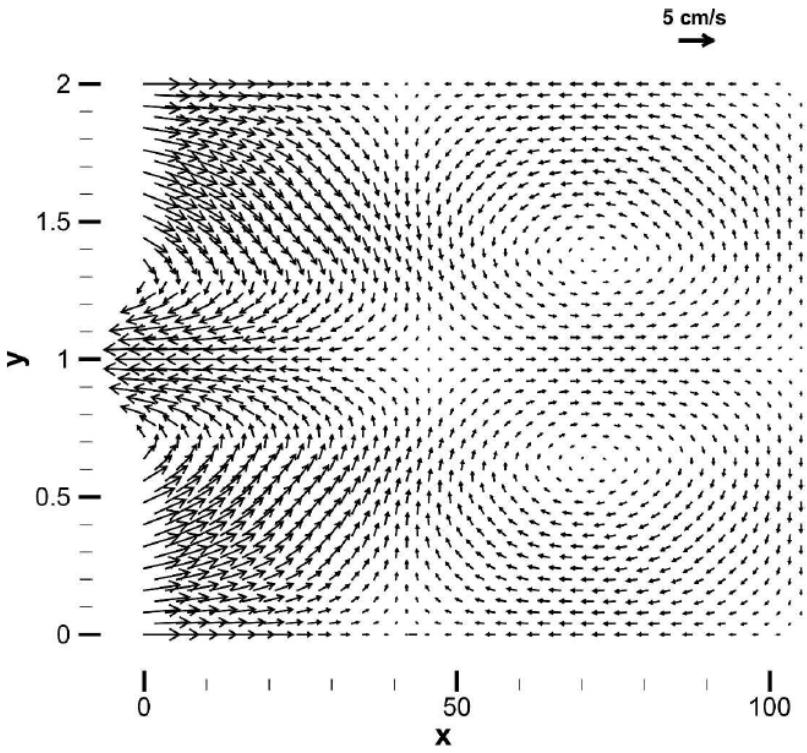

Figure 5.3: Depth-averaged residual velocity vectors found using the model of Li and O'Donnell (2005), applied to a rectangular estuary with $L = 105$ km, $B = 2$ km and a Gaussian lateral bathymetry $H(\eta) = 5 + 10\exp(-8.16\eta^2)$. Adapted from Figure 2 in Li and O'Donnell (2005).

Steepness parameter C	Figure 4.19 divided by ε	Expected from Huijts et al. (2009)
0.1	$2 \cdot 10^{-3}$ m/s	$2 \cdot 10^{-5}$ m/s
6	$1 \cdot 10^{-2}$ m/s	$3 \cdot 10^{-3}$ m/s

Table 5.1: Residual along-channel velocity scales observed in Figure 4.19 compared to the velocity scales expected from the formulas in Table 2 of Huijts et al. (2009). The velocities observed in Figure 4.19 are divided by ε to account for the multiplication discussed in Subsection 4.3.1.

Because Huijts et al. (2009) use a cross-sectional model, along-channel velocity gradients are neglected. Since it was found that residual along-channel flow is driven by a balance of forces that includes along-channel momentum advection as a dominant factor, this is likely the source of the differences. This explanation is consistent with the result that residual flow in estuaries with steeper bathymetries is driven by a balance between advection from all tidal velocity directions, whereas residual flow in the nearly flat estuary is forced primarily by along-channel momentum advection. Indeed, the disparity between the predicted velocity scales from Huijts et al. (2009) and the actual velocity scales is smaller in the case $C = 6$. In any case, the findings of this thesis suggest that at least in short channels where along-channel velocity gradients are large, cross-sectional models are insufficient to describe residual flow due to momentum advection from semidiurnal tidal motion.

5.2. Outlook

At several points in this chapter, numerical issues hampered interpretation of the results by forcing us to limit the domain to short estuaries, to modify the equations to achieve convergence, and to limit our analysis of lateral residual velocities. In order to answer the research questions completely, several steps need to be taken:

1. Implement a parallel version of the model that can be solved by large computing clusters and supercomputers. This will allow us to compute numerically converged solutions for realistically sized estuaries, as well as overtides ($M_4, M_6, \ldots$) and their interactions with each other, even when advection-driven flow is leading-order.

2. Investigate why convergence of the Newton method is so challenging and find a solution to this problem. Previously, two hypotheses for why the method kept diverging were presented. If numerical artifacts are the reason for divergence, then point 1 will solve these convergence problems. On the other hand, if the seaward boundary layer is the source of divergence, it could be possible to reduce the size and strength of the boundary layer by choosing a seaward boundary condition that fits better with the bathymetry than a uniform signal. For example, the analytical solutions of Winant (2007) for the water surface elevation could be used instead.

Furthermore, some non-linear physical processes have been neglected that might be influential factors for hydrodynamics in estuaries, especially when the bathymetry becomes very steep. Firstly, it was assumed that the free surface was not part of the domain, so integration over depth and evaluation of velocities at the surface for the surface boundary conditions did not involve one of the unknowns of the model. Dijkstra et al. (2017) have shown that these non-linear effects are of order $\mathcal{O}(\zeta / H)$, showing that they might become dominant if the domain contains shallow areas, which is the case for many values of C. Secondly, it was assumed that the eddy viscosity $\mathscr{A}_v$ was constant. In reality, the eddy viscosity scales with the size of the turbulent eddies, which scales with the local water depth (Friedrichs & Hamrick, 1996). For high values of C, the deepest point in the domain can be six times as deep as the shallowest point, implying that in reality, six times as much energy should be dissipated by the turbulent eddies. Once these physical effects are included, the research questions can be answered more completely.

6

Conclusion

This thesis presented a three-dimensional idealised model for the hydrodynamics in estuaries, based on the Reynolds-averaged shallow water equations with constant density and eddy viscosity. To solve this model, a truncation method was employed, which expands the unknowns in terms of a harmonic Fourier basis and a vertical basis defined using an eigenvalue problem. After projecting the equations and boundary conditions onto these bases, the resulting system of two-dimensional PDEs is discretised using a spectral element method and subsequently solved using the Newton-Raphson method. To be able to give numerically converged results with a standard computer, the model was applied to short estuaries (10 kilometres long).

Using the model, the effect of steep lateral bathymetries on the (linear) semidiurnal tidal motion (**Q1**) and advection-induced residual flows (**Q2**) was studied, by comparing solutions associated to gently sloping and steep bathymetries and quantifying observations.

It was found that the semidiurnal water surface elevation behaves approximately like a uniform oscillating surface regardless of the steepness of the bathymetry, because the estuary is much shorter than the tidal wave length, and because lateral variations in the water surface scale with the ratio between estuary width and length, which is small even in a short estuary.

Bathymetric steepness *does* have a significant effect on along-channel tidal velocities. In estuaries with steeper bathymetries, velocities are larger in the deeper channel and smaller above the shallower banks. This can be explained using the depth: the bed boundary layer has more space to develop in deep water than in shallower water.

The steepness also has an effect on the strength and spatial structure of the lateral velocities. At flood, water flows in through the deep channel and from the deep channel, out onto the banks. At ebb, the pattern is reversed. For steeper bathymetries, both the flow into the channel, and from the channel onto the banks are stronger. Because the water surface elevation is an approximately uniform oscillating surface, and along-channel currents are stronger in the channel than on the banks, water *must* flow onto the banks from the channel in order for the surface elevation to remain uniform.

Finally, the tidal flow associated to steep bathymetries exhibits significant phase differences between velocities in the channel and velocities close to the banks; velocities close to the banks are ahead compared to velocities in the channel. These phase differences grow as the bathymetry becomes steeper.

These results are consistent with other studies. While the lateral structure of cross-channel velocities differs known results, this can likely be explained by the fact that the estuaries considered in this thesis were short.

Because the Newton method was not converging, some modifications had to be made to the equations to be able to compute advection-driven residual flow. Firstly, advective effects on the semidiurnal tide and overtides were neglected, and secondly, the advective terms in the equations for the residual flow were multiplied by 0.1. This means that the resulting residual flows are generated because of momentum advection from the semidiurnal tide and the residual flow itself, and they are weaker than they would be in reality.

The results indicate that the along-channel residual current is characterised by inflow through the deep channel and outflow closer to the banks. Steeper bathymetries generate stronger residual flows, and notably more asymmetric flow structures. Looking at the forcing balance, one can see that the along-channel residual flow is governed by a balance between momentum advection from semidiurnal tidal velocities and along-channel surface gradients. In estuaries with gently sloping bathymetries, the contribution from advection is dominated by along-channel advection, and in estuaries with steep bathymetries, the contribution from advection is more balanced between along-channel, cross-channel and vertical momentum advection. Because the cross-channel velocity structure is asymmetric due to the Coriolis effect, the forcing balance is asymmetric as well in these estuaries.

The cross-channel flow is characterised by flow from the channel towards the banks, and residual cross-channel currents become stronger if the bathymetry becomes steeper. However, because the lateral residual velocities are riddled with numerical artifacts, one should be hesitant about drawing definitive conclusions.

Comparing the results to a depth-averaged model, one can see qualitatively similar residual flows, though the new model did not reproduce the same residual circulation. Bigger differences can be found when comparing the model to a cross-sectional model: the spatial structure of the along-channel residual flow is completely different and the three-dimensional model predicts much stronger residual currents than the cross-sectional model. The source of this discrepancy is likely the neglected along-channel velocity gradients by the cross-sectional model. Indeed, it was found that along-channel momentum advection was a dominant contributor to the residual flow. Thus, the results suggest that at least for short channels where along-channel velocity gradients are large, cross-sectional models are insufficient to study advection-driven residual flows.

Bibliography

Alam, M. Z., Carpenter-Boggs, L., Mitra, S., Haque, M., Halsey, J., Rokonuzzaman, M., Saha, B., & Moniruzzaman, M. (2017). Effect of Salinity Intrusion on Food Crops, Livestock, and Fish Species at Kalapara Coastal Belt in Bangladesh. *Journal of Food Quality*, 1–23. https://doi.org/10.1155/2017/2045157

Bosboom, J., & Stive, M. J. F. (2023). *Coastal Dynamics*. TU Delft Open. https://doi.org/10.5074/T.2021.001

Burchard, H., & Petersen, O. (1997). Hybridization between σ- and z-coordinates for improving the internal pressure gradient calculation in marine models with steep bottom slopes. *International Journal for Numerical Methods in Fluids*, *25*, 1003–1023.

Burchard, H., & Schuttelaars, H. M. (2012). Analysis of Tidal Straining as Driver for Estuarine Circulation in Well-Mixed Estuaries. *Journal of Physical Oceanography*, *42*(2), 261–271. https://doi.org/10.1175/JPO-D-11-0110.1

Cameron, W. M., & Pritchard, D. W. (1983). Estuaries. In M. N. Hill (Ed.), *The Sea* (pp. 306–324, Vol. 2). John Wiley and Sons.

Cloern, J. E., Foster, S. Q., & Kleckner, A. E. (2014). Phytoplankton primary production in the world's estuarine-coastal ecosystems. *Biogeosciences*, *11*, 2477–2501. https://doi.org/10.5194/bg-11-2477-2014

Costanza, R., d'Arge, R., de Groot, R., Farber, S., Grasso, M., Hannon, B., Limburg, K., Naeem, S., O'Neill, R. V., Paruelo, J., Raskin, R. G., Sutton, P., & van den Belt, M. (1997). The value of the world's ecosystem services and natural capital. *Nature*, *387*, 253–260. https://doi.org/10.1038/387253a0

Cushman-Roisin, B., & Beckers, J. M. (2011). *Introduction to Geophysical Fluid Dynamics: Physical and Numerical aspects*. Elsevier Science & Technology.

Davidson, P. A. (2015). *Turbulence: an Introduction for Scientists and Engineers* (2nd ed.). Oxford University Press.

Davis, T., & Duff, I. (1997). An Unsymmetric-Pattern Multifrontal Method for Sparse LU Factorization. *SIAM Journal on Matrix Analysis and Applications*, *18*(1), 140–158. https://doi.org/10.1137/S0895479894246905

Day, M. A. (1990). The no-slip condition of fluid dynamics. *Erkenntnis*, *33*, 285–296. https://doi.org/10.1007/BF00717588

Dijkstra, Y. M., Brouwer, R. L., Schuttelaars, H. M., & Schramkowski, G. P. (2017). The iFlow modelling framework v2.4: a modular idealized process-based model for flow and transport in estuaries. *Geoscientific Model Development*, *10*(7), 2691–2713. https://doi.org/10.5194/gmd-10-2691-2017

Dijkstra, Y. M., Schuttelaars, H. M., & Kranenburg, W. M. (2022). Salt Transport Regimes Caused By Tidal and Subtidal Processes in Narrow Estuaries. *Journal of Geophysical Research*, *127*(12). https://doi.org/10.1029/2021JC018391

Ensing, E., de Swart, H. E., & Schuttelaars, H. M. (2015). Sensitivity of tidal motion in well-mixed estuaries to cross-sectional shape, deepening, and sea level rise: An analytical study. *Ocean Dynamics*, *65*, 933–950. https://doi.org/10.1007/s10236-015-0844-8

Fairbridge, R. W. (1980). The estuary: its definition and geodynamic cycle. In E. Olausson & I. Cato (Eds.), *Chemistry and Geochemistry of Estuaries* (pp. 1–35). Wiley.

Fairchild, T. P., Bennett, W. G., Smith, G., Day, B., Skow, M. W., Möller, I., Beaumont, N., Karunarathna, H., & Griffin, J. N. (2021). Coastal wetlands mitigate storm flooding and associated costs in estuaries. *Environmental Research Letters*, *16*(7). https://doi.org/10.1088/1748-9326/ac0c45

Friedrichs, C. T. (2010). Barotropic tides in channelized estuaries. In A. Valle-Levinson (Ed.), *Contemporary Issues in Estuarine Physics* (pp. 27–63). Cambridge University Press.

Friedrichs, C. T., & Hamrick, J. M. (1996). Effects of channel geometry on cross sectional variations in along channel velocity in partially stratified estuaries. In D. G. Aubrey & C. T. Friedrichs (Eds.), *Buoyancy effects on coastal and estuarine dynamics* (pp. 283–300). AGU. https://doi.org/10.1029/CE053p0283

Gerkema, T. (2019). *An Introduction to Tides*. Cambridge University Press.

Gerkema, T., Zimmerman, J. T. F., Maas, L. R. M., & van Haren, H. (2008). Geophysical and astrophysical fluid dynamics beyond the traditional approximation. *Reviews of Geophysics*, *46*(2). https://doi.org/10.1029/2006RG000220

Google. (n.d.). Satellite images of the Scheldt and Hudson estuaries. Accessed on June 12th 2024 via https://earth.google.com/web.

Haberman, R. (2013). *Applied Partial Differential Equations with Fourier Series and Boundary Value Problems* (5th ed.). Pearson.

Holmes, M. H. (2013). *Introduction to Perturbation Methods*. Springer.

Huijts, K. M. H., Schuttelaars, H. M., de Swart, H. E., & Friedrichs, C. T. (2009). Analytical study of the transverse distribution of along-channel and transverse residual flows in tidal estuaries. *Continental Shelf Research, 29*(1), 89–100. https://doi.org/10.1016/j.csr.2007.09.007

Ianniello, J. P. (1979). Tidally Induced Residual Currents in Estuaries of Variable Breadth and Depth. *Journal of Physical Oceanography, 9*, 962–974. https://doi.org/10.1175/1520-0485(1979)009%3C0962:TIRCIE%3E2.0.CO;2

Karniadakis, G. E. M., & Sherwin, S. J. (1999). *Spectral/hp Element Methods for Computational Fluid Dynamics*. Oxford University Press.

Kesavan, S. (2004). *Nonlinear Functional Analysis: A First Course* (2nd ed.). Springer, Hindustan Book Agency.

Kromkamp, J., & Peene, J. (1995). Possibility of net phytoplankton primary production in the turbid Schelde Estuary (SW Netherlands). *Marine Ecology Progress Series, 121*, 249–259. https://doi.org/10.3354/meps121249

Kumar, M., Schuttelaars, H. M., Roos, P. C., & Möller, M. (2016). Three-dimensional semi-idealized model for tidal motion in tidal estuaries: An application to the ems estuary. *Ocean Dynamics, 66*, 99–118. https://doi.org/10.1007/s10236-015-0903-1

Lerczak, J. A., & Geyer, W. R. (2004). Modeling the Lateral Circulation in Straight, Stratified Estuaries. *Journal of Physical Oceanography, 34*(6), 1410–1428. https://doi.org/10.1175/1520-0485(2004)034%3C1410:MTLCIS%3E2.0.CO;2

Lesser, G. R., Roelvink, J. A., van Kester, J. A. T. M., & Stelling, G. S. (2004). Development and validation of a three-dimensional morphological model. *Coastal Engineering, 51*(8-9), 883–915. https://doi.org/10.1016/j.coastaleng.2004.07.014

Li, C., & O'Donnell, J. (2005). The Effect of Channel Length on the Residual Circulation in Tidally Dominated Channels. *Journal of Physical Oceanography, 35*(10), 1826–1840. https://doi.org/10.1175/JPO2804.1

Li, C., & Valle-Levinson, A. (1999). A two-dimensional analytic tidal model for a narrow estuary of arbitrary lateral depth variation: The intratidal motion. *Journal of Geophysical Research: Oceans, 104*(C10), 23525–23543. https://doi.org/10.1029/1999JC900172

Murray, A. B. (2003). Contrasting the goals, strategies, and predictions associated with simplified numerical models and detailed simulations. In P. R. Wilcock & R. M. Iverson (Eds.), *Predictions in Geomorphology*. AGU. https://doi.org/10.1029/135GM11

Nitsche, N. O., Ryan, W. B. F., Carbotte, S. M., Bell, R. E., Slagle, A., Bertinado, C., Flood, R., Kenna, T., & McHugh, C. (2007). Regional patterns and local variations of sediment distribution in the Hudson River Estuary. *Estuarine, Coastal and Shelf Science, 71*(1-2), 259–277. https://doi.org/10.1016/j.ecss.2006.07.021

Pedlosky, J. (1987). *Geophysical Fluid Dynamics*. Springer.

Phillips, N. A. (1957). A coordinate system having some special advantages for numerical forecasting. *Journal of the Atmospheric Sciences, 14*(2), 184–185. https://doi.org/10.1175/1520-0469(1957)014%3C0184:ACSHSS%3E2.0.CO;2

Rozendaal, M. P., Dijkstra, Y. M., & Schuttelaars, H. M. (2024). The relationship between linearised 3D and 2DH models for tidally dominated shallow waters. *Ocean Modelling, 188*. https://doi.org/10.1016/j.ocemod.2024.102330

Schenk, O., & Gärtner, K. (2004). Solving Unsymmetric sparse systems of linear equations with PARDISO. *Future Generation Computer Systems, 20*(3), 475–487. https://doi.org/10.1016/j.future.2003.07.011

Schöberl, J. (2014). *C++11 implementation of Finite Elements in NGSolve* (tech. rep.). Vienna University of Technology.

Sochi, T. (2011). Slip at Fluid-Solid Interface. *Polymer Reviews, 51*(4), 309–340. https://doi.org/10.1080/15583724.2011.615961

Sunderland, E. M., Hu, X. C., Dassuncao, C., Tokranov, A. K., Wagner, C. C., & Allen, J. G. (2019). A review of the pathways of human exposure to poly- and perfluoroalkyl substances (pfass) and present understanding of health effects. *Journal of Exposure Science & Environmental Epidemiology, 29*, 131–147.

Valle-Levinson, A. (2010). Definition and classification of estuaries. In A. Valle-Levinson (Ed.), *Contemporary Issues in Estuarine Physics* (pp. 1–11). Cambridge University Press.

Van Damme, S., Meire, P., Ysebaert, T., Van den Bergh, E., Maris, T., & Struyf, E. (2005). The Scheldt estuary: a description of a changing ecosystem. *Hydrobiologa*, *540*, 1–11. https://doi.org/10.1007/s10750-005-0896-8

van Kan, J., Segal, A., & Vermolen, F. (2005). *Numerical Methods in Scientific Computing*. VSSD.

van Neerven, J. M. A. M. (2022). *Functional Analysis*. Cambridge University Press. https://doi.org/10.1017/9781009232487

Villaret, C., Hervouet, J., Kopmann, R., Merkel, U., & Davies, A. G. (2013). Morphodynamic modeling using the Telemac finite-element system. *Geosciences and Computers*, *53*, 105–113. https://doi.org/10.1016/j.cageo.2011.10.004

Westerweel, J., Hofmann, T., Fukushima, C., & Hunt, J. C. R. (2002). The turbulent/non-turbulent interface at the outer boundary of a self-similar turbulent jet. *Experiments in Fluids*, *33*, 873–878. https://doi.org/10.1007/s00348-002-0489-5

Winant, C. D. (2007). Three-Dimensional Tidal Flow in an Elongated, Rotating Basin. *Journal of Physical Oceanography*, *37*(9), 2345–2362. https://doi.org/10.1175/JPO3122.1

A

Geophysical hydrodynamics

To derive the equations governing geophysical hydrodynamics, we start from the famous Navier-Stokes equations that represent conservation of mass and momentum, taking into account the effect of the Earth's rotation (Section A.1). Afterwards, the Boussinesq approximation will be incorporated (Section A.2), and the effects of turbulence will be parametrised in Section A.3. For these sections, we follow Chapters 3 and 4 in Cushman-Roisin and Beckers (2011). Finally, the shallow water equations are derived in Section A.4

A.1. The Navier-Stokes equations

Flowing water obeys the principle of conservation of mass. For any fixed volume of water V, it then follows that

$$\frac{\partial}{\partial t}\iiint_V \rho \, \mathrm{d}V = -\oiint_{\partial V} \rho \mathbf{u} \cdot \mathbf{n} \, \mathrm{d}S. \tag{A.1}$$

Here, ρ is the density of the water, $\mathbf{u} = (u, v, w)$ is the velocity field and $\mathbf{n}$ is the outward unit normal vector. Application of Leibniz's integration rule and the divergence theorem leads to a differential equation, which is commonly referred to as the *continuity equation*:

$$\rho_t + \nabla \cdot (\rho \mathbf{u}) = \rho_t + (\rho u)_x + (\rho v)_y + (\rho w)_z = 0. \tag{A.2}$$

Equation (A.2) is written in Cartesian coordinates, where the x and y coordinates are horizontal and the z-direction is vertical.

While the length scales associated with geophysical fluid dynamics are typically large, they are usually still small enough to warrant viewing the Earth as flat, instead of working with the more accurate spherical coordinates.

By applying the principle of conservation of linear momentum in the same fashion as before, one obtains the *momentum equations*:

$$\rho\left(u_t + uu_x + vu_y + wu_z + f_* w - fv\right) = -p_x + \left(\tau^{xx}\right)_x + \left(\tau^{xy}\right)_y + \left(\tau^{xz}\right)_z, \tag{A.3a}$$

$$\rho\left(v_t + uv_x + vv_y + wv_z + fu\right) = -p_y + \left(\tau^{yx}\right)_x + \left(\tau^{yy}\right)_y + \left(\tau^{yz}\right)_z, \tag{A.3b}$$

$$\rho\left(w_t + uw_x + vw_y + ww_z + f_* u\right) = -p_z + \left(\tau^{zx}\right)_x + \left(\tau^{zy}\right)_y + \left(\tau^{zz}\right)_z - g\rho. \tag{A.3c}$$

In (A.3a-c), p is the pressure and the terms with τ denote normal and shear stresses representing friction. Furthermore, g is the gravitational acceleration, and f and f_* are the Coriolis and reciprocal Coriolis parameters respectively. They are given by $f = 2\Omega \sin\phi$ and $f_* = 2\Omega\cos\phi$, where Ω is the Earth's angular velocity based on a true siderial day, equal to $7.29 \cdot 10^{-5}$ rad s^{-1} (Gerkema, 2019), and ϕ is the latitude in degrees. For estuaries in Northern Europe, with latitudes around 50°, it follows that f is approximately equal to 10^{-4} rad s^{-1}.

The Coriolis terms represent the fact that the water motion is not observed from an inertial reference frame, but rather a rotating reference frame following the rotation of the Earth about its axis. Because of this rotation, the flow would seem to turn counterclockwise for an observer standing on the Northern hemisphere. Thus, while the Coriolis terms can be interpreted as a force deflecting the flow, it is more accurate to view them as correction terms accounting for a non-inertial frame of reference.

Since geophysical flow is predominantly horizontal, the reciprocal Coriolis terms are generally negligible and are therefore often left out of the equations. This is called the *traditional approximation*, (Gerkema, 2019; Gerkema et al., 2008). Furthermore, we will treat the Coriolis parameter f as a constant, by choosing a constant reference latitude. The domain under consideration may thus be seen as a flat plane centered around the reference latitude, and this approximation is fittingly called the *f-plane approximation*.

Equations (A.3a-c) can be further specified by noting that water is a *Newtonian fluid*, that is, a fluid for which the stresses are proportional to the derivatives of the velocity:

$$\tau^{xx} = 2\mu u_x, \qquad \tau^{xy} = \mu\left(u_y + v_x\right), \qquad \tau^{xz} = \mu\left(u_z + w_x\right), \tag{A.4a}$$

$$\tau^{yx} = \mu\left(v_x + u_y\right), \qquad \tau^{yy} = 2\mu v_y, \qquad \tau^{yz} = \mu\left(v_z + w_y\right), \tag{A.4b}$$

$$\tau^{zx} = \mu\left(w_x + u_z\right), \qquad \tau^{zy} = \mu\left(w_y + v_z\right), \qquad \tau^{zz} = 2\mu w_z. \tag{A.4c}$$

Here, μ is the *dynamic viscosity* of the fluid, representing the internal friction. The *kinematic viscosity* is given by $\nu = \mu/\rho$. Using the constitutive relation (A.4) and applying the traditional approximation, the momentum equations (A.3) may be rewritten to

$$u_t + uu_x + vu_y + wu_z - fv = -\frac{1}{\rho}p_x + \nu\Delta u + \nu\frac{\partial}{\partial x}(\nabla\cdot\mathbf{u}), \tag{A.5a}$$

$$v_t + uv_x + vv_y + wv_z + fu = -\frac{1}{\rho}p_y + \nu\Delta v + \nu\frac{\partial}{\partial y}(\nabla\cdot\mathbf{u}), \tag{A.5b}$$

$$w_t + uw_x + vw_y + ww_z = -\frac{1}{\rho}p_z + \nu\Delta w + \nu\frac{\partial}{\partial z}(\nabla\cdot\mathbf{u}) - g. \tag{A.5c}$$

The terms involving $\nabla\cdot\mathbf{u}$ will be eliminated in Subsection A.2 using the Boussinesq approximation.

Combined with the continuity equation (A.2), Equations (A.5a-c) are known as the *Navier-Stokes equations*. Typically, they are augmented by an equation specifying the density. Assuming that water is an incompressible fluid, i.e. a fluid whose density changes by a negligible amount in response to pressure changes, the density depends on temperature T and salinity S through

$$\rho = \rho_0\left(1 - \alpha(T - T_0) + \beta(S - S_0)\right), \tag{A.6}$$

where ρ_0, T_0 and S_0 are constant reference values (Cushman-Roisin & Beckers, 2011, pg. 71). The proportionality constants α and β are called the coefficients of *thermal expansion* and *saline contraction*, and typical values for seawater are $\alpha = 1.7\cdot10^{-4}$ K^{-1} and $\beta = 7.6\cdot10^{-4}$ psu^{-1} (practical salinity units). In this thesis, we prescribe a constant temperature $T = T_0$ and a constant salinity $S = S_0$.

A.2. The Boussinesq approximation

Density variations are typically small in geophysical contexts. In fact, since we prescribe $T = T_0$ and $S = S_0$, our model contains no density variation at all. It follows that the continuity equation (A.2) reduces to

$$\nabla\cdot\mathbf{u} = 0, \tag{A.7}$$

which makes the continuity equation a reflection of conservation of *volume*, as well as conservation of mass. Equation (A.7) holds exactly if the density is constant, but if density variations are small compared to the mean density, (A.7) is a good approximation of the true continuity equation (A.2).

The momentum equations (A.5a-c) are then reduce to

$$u_t + uu_x + vu_y + wu_z - fv = -\frac{1}{\rho}p_x + \nu\Delta u, \tag{A.8a}$$

$$v_t + uv_x + vv_y + wv_z + fu = -\frac{1}{\rho}p_y + \nu\Delta v, \tag{A.8b}$$

$$w_t + uw_x + vw_y + ww_z = -\frac{1}{\rho}p_z + \nu\Delta w - g. \tag{A.8c}$$

Equations (A.7) and (A.8a-c) are commonly referred to as the *Boussinesq approximation* of the Navier-Stokes equations.

A.3. Parametrisation of turbulence

Turbulent flow, in which velocity and pressure change chaotically, is ubiquitous in geophysical hydrodynamics. Indeed, due to the long length scales and low viscosities, the Reynolds number Re given by

$$\mathrm{Re} = \frac{\|\mathbf{u}\|L}{\nu},$$

is typically quite large. In turbulent flow, eddies and vortices of swirling water appear, creating smaller eddies and vortices of their own. Dissipation of energy is concentrated in the smallest eddies, sometimes on the scale of micrometers (Davidson, 2015). Figure A.1 provides an example of a turbulent jet of water, in which eddies appear.

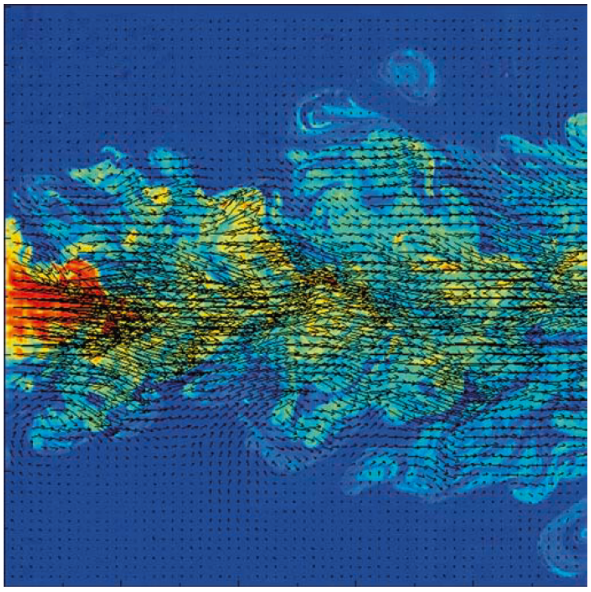

Figure A.1: Water flow in a turbulent jet, captured using laser-induced fluorescence and particle image velocimetry. Source: Westerweel et al. (2002)

Resolving these eddies in geophysical simulations on the scale of hundreds of kilometers is unfeasible. However, turbulence must be captured in the model equations, since it is a dominant energy-dissipating process. In order to achieve this, we *parametrise* the turbulent effects by viewing them as additional viscosity, leading to the so-called *eddy viscosity parametrisation*.

To start, all unknowns are decomposed into a statistically averaged mean part $\langle\cdot\rangle$ free of turbulence, and a fluctuating part representing turbulent motion denoted by a prime. This is called the *Reynolds decomposition*. For instance, the along-channel velocity u is written as

$$u = \langle u\rangle + u', \tag{A.9}$$

with $\langle u'\rangle = 0$.

Using the Reynolds decomposition, equations for the mean flow may be derived by taking the (linear) expected value of (A.7) and (A.8):

$$\nabla \cdot \langle \mathbf{u} \rangle = 0, \tag{A.10a}$$

$$\begin{aligned}\langle u\rangle_t + \langle u\rangle\langle u\rangle_x + \langle v\rangle\langle u\rangle_y + \langle w\rangle\langle u\rangle_z - f\langle v\rangle = &-\frac{1}{\rho}\langle p\rangle_x + \left(\nu\langle u\rangle_x - \left\langle (u')^2\right\rangle\right)_x + \left(\nu\langle u\rangle_y - \left\langle u'v'\right\rangle\right)_y \\ &+ \left(\nu\langle u\rangle_z - \left\langle u'w'\right\rangle\right)_z,\end{aligned} \tag{A.10b}$$

$$\begin{aligned}\langle v\rangle_t + \langle u\rangle\langle v\rangle_x + \langle v\rangle\langle v\rangle_y + \langle w\rangle\langle v\rangle_z + f\langle u\rangle = &-\frac{1}{\rho}\langle p\rangle_u + \left(\nu\langle v\rangle_x - \left\langle u'v'\right\rangle\right)_x + \left(\nu\langle v\rangle_y - \left\langle (v')^2\right\rangle\right)_y \\ &+ \left(\nu\langle v\rangle_z - \left\langle v'w'\right\rangle\right)_z,\end{aligned} \tag{A.10c}$$

$$\begin{aligned}\langle w\rangle_t + \langle u\rangle\langle w\rangle_x + \langle v\rangle\langle w\rangle_y + \langle w\rangle\langle w\rangle_z = &-\frac{1}{\rho}\langle p\rangle_z + \left(\nu\langle w\rangle_x - \left\langle u'w'\right\rangle\right)_x + \left(\nu\langle w\rangle_y - \left\langle v'w'\right\rangle\right)_y \\ &+ \left(\nu\langle w\rangle_z - \left\langle (w')^2\right\rangle\right)_z - g.\end{aligned} \tag{A.10d}$$

Because of the presence of the unknown *Reynolds stresses* $\langle (u')^2\rangle$, $\langle (v')^2\rangle$, $\langle (w')^2\rangle$, $\langle u'v'\rangle$, $\langle u'w'\rangle$ and $\langle v'w'\rangle$, equations (A.10) do not form a closed system of equations. In this thesis, we will assume that turbulent fluids act like Newtonian fluids, and parametrise the Reynolds stresses as additional viscosity similar to (A.4), even though more sophisticated techniques exist (Cushman-Roisin & Beckers, 2011, ch. 14).

Geophysical flows tend to feature horizontal velocities that are much larger than vertical velocities. Therefore, it is to be expected that horizontal turbulent eddies are larger than vertical ones. In light of this, we introduce two parameters: the *horizontal eddy viscosity* A_h and the *vertical eddy viscosity* A_v, where A_h is assumed to be larger than A_v. For simplicity, both are assumed to be constant. The Reynolds stresses can then be written as

$$\left\langle (u')^2\right\rangle = 2A_h\langle u\rangle_x, \qquad \left\langle (v')^2\right\rangle = 2A_h\langle v\rangle_y, \qquad \left\langle (w')^2\right\rangle = 2A_v\langle w\rangle_z, \tag{A.11a}$$

$$\left\langle u'v'\right\rangle = A_h(\langle u\rangle_y + \langle v\rangle_x), \qquad \left\langle u'w'\right\rangle = A_v\langle u\rangle_z + A_h\langle w\rangle_x, \qquad \left\langle v'w'\right\rangle = A_v\langle v\rangle_z + A_h\langle w\rangle_y. \tag{A.11b}$$

Using this parametrisation, a closed set of equations for the mean flow can be derived. In the following, $\mathscr{A}_h$ and $\mathscr{A}_v$ denote the horizontal and vertical *effective eddy viscosity* respectively. They are given by $\mathscr{A}_h = A_h + \nu$ and $\mathscr{A}_v = A_v + \nu$.

$$\nabla \cdot \mathbf{u} = 0, \tag{A.12a}$$

$$u_t + uu_x + vu_y + wu_z - fv = -\frac{1}{\rho}p_x + \mathscr{A}_h u_{xx} + \mathscr{A}_h u_{yy} + \mathscr{A}_v u_{zz}, \tag{A.12b}$$

$$v_t + uv_x + vv_y + wv_z + fu = -\frac{1}{\rho}p_y + \mathscr{A}_h v_{xx} + \mathscr{A}_h v_{yy} + \mathscr{A}_v v_{zz}, \tag{A.12c}$$

$$w_t + uw_x + vw_y + ww_z = -\frac{1}{\rho}p_z + \mathscr{A}_h w_{xx} + \mathscr{A}_h w_{yy} + \mathscr{A}_v w_{zz} - g. \tag{A.12d}$$

In this work, only the mean flow variables are considered and therefore, the brackets $\langle\cdot\rangle$ will be omitted like in (A.12a-d).

A.4. The shallow water equations

The typical length and width scales of estuaries are far larger than their typical depth scales. For instance, the tidal Scheldt estuary in Belgium and Southern Netherlands is approximately 160 km long and its width ranges from 5 km at the mouth to 50 m at the end of the tidal influence zone, whereas the estuary is on average only about 15-20 m deep (see Table 1 in Van Damme et al. (2005)). It follows that the typical length scales for estuarine flow velocities are also much larger in the horizontal than in the vertical. Mathematically, if L is a characteristic horizontal length scale for the water motion and H_0 is a characteristic vertical length scale, we may assume that $H_0 \ll L$.

From the continuity equation (A.12a), it is then possible to derive characteristic scales U and W for the hori-

zontal and vertical flow velocities. The scaling of (A.12a) is given by

$$\begin{array}{ccccccc} u_x & + & v_y & + & w_z & = & 0. \\ \frac{U}{L} & & \frac{U}{L} & & \frac{W}{H_0} & & \end{array}$$

Assuming a three-way balance, it follows that

$$W = \mathcal{O}\left(\frac{UH_0}{L}\right),$$

and since $H_0 \ll L$, the vertical velocity scale W is much smaller than the horizontal velocity scale, i.e. $W \ll U$.

Following Pedlosky (1987), the vertical momentum equation (A.12d) can then be reduced to the *hydrostatic balance*:

$$p_z = \rho g, \qquad (x, y, z, t) \in D, \tag{A.13}$$

with boundary condition $p(\zeta(x, y, t)) = p_a$, where p_a is the atmospheric pressure, assumed to be constant. This ordinary differential equation can be integrated to obtain

$$p(x, y, z, t) = p_a + g \int_z^{\zeta(x,y,t)} \rho(x, y, z', t)\, \mathrm{d}z'. \tag{A.14}$$

Partial derivatives of (A.14) are computed using the Leibniz integration rule. This results in

$$p_x = g\rho(\zeta)\zeta_x + g \int_z^{\zeta} \rho_x \, \mathrm{d}z', \tag{A.15a}$$

$$p_y = g\rho(\zeta)\zeta_y + g \int_z^{\zeta} \rho_y \, \mathrm{d}z'. \tag{A.15b}$$

Here, $\rho(\zeta)$ denotes the density at the water surface ζ, which is equal to ρ at every point $(x, y) \in D_{2\mathrm{D}}$, since the prescribed salinity is constant. The first term in Equations (A.15) is generally known as the *barotropic* contribution to the pressure gradient, and the second term as the *baroclinic* contribution. *Because a constant density is prescribed, the baroclinic pressure gradient vanishes.*

These can then be substituted in the horizontal momentum equations (A.12b-c) to obtain:

$$u_t + uu_x + vu_y + wu_z - fv = -g\zeta_x + \mathscr{A}_h u_{xx} + \mathscr{A}_h u_{yy} + \mathscr{A}_v u_{zz}, \tag{A.16a}$$

$$v_t + uv_x + vv_y + wv_z + fu = -g\zeta_y + \mathscr{A}_h v_{xx} + \mathscr{A}_h v_{yy} + \mathscr{A}_v v_{zz}. \tag{A.16b}$$

Combined with the continuity equation (A.12a), equations (A.16a-b) are known as the (three-dimensional) *shallow water equations*.

Finally, horizontal eddy viscosity is neglected to ensure that non-linear boundary conditions are not required. Indeed, using this assumption, the no-stress boundary condition at the water surface (2.6) is a linear boundary condition.

This simplification may be (partially) justified using a scaling argument. The eddy viscosity parameters may be assumed to scale linearly with the size of the turbulent eddies (Friedrichs & Hamrick, 1996). Thus, $\mathscr{A}_h = \mathcal{O}(\mathscr{A}L)$ and $\mathscr{A}_v = \mathcal{O}(\mathscr{A}H_0)$, for some common factor $\mathscr{A}$ that describes the general viscous effects of turbulence. It then follows that $\mathscr{A}_h u_{xx}, \mathscr{A}_h u_{yy} = \mathcal{O}(\mathscr{A}L^{-1})$ and $\mathscr{A}_v u_{zz} = \mathcal{O}(\mathscr{A}H_0^{-1})$. Since $H_0 \ll L$, $\mathscr{A}_h u_{xx}, \mathscr{A}_h u_{yy} \ll \mathscr{A}_v u_{zz}$. The same holds for the cross-channel velocity v.

B

Solving eigenvalue problem 3.11

Consider the eigenvalue problem (3.11) subject to boundary conditions $f(-1) = 0$, $f'(0) = 0$:

$$f'' = -\lambda f.$$

First suppose that $\lambda < 0$. Then the general solution of (3.11) is given by

$$f(\varsigma) = C_1 e^{\sqrt{\lambda}\varsigma} + C_2 e^{-\sqrt{\lambda}\varsigma}. \tag{B.1}$$

Substituting (B.1) into the Neumann boundary condition results in

$$f'(0) = \sqrt{\lambda}\left(C_1 e^{\sqrt{\lambda}\cdot 0} - C_2 e^{-\sqrt{\lambda}\cdot 0}\right) = \sqrt{\lambda}(C_1 - C_2) = 0,$$

which implies $C_1 = C_2$. In this case, the Dirichlet boundary condition requires

$$f(-1) = C_1\left(e^{\sqrt{\lambda}} + e^{-\sqrt{\lambda}}\right) = 2C_1 \cosh\left(\sqrt{\lambda}\right) = 0.$$

This is only possible if $C_1 = C_2 = 0$. Thus, the only solution associated to $\lambda < 0$ is the trivial solution. Therefore, any λ smaller than 0 cannot be an eigenvalue of (3.11).

Now suppose that $\lambda = 0$. Then the general solution of (3.11) is given by

$$f(\varsigma) = C_1\varsigma + C_2. \tag{B.2}$$

Again, the boundary conditions require that $C_1 = C_2 = 0$, so $\lambda = 0$ is also no eigenvalue.

Finally, suppose that $\lambda > 0$. The general solution of (3.11) is given by

$$f(\varsigma) = C_1 \cos\left(\sqrt{\lambda}\varsigma\right) + C_2 \sin\left(\sqrt{\lambda}\varsigma\right). \tag{B.3}$$

The Neumann boundary condition $f'(0) = 0$ necessitates $C_2 = 0$. Now, substitution of (B.3) into the Dirichlet boundary condition $f(-1) = 0$ leads to the equation

$$C_1 \cos\left(\sqrt{\lambda}\right) = 0. \tag{B.4}$$

Equation (B.4) is solved by $C_1 = 0$, which would again lead to a trivial solution. However, by letting

$$\sqrt{\lambda} = m\pi + \frac{\pi}{2}, \qquad m \in \mathbb{N},$$

Equation (B.4) is satisfied regardless of C_1.

In conclusion, the eigenvalue problem (3.11) is solved by the eigenvalue-eigenfunction pairs (λ_m, f_m) given by

$$f_m(\varsigma) = \cos\left(\left(m + \frac{1}{2}\right)\pi\varsigma\right), \qquad \lambda_m = \left(m + \frac{1}{2}\right)^2 \pi^2.$$